

ABSTRACT

FARRINGTON, NATHANIEL CHRISTIAN. Numerical Weather Prediction of Stratus: Sensitivity to Aerosol Aware Microphysics. (Under the direction of Dr. Gary Lackmann.)

Operational numerical weather prediction microphysics schemes commonly hold cloud droplet number concentration fixed domain-wide to increase computational efficiency. However, observations indicate wide variability of this quantity. Particularly, cloud condensation nucleus concentration has been observed to influence cloud droplet size, leading to changes in cloud radiative and microphysical properties. These changes have been shown to alter cloud depth, lifetime, and other characteristics of importance to operational forecasters. The advent of the Weather Research and Forecasting model version 3.6 includes the Thompson and Eidhammer radiation-coupled microphysics option which is double-moment for cloud water, accounts for some aerosol influences, and is designed for operational efficiency. Tests conducted here show that the new scheme successfully varies aerosol and cloud droplet number concentration temporally and spatially, while significantly altering the radiative properties and coverage of inland coastal stratus in the Pacific Northwest. However, tests also show that several other factors exercise greater sway over stratus coverage and lifetime relative to CCN concentration.

© Copyright 2015 Nathanael C. Farrington

All Rights Reserved

Numerical Weather Prediction of Stratus: Sensitivity to Aerosol Aware Microphysics.

by
Nathanael C. Farrington

A thesis submitted to the Graduate Faculty of
North Carolina State University
in partial fulfillment of the
requirements for the degree of
Master of Science

Marine, Earth and Atmospheric Sciences

Raleigh, North Carolina

2015

APPROVED BY:

Dr. Gary Lackmann
Committee Chair

Dr. Walter Robinson

Dr. Anantha Aiyyer

DEDICATION

I dedicate this work to my wife, Kristen, who continues to set aside her dreams to chase a life with me, and to my Father, brothers, and sisters. You carry me when I am too weak to walk and without you I would not be where I am today.

BIOGRAPHY

Nate Farrington is originally from Scottsdale, Arizona. He grew up amazed at the power, in awe of the lightning, humbled by the bone-rattling thunder, and intrigued by the ominous haboobs of North American Monsoon thunderstorms. Nate has been a forecaster in the Air Force weather community for over 15 years. During his career, he has issued operational aviation forecasts for airspace over every continent and every ocean on the planet except the Arctic, served tours to Iraq and Afghanistan, supported the Special Operations community, and even broadcasted weather forecasts to 1.1 million Defense and State department viewers worldwide for the American Forces Network.

Nate has a wonderful family, including three beautiful children and a lovely and talented wife of almost 16 years. Nate and his family have lived and worked in Germany and six different U.S. states. Nate assembled his undergraduate degree from five different brick and mortar institutions over ten years of rotating shift work and raising a family, culminating in a degree in Natural Science and Mathematics from Thomas Edison State College in 2010. He enrolled in the Atmospheric Science graduate program at North Carolina State University in fall of 2013 where he has been working under the guidance of Dr. Gary Lackmann. Upon finishing his Master's degree, Nate will join the 16th Weather Squadron, part of the Air Force Weather Agency, where he will help the Air Force exploit the latest in science and technology to provide responsive, accurate, and relevant weather information to the warfighter, the intelligence community, and other national agencies.

ACKNOWLEDGMENTS

I would like express gratitude to my advisor, Dr. Gary Lackmann, for the vision and patience to conduct this project with me. His calm and steady hand guided this endeavor through storm and drought; I am indebted to him for his kindness and understanding. I would also like to thank my thesis committee members, Dr. Walter Robinson and Dr. Anantha Aiyyer, for keeping the project soundly grounded in the scientific and meteorological principles to which this thesis' processes are subject. I would also like to thank Dr. Sandra Yuter and Dr. Matt Miller for giving me their honesty, time, and technical expertise.

I thank the United States Air Force and the Air Force Institute of Technology, Civilian Institutions Program for funding this assignment. A very responsive Technical Sergeant Precious Monk at the 14th Weather Squadron (14WS) provided tens of thousands of observations crucial to this analysis. I extend a special thank you to Dr. Neil Jacobs and his team at Panasonic AirDat for gracious access to their proprietary aircraft observations and software. The National Climatic Data Center provided North American Mesoscale Model analyses. The National Center for Atmospheric Research made the Weather Research and Forecasting model available to the public. I am grateful to Unidata for the incredibly user friendly Integrated Data Viewer platform and University of Wisconsin's Cooperative Institute for Meteorological Satellite Studies for their imagery. I particularly want to express my gratitude to Dr. Greg Thompson and Trude Eidhammer for their vision and work to modernize the microphysics of operational Numerical Weather Prediction.

My lab mates, Xiaoyu Long, Chris Marciano, Allison Michaelis, Jennifer Tate, Lindsay Blank, and colleagues, Matthew Morriss, Dianna Francisco, Jeffery Willison, Andy

Meier, Josh Tobias, and Maj Adam DeMarco provided technical assistance and friendship which made this great task easier to bear. My friend, Suchit Mehrotra, aided greatly with statistical analysis software. I would also like to thank Air Force Reserve Officer Training Corps Detachment 595 Commander, Lt Col Jay Allen, for the motivation, competition, mentorship, and friendship with which he led me. I humbly acknowledge Air Force and Army Special Operations aviators who, with weather babbas Mr. John White and Mr. Jerry Gaunt, inspired this project and perpetually inspire me. Special operator Chief Warrant Officer 4 Paul Dulfer provided helpful maps and information. I would like to extend thanks to Mr. Randall Kallenbach and Mr. Stephen Chessler for their mentorship and friendship throughout the years, and for encouraging me to do this.

Finally, I thank my family who have supported and believed in me. I want to thank my dad and mom, Tim and Linda, whose dedication to God, each other, and their professions have helped make me who I am, and whose long arm of love I felt through many valleys. I want to thank my younger brother, Phil, for wisely teaching and admonishing me with psalms and hymns and spiritual songs. I would like to thank my children, Riley, Parker, and Madison, for their resilience and love when my work robbed them of my best time and energy. Above these, I pour out my profound gratitude to my stunning wife, Kristen. I have built my career and life upon the confidence of her selfless support, tireless friendship, and skillful encouragement. Ultimately, I give thanks for all trials and success in the name of my hope, the Lord Jesus Christ, to God the Father and Creator from whose “counsel and dominion” this “most beautiful system” proceeds (Newton 1687).

TABLE OF CONTENTS

LIST OF TABLES	viii
LIST OF FIGURES	ix
1. Introduction.....	1
1.1. Motivation.....	1
1.1.1. Low Cloud Impacts on Military Aviation.....	1
1.1.2. Low Cloud Impacts on Civilian Aviation	4
1.1.3. Impacts of Low Clouds on Radiation.....	4
1.2 Background	6
1.2.1 Stratus Formation and Dissipation Processes	6
1.2.2 Cloud Droplet Formation.....	7
1.2.3 Cloud-Aerosol Interactions and Radiation.....	8
1.2.4 Model Cloud-Aerosol Interactions and Radiation.....	10
1.2.4.1 Model Physics Parameterizations.....	12
1.2.5 Thompson and Eidhammer (2014) Microphysics.....	16
1.2.5.1 Aerosol Input	17
1.2.5.2 Explicit Calculation of Aerosols	17
1.3 Science Questions	19
1.4 Organization.....	20
2. Methods.....	21
2.1 Stratus Event Selection.....	21
2.1.1 Case Study Selection	29

2.2 Configuration of the Weather Research and Forecasting Model.....	31
 2.2.1 Model Domain	32
 2.2.2 Initial Conditions	34
 2.2.3 Physics Choices.....	38
 2.2.4 Model Preparation for Aerosol Climatology Use.....	39
2.3 Cloud Physical and Radiative Properties of Interest.....	43
2.4 Observational Data	45
2.5 Limitations and Statistical Significance.....	49
3. Analysis	51
 3.1 Stratus Case 20130718.....	51
 3.2 Model Cloud Microphysical Properties	62
 3.2.1 Model Cloud and Shortwave Radiation.....	62
 3.3 Model Forecast Verification and Intercomparison	75
 3.3.1 Model Cloud Morphology	75
 3.3.2 Point-Forecast Cloud Coverage	89
 3.3.3 Point-Forecast Cloud Base and Top Height and Geometric Thickness.....	96
 3.3.4 Point-Forecast Timing Forecast Verification.....	111
 3.4 Sensitivity Tests.....	113
4. Conclusions.....	123
 4.1 Science Questions Answered.....	123
 4.2 Implications	125
 4.3 Future Work.....	126

LIST OF TABLES

Table 1 Seattle / Tacoma International Airport frequency of either ceiling below 3,000 ft or visibility less than 1 mile (1600 m) or both. Given by percent of occurrence during 3-hourly local time periods and month of the year (14WS 2015).	29
Table 2 Final case days for which tests were run, with associated 24-hour pressure change observed at 18 UTC and the percentage of available METAR surface stations which observed the event.....	31
Table 3 METAR locations used in this study, organized by initial aerosol concentration (# kg-1) from least to greatest.	44
Table 4 Two by two contingency tables for the binary prediction versus observation of sky cover less than half (CLR to SCT) or greater than or equal to half (BKN to OVC) on 18 July 2013 for the 100 (A), Aero (B), and 1000 (C) runs, gathered for each model run at each site and then aggregated to one daily table for each model run.	93
Table 5 Summary statistics for prediction of occurrence or non-occurrence of cloud cover greater than or equal to half (BKN) on 18 July 2013 computed hourly for each station and then aggregated hourly for all stations. Columns 1 through 5 represent Percent Correct (PC), Hit Rate (HR), False Alarm Rate (FAR), Equitable Threat Score (ETS), and Frequency Bias, respectively for the given criteria.	94
Table 6 Statistical data for the TAMDAR observation values (in feet) taken 18 July 2013 and presented in Figure 39.....	108
Table 7 Forecast for KSEA (a) and KBFI (b) cloud base and top heights (in feet) compared to TAMDAR observations in Table 6.....	108
Table 8 Change in mean absolute error between the 100 control run and the 1000 (a) and Aero (b) forecasts for the onset and dissipation of stratus for 18 July 2013. Values shown are control minus experiment such that positive values are improvement over the control. The “Combined” column indicates the total error difference when using one model (onset MAE + dissipation MAE) versus the control total or a proportion of the control combined MAE ..	113
Table 9 Absolute Error (minutes, 0 = perfect) tabulation for 8 PSB observation locations comparing the performance of the ERA to the NAM as initial conditions for one run of the 1000 configuration. Mean Absolute Error is calculated at the bottom of each column. Note the ERA MYJ combination produced no cloud at CLS, PAE, and NUW.....	117
Table 10 As in Table 8 but comparing the NAM 1000 forecasts using YSU versus those using MYJ PBL schemes	120

LIST OF FIGURES

Figure 1 Global map of GOCART calculated mean aerosol optical depth of sulfates at a wavelength of 550 nm from 18 to 23 July 2006 (Colarco et al. 2010).....	15
Figure 2 Physiographic provinces and meteorologically-significant geographic features of Washington (Adapted from the Washington Department of Natural Resources www.dnr.wa.gov/Publications/ger_geol_map_washington_pagesize.pdf).	25
Figure 3 Topographical map indicating two primary northerly routes (purple and yellow) and one backup route of flight (green) for helicopter crews transiting from KGRF to KYKM for military training missions (Image courtesy of P. Dulfer).	27
Figure 4 Climatology of ceiling height occurrence below 5,000 ft at KSEA by percent of observations of given times UTC (local) and months of the year (14WS 2015).....	28
Figure 5 Map projection of WRF domains used in this study.....	33
Figure 6 Comparison of Skew-T log P diagrams observed by TAMDAR (A), forecast by WRF 100 with NAM218 (B), and with ERA-Interim (C) as initial conditions for 17 July 2013 at 1200 UTC, the 00 hour forecast. Note the differing temperature scales at the bottom of the TAMDAR versus the forecast diagrams.....	37
Figure 7 Vertical profiles of water-friendly aerosol initial condition over Seattle, WA from the ERA aerosol input file interpolated to the ERA (red) and NAM218 (blue) pressure levels for input to WRF. Values shown are aerosol # kg-1 and altitude in meters.	41
Figure 8 Water-friendly aerosol (# kg-1) initial condition in Aero runs. Values are mean aerosol concentrations (number per kilogram of air) as modeled by Colarco et al. (2010) using GOCART. Values shown are column totals from the surface to 850 hPa based on inversion base heights observed in this study, summed to indicate initial BL content.	42
Figure 9 Map of TAMDAR observations for KSEA sampled on 18 July 2013 for flights below 6,000 ft MSL (vertical scale) with cool colors representing heights above 3,000 ft and warm colors representing heights below.....	48
Figure 10 18 July 2013 observed 300 (a), 500 (b), 700 (c), and 850 (d) hPa level and surface (e) charts valid at 1200 UTC and GOES15 visible channel satellite image (f) valid 1515 UTC (Ahijevych 2015, mmm.ucar.edu/imagearchive , WPC 2015, wpc.ncep.noaa.gov/archives/web_pages/sfc/sfc_archive.php).	53
Figure 11 GOES15 visible satellite image valid 2015 (a) Stratus remains along the southeastern PSB and the western Cascade slopes but dissipates by 2245 UTC (b).....	54

Figure 12 Observed surface wind plots from 18 July 2013 from 00 (a) to 23 UTC (i) (Data courtesy Iowa State University, http://mtarchive.geol.iastate.edu/ 2015).	55
Figure 13 Time series of METAR cloud base heights at locations upwind of Seattle-Tacoma during the 18 July 2013 stratus event. Cloud base heights are observed to rise with time after solar heating began.....	56
Figure 14 As in Figure 13, except for locations downwind of the climatological aerosol concentration maximum.....	57
Figure 15 Map of METAR observation stations with insets displaying cloud base height trends from the surface to 4,000 ft (vertical axis) at each location from 03 to 24 UTC 18 July (horizontal axis). General trends show increasing cloud base heights with time before dissipation for all but those locations between the Sound and the Cascades.....	58
Figure 16 TAMDAR soundings at KSEA on 18 July 2013 at 1452, 1604, 1702, and 1808 UTC, as indicated.....	59
Figure 17 Time series scatter plot of surface wind direction (black, left vertical axis in degrees magnetic) and speed (red, right vertical axis in knots) observed at Seattle-Tacoma International Airport (KSEA) on 18 July 2013 (data courtesy 14WS).....	61
Figure 18 As in Figure 8 but at 14 (a) and 18 (b) UTC	62
Figure 19 Overlaid Skew-T log P diagrams for the 100 (blue) and 1000 (red) runs valid for 18 July 2013 at 17 (a) and 18 (b) UTC indicating that the 1000 run is cooler at the surface, and has a lower lifted condensation level than the 100 at each time.	64
Figure 20 Time series of METAR observed surface temperature (black) with 2-meter forecast temperatures from the 100 (blue), 1000 (burnt orange), and Aero (green) runs valid for Seattle on 18 July 2013.	64
Figure 21 Difference fields in downwelling shortwave radiation at the surface (W m ⁻²) at 1400 (a, b) and 1800 UTC (c, d) between the 1000 run (a, c) and the Aero run (b, d) and the control, respectively.	66
Figure 22 Difference fields of total column cloud water (kg kg ⁻¹) between the Aero (a) and 1000 (b) and the control 100 run, respectively, valid 18 July 2013 at 1400 UTC.....	68
Figure 23 Scatter plot (a) indicating the ratio of downwelling shortwave radiation per unit cloud water from 19 to 21 UTC for the 100 control run (blue), Aero (green), and 1000 (burnt orange) runs, respectively. Map (b) indicating the area for which radiation to cloud water	

ratios (a) were gathered, overlaid on column-total water-friendly aerosol concentration (kg kg ⁻¹) at 2015 UTC. Data was calculated at every vertical grid column of the area shown in the map (b) during the two hour period centered on solar noon 18 July 2013.....	70
Figure 24 Goodness of fit of a linear regression fitted to radiation per cloud water data presented in Figure 23. Note the poor conformance of the data to the quantile-quantile plot (top right panel). Data were analyzed using R Studio analysis scripts (Constructed with assistance by Suchit Mehrotra)	71
Figure 25 As in Figure 24, except for a square root transformation of the data. Note the improved fit of the data in the quantile-quantile plot (top right panel) (Constructed with assistance by Suchit Mehrotra)	72
Figure 26 Vertical profiles of Aero run number of water-friendly aerosols (red dashed line) and cloud droplet number concentration (blue solid line) overhead KSEA (a) and approximately 30km northeast of KSEA (b) on 18 July 2013 at 1200 UTC. The vertical axis denotes pressure level heights (hPa), the bottom horizontal axis shows droplet concentrations (# cm ⁻³), and the top horizontal axis shows aerosol concentrations (# cm ⁻³).	74
Figure 27 July 18, 2013, 1345 UTC GOES15 visible satellite imagery with the Unidata IDV visible/fog enhancement applied and overlaid with the 5x10 ⁻⁵ kg kg ⁻¹ 100 (blue) model cloud water mixing ratio as a three-dimensional isosurface. The Aero (green), and 1000 (red) are overlaid onto the 100 image for ease of comparison.	76
Figure 28 As with Figure 27, but valid 1745 UTC and without enhancement to the visible satellite image.	79
Figure 29 As with Figure 28, but valid 2015 UTC.	80
Figure 30 GOES15 visible satellite images valid 2145 (a) and 2245 UTC (b) showing complete stratus dissipation in the PSB.....	81
Figure 31 Comparison of Skew-T log P diagrams observed by TAMDAR (A) at 1409 UTC, and forecast by the 100 (B), Aero (C), and 1000 (D) runs valid for 1400 UTC on 18 July 2013. Note the horizontal and vertical scale of the TAMDAR sounding differs slightly from those of the forecast soundings.	82
Figure 32 Model forecast sounding comparison to TAMDAR as in Figure 31 except valid for 1800 UTC (model runs) and 1808 UTC (TAMDAR).	87
Figure 33 Time series of mean cloud cover proportion averaged across all locations for METAR (black), the 100 (blue), 1000 (burnt orange), and Aero (green) runs.....	90

Figure 34 Cloud coverage proportion mean difference (a and b) and root mean squared error plots (c and d) as evaluated against METAR for the 100 (blue), 1000 (burnt orange), and Aero (green) runs. Comparisons of all sites averaged together at each time are presented in the time series in a and d. Comparisons of each site averaged over all times are presented in b and d.....	91
Figure 35 Observed and model forecast cloud heights (left column) and absolute error (right column) for 18 July 2013 at locations in the Puget Sound Basin. METAR heights are bases only, while model forecasts for 100 (blue), Aero (green), and 1000 (blue) base and top height are provided for perspective.....	98
Figure 36 As in Figure 15, except with model cloud base and top forecast by the 100 (blue), 1000 (burnt orange), and Aero (green) runs added to location plots.....	103
Figure 37 Vertical velocities (cm s ⁻¹) at sigma level .851 for 15 (a) and 18 UTC (b).....	105
Figure 38 Time series of mean cloud base heights for 18 July 2013 over all locations (a) and RMSE calculated for each location's daily mean versus METAR (b) in feet MSL. Values shown are for METAR (black), 100 (blue), 1000 (burnt orange), and Aero (green).	106
Figure 39 Time series of TAMDAR observed relative humidity values of $\geq 99.5\%$, indicating cloud base (gray boxes) and cloud top (blue triangles) observed during 18 July 2013 KSEA (a) and KBFI (b). Statistical analysis of the samples for cloud base and cloud top heights excluded the outliers (black dashes) as values lying outside the mean by more than two standard deviations.....	107
Figure 40 Time series showing mean daily cloud geometric thickness forecasts for all sites averaged at each time for the 100 (blue), 1000 (burnt orange), and Aero (green) forecasts versus TAMDAR (red squares) and METAR (black squares) values.....	109
Figure 41 Time series of model cloud geometric thickness (in feet) valid 18 July 2013 for the 100 (blue), 1000 (burnt orange), and Aero (green) runs.....	111
Figure 42 Box-and-whisker plot of mean absolute error (MAE) in timing (minutes) stratus onset (a) and dissipation (b) forecasts for all locations aggregated for 18 July 2013 for the 100 (blue), 1000 (red), and Aero (green) runs. The percentage of forecasts which were late predicting an event (% Negative) is overlaid (right vertical axis). Percent Negative is a measure of forecast bias in distribution (50% = normally distributed, 0% = early bias, 100% = late bias). MEA observed for each forecast is shown with a solid black dot.....	112
Figure 43 Comparison of 18 July 2013 1800 UTC 850 hPa Omega (Pa s ⁻¹) observed (represented by the NAM218 grid analysis, a) and forecast by the 100 run (b). The 100 over-forecasted subsidence above the inversion (indicated by the excess of pressure increase over	

the PSB in b as compared to a) during the stratus dissipation period, leading to early dissipation in the model.	114
Figure 44 Time series of Seattle forecast cloud water (g kg ⁻¹ , a and c) and downwelling shortwave radiation at the surface (W m ⁻² , b and d) for the 100 run (a and b) versus the 1000 run (c and d) for 18-19 July 2013. Note the different vertical axes values of b and d.	115
Figure 45 As in Figure 42 except for the 100 (royal blue box), 1000 (red box), and the Aero (green box) forecast onset (leftmost of each box) and dissipation (rightmost of each box) times calculated at each location daily for six model runs using the ERA-Interim (Carolina blue plots) and NAM grid 218 (NC State red plots) as initial conditions.....	116
Figure 46 GOES15 Visible satellite image valid on 18 July 2013 at 1715 UTC with three-dimensional overlays for 5 x 10 ⁻⁵ kg kg ⁻¹ cloud water isosurfaces produced by a 1000 run with YSU (cyan) and MYJ (red) PBL schemes.....	119
Figure 47 As in Fig. 26, valid at the same time, except as produced by eliminating the grid scaling factor of TE14 which reduced the surface aerosol flux by 80% for a grid length of 4 km from that of Thompson and Eidhammer's 20 km.....	122

CHAPTER 1

1. Introduction

1.1. Motivation

Microphysics schemes commonly used in many operational numerical weather prediction models, by default, produce clouds with constant cloud droplet number concentration--no matter where they are predicted in space or time. This parameterization can produce clouds unlike those of the physical world, leaving much room for improvement (Thompson and Eidhammer 2014). The question at issue here is whether that improvement would make a difference in the forecast.

1.1.1. Low Cloud Impacts on Military Aviation

The Air Force Special Operations Command (AFSOC) Chief of Operations and Training identifies low cloud ceiling forecast improvement as “priority 1”. Behind poor surface visibility, low cloud ceilings are the greatest impact to aviation employment in a warfighting environment (Hauke 2014). As innocuous as a stratus forecast may seem, the U.S. Air Force’s top leaders identify low cloud base forecasts as the Air Force Weather (AFW) community’s third highest process improvement priority, ahead of over 40 other topics (AFIT 2014). Cloud information at a given location is a significant factor in military planning processes such as Intelligence Preparation of the Operational Environment (IPOE) and the Air Tasking Order (ATO) cycle (AFI 13-1AOC V3 2011). Accurate foreknowledge of cloud timing, height, and coverage can be of great value at each level of military airpower employment from the strategic perspective (climatology) down to the mission planning (24-120 hour forecast) and tactical or execution (1-24 hour forecast) perspectives (Norquist

1999). At the operational level, unfavorable cloud conditions impact commanders' abilities to launch and recover aircraft or allocate assets to missions and targets on schedule or as needed. At the tactical level, low cloud ceilings limit pilots' abilities to complete missions in an effective, safe, and timely manner, affecting how or if they deliver payloads, collect information, and get aircraft and crew safely back to base.

A cloud ceiling is defined as the lowest cloud layer at which greater than half the sky is obscured in aggregate as viewed from the ground (AFMAN 15-111 2009). Visual Flight Rules (VFR) require at least 500 feet of vertical separation (above or below) between manned aircraft and cloud ceilings. This is required in order that "aircrews must be able to control the aircraft by referencing visual cues from a discernible horizon" (AFI 11-202 V3 2014). Air Force and Army aviation guidelines require a minimum vertical clearance of 500 (1,000) feet above ground level (AGL) over level terrain for rotary-wing (fixed-wing) aircraft, and an additional 1,000 feet over mountainous terrain. A properly rated pilot may request Instrument Flight Rules (IFR) which allow in-cloud flight, but regardless must maintain the minimum terrain clearance (AFI 11-202 V3 2014). Mountain obscuration by clouds can severely endanger aircraft and crews during low altitude navigation that a military context sometimes requires (JP 2-01.3). This means that a cloud ceiling lower than 2,000 feet AGL over mountainous terrain may force aircrews to abort the planned route or accept much higher risk to the aircraft and crew in proceeding. Inaccurate forecasts of these clouds endanger missions, aircraft, and airmen.

At any altitude of flight, clouds can impact sensor and weapon system employment. Intelligence, surveillance, and reconnaissance (ISR) aircraft and satellites may employ a

variety of sensors which leverage the visual or infrared wavelengths of the electromagnetic spectrum. Similarly, many attack aircraft and individual munitions utilize similar wavelengths for acquisition of and guidance to target. However, such systems may require cloud-free line of sight (CFLOS). Clouds veiling a point of interest attenuate and scatter laser energy, wash out infra-red energy, and obscure visual line of sight, potentially rendering these multi-million-dollar sensors useless (JP 2-01.3 2009; JP 3-09.1 1999). In fact, “precision-guided” munitions using the Global Positioning System were borne out of a need to solve the line of sight problem with a “weather-proof” strike capability (Hallion, 1997). If a cloud base is too low to obtain CFLOS below cloud without sacrificing safety or concealment, the aircraft may have to climb above the clouds, abort the mission, or assume elevated collateral and personal risk. An aircrew above clouds can achieve or maintain CFLOS if a break in the clouds is large enough to allow sensor employment. That is, CFLOS can be obtained above clouds if the cloud top is low enough, horizontal extent small enough and adjacent cloud bases are high enough to provide suitable slant range visibility and useful sensor footprint (JP 3-09.1 1999). If the cloud top is too high or horizontal extent too great, the aircraft may be forced to an altitude above the sensor’s (or weapon’s) maximum effective range without ever acquiring the target. Cloud base and top heights AGL are so critical to low-altitude aviation employment that Air Force Weather (AFW) regulations mandate cloud base and top height forecasts for these operations to be precise (accurate) to within 100 (200) feet vertically. Horizontal coverage and onset/dissipation time forecasts must likewise be precise to within one-eighth (one okta) of the sky and one hour, and accurate to two oktas of

the sky and two hours, valid up to 24 hours from the time of issuance (AFMAN 15-124 2013).

1.1.2. Low Cloud Impacts on Civilian Aviation

Civilian aviators also operate at the mercy of low cloud ceilings. A 2003 National Traffic Safety Board statistics analysis implicated “ceiling and visibility” as primary contributing factors to 24% of general aviation accidents. Under-rated pilots or ill-equipped aircraft operating in clouds can result in loss of control or controlled flight into terrain. A University of Illinois study found that once in-cloud, VFR pilots rapidly experience a loss of control giving aircrews an average of under three minutes to take life-saving actions and prevent catastrophe (Kulesa 2003). Low ceilings also impact the air traffic industry’s bottom line by decreasing airport takeoff and landing efficiency. Major air hubs often employ parallel approaches utilizing two or more runways with the same heading in order to maximize takeoff and landing efficiency. But because pilots are required to maintain visual horizontal separation from other aircraft, low ceilings prevent side-by-side arrivals. This forces airports like those in Seattle, San Francisco, and Los Angeles to stagger aircraft approaches with increased lag between landings on every runway (Bone, Olmos and Mundra 2000). This can cut efficiency in half, causing airborne and ground delays which lead to extra operating costs through diversions, missed connections, and cancellations. The FAA’s Aviation Weather Research Program found that an accurate marine stratus forecast could prevent arrival and departure delays, potentially saving \$5.45 million annually at just one airport (Kulesa 2003).

1.1.3. Impacts of Low Clouds on Radiation

More accurately representing the height, depth, coverage, and density of low clouds in forecasts addresses a much broader problem: radiative effects (Wielicki et al. 1995; Brenguier et al. 2000; Thompson and Eidhammer 2014). Boundary layer clouds greatly alter the amount of incident solar radiation (insolation) which is reflected or absorbed and re-radiated into the atmosphere (Stephens and Greenwald 1991; Brenguier et al. 2000) which contribute to turbulent kinetic energy (TKE), vertical velocity and other cloud formation, maintenance, and dissipation factors in the boundary layer (BL) (Rogers and Yau 1989). Cloud base height, vertical development, and horizontal extent of BL clouds are, by definition, highly sensitive to surface and BL temperature variations. By altering the amount of insolation which reaches the ground, BL clouds provide their own feedback which, if not skillfully treated in operational forecast models, can lead to large forecast errors in cloud base height, coverage, timing, and thickness as well as precipitation type, intensity, and frequency (Neiburger 1944; Wood 2012).

Beyond the aviation applications and cloud radiative property representation of improved operational (short-term) forecasts, getting cloud radiative properties right is paramount to predicting the Earth climate system over the long run. The term albedo refers to an object's ability to reflect shortwave light. The high albedo and low altitude of BL clouds make them a significant cooling force in the balance of Earth's radiation budget (ERB) such that just a 4% increase in marine stratiform clouds could offset global temperature rise caused by a doubling of atmospheric CO₂ (Randall et al. 1984). However, climate calculations based on historical reanalysis data and future scenarios fail to accurately

represent cloud radiative properties and feedbacks, leading to large errors in observed and predicted radiation budget estimates (Abel et al. 2010). Inadequate representation of clouds in climate models is a primary source of uncertainty in global climate change predictions (Bony and Dufresne 2005). Although suggestions for alterations to climate models are far beyond the scope of this work, ideas incorporated here may indeed improve cloud prediction accuracy in future climate models.

1.2 Background

1.2.1 Stratus Formation and Dissipation Processes

The archetypal synoptic pattern conducive to stratus formation is general ridging of high pressure and higher heights aloft and a dominant surface anticyclone with low level cold air advection over a moisture source. The midtropospheric ridge axis generally forms the western boundary of the underlying stratus field, which occurs under an area of large-scale subsidence. Stratiform clouds generally form as the boundary layer cools and moistens due to one or a combination of radiative processes or by buoyant or turbulent mixing. Surface longwave radiation can cool the boundary layer by several degrees C overnight, also encouraging saturation (Wood 2012). In the case of the Puget Sound Basin (PSB) in the summer, the Pacific High provides the subsidence, stability, and moisture required of stratus formation. Under a marine push, this feature also provides the horizontal wind required for turbulent mixing in the boundary layer, and the PSB receives onshore flow of air laden with Pacific moisture. Moist air undercutting dry continental air or that of a subsiding overlying airmass creates a strong temperature inversion, which is resistant to mixing. With the development of a turbulent boundary layer, or sufficient shear across the inversion, mixing

and entrainment can result, causing marine stratus to evaporate. In the presence of sufficient moisture and mixing, this brings the temperature and dew point to saturation, which causes stratus formation (Wood 2012). The dry air often present above the inversion in the PSB limits cross-inversion mixing, and can lead to persistent episodes of stratus trapped beneath the inversion layer.

Dissipation of stratus often occurs by LCL lifting. When solar heating or other surface warming and drying increases the height of the lifted condensation level (LCL), stratus is eroded from below by warming the subcloud layer and increasing the dew point depression such that saturation cannot be maintained. Stratus thinning also occurs when the PBL is suppressed under strong subsidence, forcing the cloud base down to the LCL (Wood 2012). Cloud scavenging by drizzle dries a stratus layer by water removal (Albrecht 1989). Excessive cloud top cooling by evaporation could overcome cloud maintenance processes and cause excessive dry air entrainment which thins and erodes stratus (Randall 1984). A combination of these processes is also effective (Wood 2012). Clouds formed in marine airmasses contain a small number of large cloud droplets (Rogers and Yau 1989), making them less optically thick to incident solar radiation (insolation) than continental or polluted clouds with a higher number of smaller cloud droplets, which increase the cross-sectional area available to reflect or refract sunlight (Twomey 1974). The stratus dissipation process over land is markedly different from that over water. Over land, solar warming of the PBL leads to bottom-up solar dissipation much more frequently than over water, where a limited diurnal temperature range is observed.

1.2.2 Cloud Droplet Formation

In order for a cloud to form, moist air must be cooled from the ambient temperature to the dew point temperature (saturation), when rates of evaporation and condensation are equal. Adiabatic ascent of a moist parcel can cool the parcel to saturation. But in nature condensation of liquid water from water vapor (homogeneous nucleation) does not occur automatically just because saturation is reached. In fact, in order for droplets to automatically form this way, the relative humidity would have to exceed several hundred percent. Instead, when a parcel of air containing water vapor is sufficiently cooled, water vapor condenses into liquid water on cloud condensation nuclei (CCN) in heterogeneous nucleation (Rogers and Yau 1989).

Cloud condensation nuclei are micron and sub-micron sized natural and manmade particles found in abundance in the atmosphere. Of all aerosols found in the atmosphere, CCN constitute a narrow part of the greater spectrum based on two primary characteristics, particle radius (r) and hygroscopicity. In other words, particles must be sufficiently large ($> 0.1 \mu\text{m}$) and hydrophilic to constitute CCN (Rogers and Yau 1989).

Concentrations of CCN aerosols vary greatly with time and space. A pristine, remote marine airmass with no wind may have a concentration of nucleation-sized aerosols on the order of 1×10^1 to $1 \times 10^2 \text{ cm}^{-3}$ whereas “clean” continental air contains $1 \times 10^3 \text{ cm}^{-3}$ and polluted urban air holds as many as $1 \times 10^5 \text{ cm}^{-3}$ Aitken mode CCN (Lance et al. 2004).

However, cloud droplet concentration is not simply a function of the availability of CCN. The proportion of particles which nucleate is determined by updraft velocity and the chemical properties of the nucleus. The greater the updraft velocity and more hydrophilic a

particle, the greater the proportion of particles which are activated. The size of the particles largely determines the required critical supersaturation (S) for droplet formation. The larger the particle, the lower the required S , but small particles can nucleate below S . Therefore, the number and size of particles available for nucleation by an updraft determines how many cloud droplets a given cloud volume contains (Rogers and Yau 1989).

1.2.3 Cloud-Aerosol Interactions and Radiation

Cloud droplet number concentration (N_d) of a cloud has implications on its physical and radiative properties. Conover (1966) postulated that for fixed liquid water content (LWC) and cloud depth (H), visible cloud albedo would increase from 13 to 38% if N_d increased from 30 to 200 cm^{-3} . Twomey (1974) confirmed that the unnaturally small size and high concentration of anthropogenic aerosols act to increase the number of CCN and significantly increase N_d . For fixed LWC per unit volume, Twomey noted that the increase in N_d yielded a significant increase in droplet surface area per unit surface area of Earth, with far more numerous and smaller CCN came far more numerous and smaller cloud droplets, resulting in a ~25% increase in cross-sectional surface area with a doubling of droplet number. More and smaller droplets can increase cloud top cooling which acts to sustain or even grow cloud depth through cloud deepening through entrainment (CDE, Randall 1984). Albrecht (1989) showed that greater CCN concentrations delay precipitation due to smaller droplet effective radii resulting in lower collision efficiency, delaying removal of cloud water by precipitation, which prolongs cloud lifetimes and increases fractional cloudiness. Ackerman et al. (1993) extended Albrecht's findings, noting that in non-precipitating marine stratiform clouds, increased CCN and N_d correspond to delayed dissipation of a cloud layer,

and maintenance of its geometric thickness and optical depth (opacity) even at near constant (1993, 2003) or smaller (1995b, 2000) cloud water values. This occurred due to the lower collision efficiency of smaller droplets limiting the CCN removal rate, which acts as a positive feedback for CCN and droplet concentration maintenance, and thereby cloud lifetime extension. This process is balanced by the aerosol direct effect and longwave absorption by cloud droplets (Ackerman 2000) which would warm a cloud layer and help stabilize a boundary layer, and is more directly controlled by large scale subsidence, sea surface temperature, and other synoptic factors (Ackerman et al. 1995b).

Greater cloud opacity, or the droplet density of the cloud relative to insolation, logically determines the rate of surface heating by the sun (especially over land), and resultantly the cloud dissipation rate, with operational implications. But with all the theory pointing toward the influence of CCN concentration and N_d on clouds, the state of operational forecasting for these phenomena lags.

1.2.4 Model Cloud-Aerosol Interactions and Radiation

As numerical weather prediction (NWP) blossomed from the 1980s to the present century, efforts of increasing complexity have sought to address aerosol-cloud microphysical interactions in a computationally efficient enough manner as to facilitate use in operational NWP models. Operational NWP models are run on time scales of ~6 hours and their output is valid for ~24 to 72 h. The “operational” constraints on computational efficiency and micron-sized processes of real cloud microphysics limit the degree to which NWP parameterization can represent the physical processes.

All tropospheric weather is caused by differential heating of Earth by incoming solar radiation, the primary driver of the Earth climate system. For the last several decades, concerns over anthropogenic aerosol contributions to the greenhouse effect have motivated efforts to tease out individual contributions from direct aerosol effects, increased water vapor effects, and cloud reflectance to the Earth's radiation budget (ERB). The Earth intercepts approximately 341 W m^{-2} of shortwave solar radiation at the top of the atmosphere (TOA) on average over time (Trenberth et al. 2009). Satellite measurements of TOA outgoing shortwave radiation show that approximately 30% ($\sim 102 \text{ W m}^{-2}$) of that is reflected back into space. Including outgoing longwave radiation of $\sim 239 \text{ W m}^{-2}$, Earth remains in relative radiative stasis (Ramanathan et al. 1989; Yang et al. 2011) with a possible 0.9 W m^{-2} mean net surface absorption (for the period of March 2000 through May 2004) as estimated by Trenberth et al. (2009). Of the $\sim 341 \text{ W m}^{-2}$ average daily incident solar radiation (insolation) at the top of the atmosphere (TOA), Stephens and Greenwald (1991) found that stratiform BL clouds may reflect upwards of 70 W m^{-2} back into space with clear skies aloft. This becomes significant when viewed in the light that the greenhouse effect of CO₂ retains only 32 W m^{-2} (Kiehl and Trenberth 1997). The contrasting radiative impacts of high versus low clouds also indicate importance for the stratus and stratocumulus problem. Because low, warm clouds emit more infrared energy according to the Stefan-Boltzmann law, but reflect with a high albedo, they exert a cooling influence on the Earth. High clouds exert a warming influence. While the focus of this thesis is on operational, short-term prediction, there are relevant aspects to the climate problem, and it is important that the general circulation models used in climate projection parameterize cloud processes accurately.

Modern weather forecasting is heavily dependent on numerical weather prediction (NWP) models. Advances in remote sensing, computing technology, data assimilation, and equations that describe the physics and dynamics of the atmosphere have led to a ~55% (~35%) improvement in 36-hour (72-hour) forecast skill over the last five decades (Harper 2007). Operational model resolution alone has improved by an order of magnitude in just 15 years (Norquist 1999; Thompson and Eidhammer 2014). Significant challenges with BL depth, liquid water path (LWP) (Wyant et al. 2010) and parameterization of various physical processes (Abel et al. 2010) limit the realistic representation of low cloud height, depth, density and coverage by operational models. A key missing piece to the cloud forecast puzzle is accurate representation of aerosol-cloud interactions (Thompson and Eidhammer 2014).

1.2.4.1 Model Physics Parameterizations

Parameterization schemes are used in NWP models to represent various natural processes they cannot directly calculate. Parameterization schemes avoid the computational expense of explicitly calculating certain variables by estimating results of certain sub-grid scale processes which either cannot be resolved by the model grid spacing, or are too computationally expensive to be computed on practical time scales. Parameterization estimates the values for variables resulting from unresolved processes by taking resolved variables as inputs and calculating output internally or choosing output estimated in a lookup table or other fixed data source, then passing this value back to grid scale variables such as potential temperature (θ), water vapor mixing ratio (Q_v), and wind (U). This parameterization process saves time and hardware use, but introduces potential errors in a model's solution. Present computational technology and knowledge of real physical processes necessitate

parameterization of surface layer, land surface, planetary boundary layer, radiation, cumulus, and cloud microphysical processes.

Cloud microphysical processes are parameterized in models using microphysics parameterization (MP) schemes. Many additional parameterizations and assumptions are included within such calculations. These include values for aerosol mean radius, aerosol hygroscopicity, cloud droplet size distribution, and N_d , four factors critical to proper accounting of aerosol-cloud interaction, precipitation, and radiation.

Aerosol mean radius or aerosol median radius is a value often prescribed in MP scheme subroutines to represent the average chemical constituent and mass which comprise CCN. The typical radius among a population of potential CCN is crucial to the fraction of CCN that activate and the speed with which they reach critical radius to grow into cloud droplets, and eventually the efficiency with which collision and coalescence produce precipitation-sized drops. The work of Saleeby and Cotton (2004) used a binned lognormal distribution of ammonium sulfate with a mass spectrum from 10^{-17} to 10^{-8} g and radii from 0.04 to 0.96 μm with a geometric standard deviation of 1.8 in a Lagrangian parcel model which used Kohler theory to nucleate cloud droplets. In sensitivity tests for cloud nucleation under various vertical velocities, temperatures, and CCN concentrations, Saleeby and Cotton used a binned lognormal distribution about a median CCN radius of 0.04 μm .

As noted, chemical constituents which might act as CCN vary widely in composition and concentration with location. As discussed previously, these various chemical constituents have differing hygroscopicities. Pringle et al. (2010) observed global surface mean hygroscopicity (for mixed Aitken and accumulation modes) of 0.72 ± 0.24 and 0.27 ± 0.21

for maritime and continental regions, respectively. Prescribing this value as a hygroscopicity parameter, κ , is a low-computational-cost method to account for the influence of an aerosol population's chemical composition on CCN activation for NWP purposes. Petters and Kreidenweis (2007) formulated a simple mixing method commonly used in recent studies (Pringle et al. 2010). This value is used in Kohler model calculations to determine the number of particles of a given aerosol population that will activate at a given S . This gives rise to an N_d for a given model volume.

Perhaps the most important control variable in MP schemes is the parameterization for CCN number (Feingold and Heymsfield, 1992) as it controls activation spectrum for a given updraft velocity, resulting in the N_d . As discussed in section 1.2, Models used for operational forecasting have traditionally been forced by way of computational savings to prescribe N_d instead of explicitly calculating it. This is due to the infinitesimally small scale, yet pervasive spatial extent and constant frequency of cloud microphysical processes like CCN activation, water vapor condensation, latent heat release, droplet growth, evaporation, and precipitation scavenging. Setting the number of cloud droplets per volume is simple and saves computational expense. However, the default prescription of N_d in MP schemes is even less physically representative than the parameterization in general. As discussed previously, observed cloud condensation nuclei concentration can vary by orders of magnitude across both time and space (Lance et al. 2004), with the highest concentrations near urban areas and at ground level (Fig. 1).

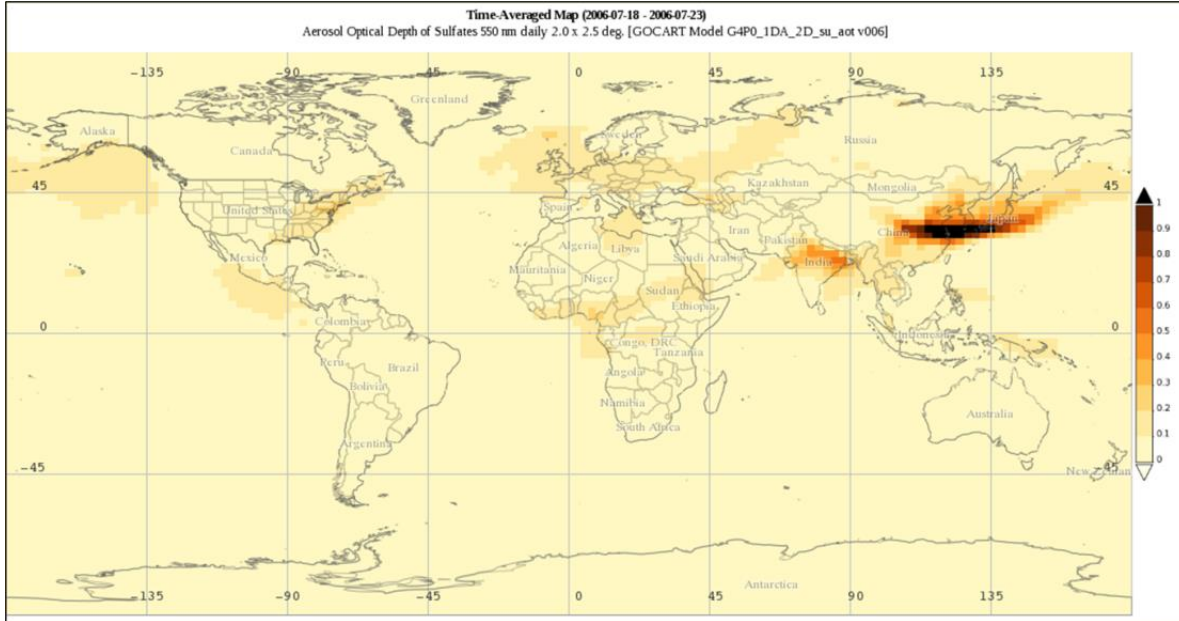


Figure 1 Global map of GOCART calculated mean aerosol optical depth of sulfates at a wavelength of 550 nm from 18 to 23 July 2006 (Colarco et al. 2010).

This would result in a similarly varying distribution of CCN, and potential N_d . Yet many of the single-moment WRF MP schemes previously available for operational forecasting (due to reduced computational expense) prescribe the same N_d for every grid cell, no matter what the location or height above ground. This means that the same N_d values are used in upper tropospheric cells over the pristine remote ocean as are used in the lowest model level over downtown Los Angeles, CA.

The default N_d prescription for the Thompson (2008, hereafter T08) scheme in WRF is 100 cm^{-3} . As discussed in section 1.2, this number is a 50% overestimate for remote ocean air and a minimum 66% underestimate for continental air. In fact, one study of this parameter in the skies over Los Angeles, CA found that N_d of $2,000 \text{ cm}^{-3}$ were not uncommon (Cubison et al. 2008). The T08 and Thompson and Eidhammer (2014) microphysics schemes also use

100 cm^{-3} as the default N_d prescription. However, within the opening comments of the module code, Dr. Greg Thompson adds a note about the importance of prudent use of the N_d setting for regional representation. Importantly, the latter scheme constitutes a novel method for calculating N_d explicitly.

1.2.5 Thompson and Eidhammer (2014) Microphysics

Many models such as WRF-Chem have incorporated full physics and explicitly calculated aerosol number concentration as well as accounted for the different chemical constituents of a given air parcel and several other factors of which operational WRF-ARW is incapable. However, WRF-Chem is computationally too expensive to run with full chemistry and physics on operational time scales, taking USAF resources as many as six times longer to run than WRF-ARW (Neemann 2015). If run with near-real-time data from an initialization time like an operational model, the WRF-Chem run time would exceed the forecast valid time. The output data would be too old to be usable, and in fact the valid time would likely have passed by several days. However, the Thompson and Eidhammer microphysics scheme (microphysics option 28), hereafter TE14, explicitly calculates aerosol number concentration and N_d and claims only a 16% increase in computational expense (2014). Therefore, TE14 presents a potential advance in the effort to bring operational forecast representations of the atmosphere closer to those of the physical world.

The TE14 MP scheme updates the T08, bulk microphysics scheme which is a class 7 scheme, using single-moment prediction of mass mixing ratio for cloud water, snow, and graupel plus double-moment prediction of cloud ice and rain. The TE14 scheme adds prediction of IN and CCN activation, becoming a double-moment scheme for cloud water,

hygroscopic “water-friendly” aerosols (N_{wfa}) which the scheme treats as CCN, and non-hygroscopic “ice-friendly” aerosols (N_{ifa}), treated as IN (TE14).

1.2.5.1 Aerosol Input

In an effort to represent a more realistic horizontal distribution of potential CCN and IN, but reduce the computational expense of assimilating real-time aerosol and chemistry inputs like the WRF-Chem does, the T14 MP scheme utilizes an aerosol climatology based on aerosol number concentration (TE 2014). The Goddard Chemistry Aerosol Radiation and Transport (GOCART) model (Ginoux et al. 2001) run globally for the span of 2001-2007 by Colarco et al. (2010) provided that aerosol climatology. Colarco et al.’s GOCART run explicitly modeled natural and anthropogenic particles and their precursors, binned by species size. Thompson and Eidhammer placed the mass mixing ratios of sulfates, sea salts, organic carbon (CCN), and dust (IN) for each horizontal grid cell into simplified bins. The IN, non-hygroscopic mineral dust mode included GOCART dust mass greater than $0.5 \mu\text{m}$. All other species except black carbon were binned into a homogeneous hygroscopic CCN mode. Thompson and Eidhammer converted these mass mixing ratios into final number concentrations using log-normal distributions, yielding the monthly variables called QNWFA and QNIFA in WRF (TE14).

1.2.5.2 Explicit Calculation of Aerosols

Accounting for aerosols in TE14 includes terms for aerosol emission, CCN activation, homogeneous ice nucleation and depositional freezing of deliquesced aerosols, precipitation scavenging, and evaporation (TE 2014).

To represent surface aerosol emissions of N_{wfa} and N_{ifa} , TE14 uses the near-surface concentration values and the mean surface wind to calculate a constant flux from the lowest model level throughout the model evolution following $\frac{dN_{wfa}}{dt} = 10^{[LOG(N_{wfa}) - 3.69897]}$. For an initial value of $N_{wfa} = 500 \text{ cm}^{-3}$ the flux is designed to be $0.1 \times 10^6 \text{ kg}^{-1} \text{ s}^{-1}$. Given the proper PBL scheme choice and other settings, this scalar value will mix through the boundary layer just as other scalars do, and into the free atmosphere in dry adiabatic or prolonged large scale lifting conditions.

To represent cloud droplet nucleation, the TE14 MP scheme uses predicted values for temperature, vertical velocity, un-activated aerosol number, and prescribed values for hygroscopicity parameter and aerosol mean radius to determine a fraction of aerosols to activate as CCN by means of a look-up table. This method enables TE14 to attempt representation of aerosol concentration variability and cloud droplet number concentration inhomogeneity in a more realistic manner than uniform N_d assignment throughout the domain. It also saves the computational expense of explicit treatment of chemical constituents' hygroscopicity and radii, as in WRF-Chem, and helps preserve TE14's potential utility in operational forecasting. As discussed, grouping all possible constituents' hygroscopicity values into one value for κ is a generalization and obviously unphysical. The inescapable caveats of using such a method include the noted unphysical nature of this parameterization, and the need to reasonably represent constituent-mean appropriate values for aerosol mean radius and κ for a particular geographic region and time of year pertinent to the simulation or forecast at hand. In their study of a midlatitude winter cyclone over the U.S.

plains states, an aerosol mean radius of $0.04 \mu\text{m}$, based on the CCN median radius used in the cloud nucleation work of Saleeby and Cotton (2004), and κ value of 0.4 was used. This is the default setting in the TE14 module in WRF 3.6. Findings of Feingold and Heymsfield (1992) indicate that there is far greater error in droplet effective radius calculation for errors in N_d ($\sim 70\%$ for tenfold error) than for errors in κ ($\sim 8\%$ for tenfold error) which means it is a much higher priority to get the aerosol number right than it is to accurately represent a mixed aerosol population's hydrophilic magnitude. Results from Petters and Kreidenweis (2007) further suggest that hygroscopicity parameterization such as that used by TE14 is adequate to predict CCN activation from a mixed particle population.

In addition to calculating aerosol concentration explicitly, the TE14 scheme adds another process. It passes variables from the MP scheme to the radiation scheme for use in translating cloud properties, incident shortwave radiation, and other variables into the radiation scheme's calculations. This feature of TE14 is designed to work specifically with the RRTMG LW and SW schemes (Iacono 2008).

1.3 Science Questions

Given the extant knowledge of CCN concentration and N_d since the middle of last century and the advance of computational ability in recent decades, operational use of aerosol-cloud interaction is surely short in coming. However, given the considerable computational expense and difficulty of initialization of models such as WRF-Chem, one wonders whether the basic CCN properties in TE14 could account for changes in forecast cloud properties such that the improvement over existing N_d prescriptions would be worth any additional computational expense. The primary hypothesis under study here is that

increasing model cloud droplet number concentration could result in more representative forecasts for cloud properties such as radiation transmissivity and cloud lifetime.

If N_d increases correspond with decreases in cloud transmissivity or increases in cloud lifetime, the immediate temptation is to suspect a corresponding increase in LWC or LWP as the cause. Ackerman (1993) showed that LWP remained relatively constant during simulations of doubling CCN count. However, for N_d greater than double the default value of 100 cm^{-3} , there is a potential to observe a change in cloud transmissivity due to LWP alone. Another hypothesis under consideration is that clouds with increased N_d will exhibit reduced radiation transmissivity, regardless of the liquid water content of a volume.

1.4 Organization

The following chapters will discuss key components of the body of work previously accomplished in the study and numerical prediction of low cloud, describe this work's methods in advancing that knowledge, identify some key results, and propose future efforts in the advancement of low cloud forecasts incorporating aerosol awareness.

CHAPTER 2

2. Methods

This chapter outlines the data and methods used in this study. A description of case selection criteria is given. Next, the WRF settings used for control and experimental forecasts are discussed. A brief description of analysis techniques for various cloud physical and radiative property changes is presented. A discussion of the cloud forecast verification metrics follows, including a presentation of the three observational data sets against which forecasts are verified. The chapter concludes with a brief discussion about the limitations and statistical significance of this study.

2.1 Stratus Event Selection

In order to test for any effect of varying aerosol and cloud droplet number concentration on numerical predictions of stratus, a multiple case study approach is preferable such that model cloud properties could be measured against real-world observations in a variety of cases. Toward this effort, the following aspects were sought: (i) warm-cloud situations, to allow focus on cloud-radiation interactions in the absence of ice processes, (ii) a cloud type that presents an important operational forecasting challenge, and (iii) a location that offers sufficient observational data against which to evaluate model performance. Some additional meteorological considerations in case study selection include cloud type, topography, synoptic regime and seasonality, and proximity to both a significant moisture source and a climatologically consistent source of anthropogenic aerosol. Measurement considerations constraining this study include availability of ground and

airborne meteorological observations, frequency of cloud occurrence, as well as horizontal and vertical extent of the cloud (observability).

Although the Thompson and Eidhammer (2014) microphysics scheme has incorporated “ice-friendly aerosols” in its calculations, ice processes add complexity which exceeds the scope of this study. Therefore, liquid-phase clouds are preferred. This points toward low-tier clouds and almost exclusively during summer months when the freezing level is high relative to the cloud top, and the majority of mixed-phase cloud particles are even higher.

As discussed in Chapter 1, vertical velocity is the single greatest non-nucleus contributing factor to cloud droplet nucleation and growth besides saturation vapor pressure and temperature. Considering that cloud base vertical velocities of Cumulus Humilis, Cumulus Congestus, and Cumulonimbus are on average 3 m s^{-1} , 10 m s^{-1} , and 30 m s^{-1} respectively, stratiform clouds are formed and maintained by the smallest vertical velocities of any boundary layer cloud type. Fog—essentially a ground-based stratus cloud—exhibits the lowest vertical velocities of any low cloud, 0.01 m s^{-1} on average. However, fog’s shallow vertical depth of approximately 100 m, limited horizontal extent on the order of 100 to $1,000 \text{ km}^2$, and lifetime of only 2 to 6 h make it less than ideal for capturing the cloud-aerosol interactions of this study. Typical cloud depth, horizontal extent, and lifetime of stratus and stratocumulus clouds are on the order of 200 to 300 m, $1,000$ to $10,000 \text{ km}^2$, and 6 to 12 h, respectively. These properties make stratus more observable and fog less suitable for observation by comparison. Stratus and stratocumulus clouds can be formed and maintained with an average of 0.01 to 0.1 m s^{-1} vertical velocity at the cloud base (Cotton,

Bryan and Van den Heever 2010). Differentiating between the vertical velocities of stratus and stratocumulus requires more care. The maintenance mechanism of stratocumulus is a turbulent flux of moisture and heat through the depth of the layer in inhomogeneous “cells” where vertical velocities are routinely 0.25 to 1.25 m s⁻¹, therefore variations between peaks and troughs can differ by a factor of 2 to 5 over the horizontal scale of a few kilometers (Wood 2012). By selecting stratus as the cloud of study, we maximize observability and minimize the vertical velocity variability which would cause a predominant proportion of the variability spatially, temporally, and case-to-case in stratocumulus.

With stratus as the cloud type of study, consideration turns to a location and time of year in which stratus frequently occur. As noted in Chapter 1, previous study has been made mostly of vast stratocumulus fields over the open ocean of the southeast Pacific near Peru, the eastern Atlantic near the Azores, and eastern Pacific near Los Angeles, CA. Neither Peru nor the Azores/Iberian Peninsula regions climatologically host a high enough anthropogenic aerosol concentration to test the phenomenon of interest. Typical aerosol counts in those regions were 100 to 300 cm⁻³ during VOCALS Rex and ACE-2 (Yang et al. 2011, Brenguier et al. 2000), barely exceeding those of the default WRF setting for N_d, which is 100 cm⁻³. However, Seattle, WA and the Puget Sound Basin experience warm season marine stratus and are frequently hazy under stagnant conditions.

The term “Puget Sound Basin” broadly describes the watershed land surface and water area between the Olympic Peninsula and the Cascade Mountains, from the Portland Basin to the Strait of Juan de Fuca in the north (Fig. 2). The Puget Sound Lowland is the general depression centered on the sound which tapers to a terminus near the OR border,

approximately 125 km south of the southern coast. The Willapa Hills encompass the area between the Pacific and the southern Lowland and are separated from the Olympic Mountains by the Chehalis Gap. Together, the Olympic Mountains and the Willapa Hills are referred to as the Coastal Range (Lasmanis 1991). The PSB often receives westerly low-level “marine pushes” of moist air flowing off Pacific Ocean, around the Olympic Mountains through both the Strait of Juan de Fuca and the Chehalis Gap, forming the Puget Sound Convergence Zone (Mass 1981). The Puget Sound has an average July water surface temperature of 12 to 13 C (NODC 2015), is approximately 300 m deep, is fed by numerous river inlets, and is accompanied by numerous lakes ponds, particularly in the lower-lying gentle slopes near the Chehalis Gap (14WS 2015). Sunrise (sunset) times in Seattle during the summer range from 0513 L / 1213 UTC (2036 L / 0336 UTC) to 0553 L / 1253 UTC (2111 L / 0411 UTC). Solar azimuth at sunrise (sunset) was within 5 degrees of heading 058 (301) and solar noon occurred within 4 minutes of 1312 L / 2112 UTC (<http://www.timeanddate.com> accessed 2015).

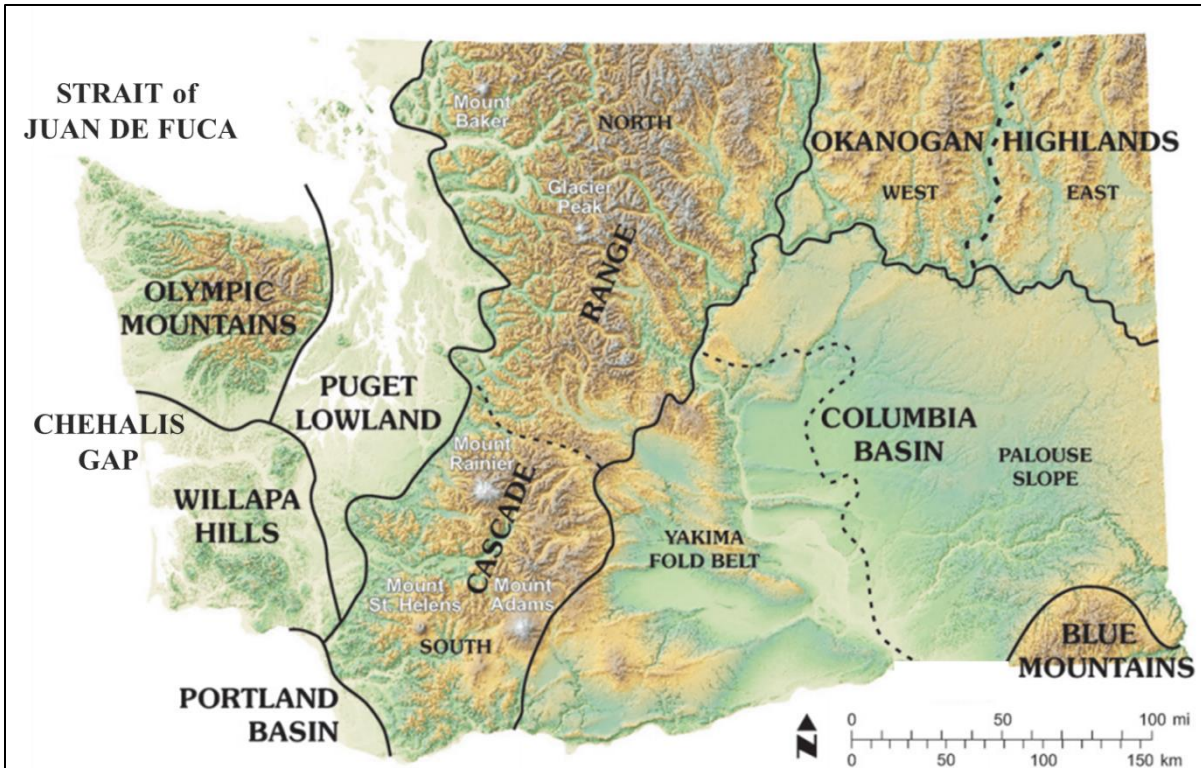


Figure 2 Physiographic provinces and meteorologically-significant geographic features of Washington (Adapted from the Washington Department of Natural Resources www.dnr.wa.gov/Publications/ger_geol_map_washington_pagesize.pdf).

The PSB land surface is approximately 30,000 km² (USGS 2015), contains 12 international, regional, and military airfields with reliable meteorological equipment which are not divided by mountains. Not particularly famous for pollution, the southern PSB is a major urban area. At a potential 36 per million people, cancer cases due to toxic air pollutants are over 27 times more likely to develop in residents of Seattle and Tacoma than the national average (Doughton 2009). Every county along the southern Puget Sound coast, including Seattle's King County, was ranked in the Environmental Protection Agency's (EPA) 2002 Average Risk Level Hazard Index's highest category for non-cancer respiratory risk, alongside Los Angeles County, and this was after a 42% reduction in air toxins between 1999

and 2002. King County's total average suspended particulate matter (TSP) was $53.9 \mu\text{g cm}^{-3}$ in 2009, which was actually higher than Los Angeles' $53.8 \mu\text{g cm}^{-3}$ (Wu et al. 2009). The Seattle, Tacoma, and Olympia region earned a dubious 17th on the American Lung Association's Short-term Particle Pollution (24-h PM2.5) report in 2013, ahead of Harrisburg and Allentown, PA, Phoenix, AZ, and San Diego, CA (Billings et al. 2013). Pollution aside, the iconic stratus of Seattle, WA and the Puget Sound Basin are world famous. Additionally, Seattle Tacoma International Airport (KSEA), Bellingham International (KBLI), and Victoria International (CYYJ) on southern Vancouver Island have hosted a novel in-situ sensing program, Tropospheric Airborne Meteorological Data Reporting (TAMDAR, Gao et al. 2012), which will be discussed in section 2.4.

The location of Joint Base Lewis-McChord (JBLM, a.k.a. KTCM), near the most polluted portions of the PSB around Tacoma, presents another benefit to studying forecast aerosol-cloud effects in this region. Frequent training flights of U.S. Army and Air Force helicopters traverse the southeastern portion of the PSB on the way to various locations such as Gray Army Airfield (KGAF) and the Yakima Training Range east of the Cascade Mountains (Fig. 3). Personal communication with U.S. military weather personnel and aviators with operational experience in the region provided insight into the frequent problem of stratus-related mission cancellations and crew endangerment during flights from JBLM to the Yakima Range. Studying the forecast changes of stratus in that region could potentially have real-world application to addressing a very real and immediate forecast challenge.

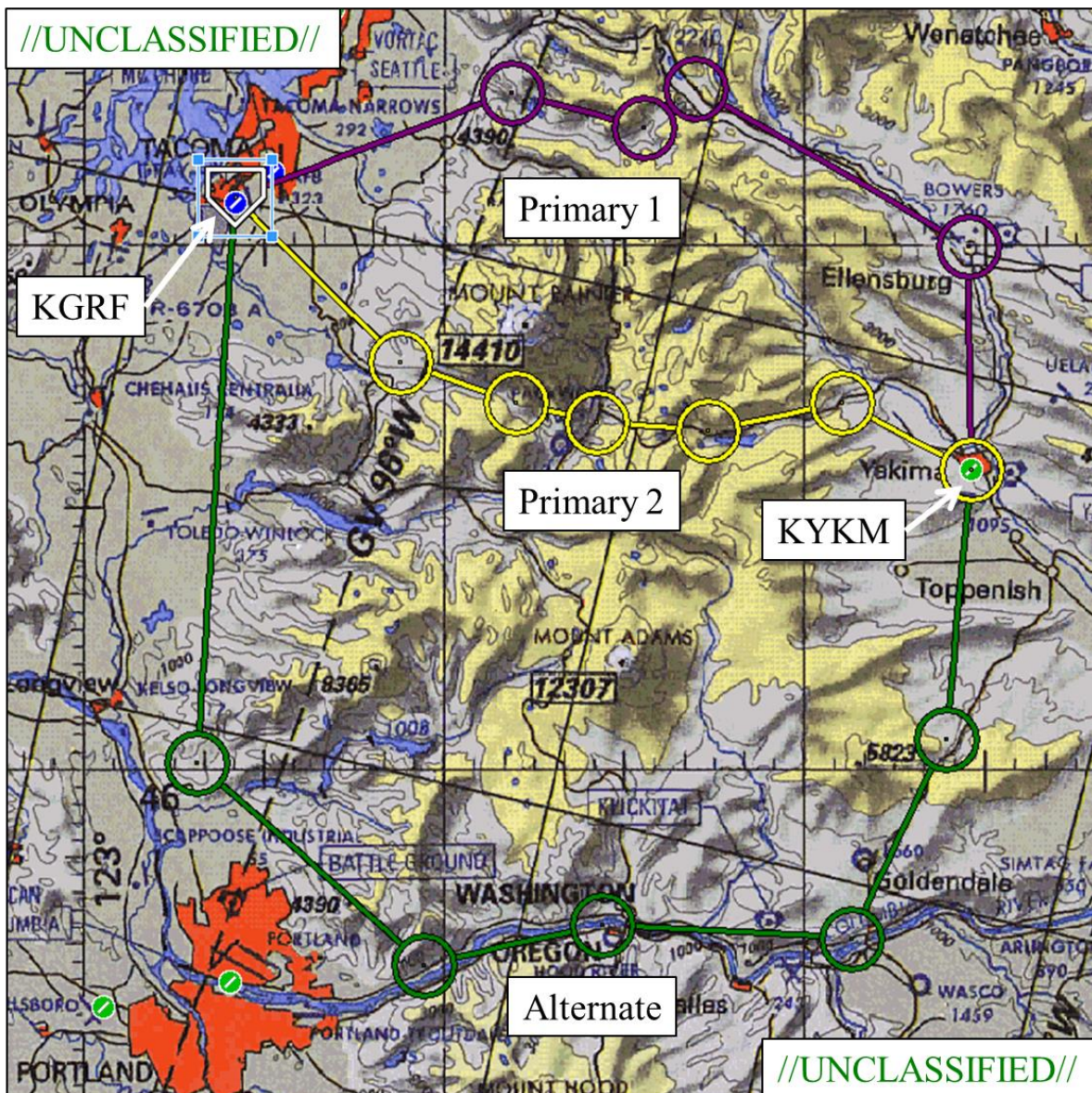


Figure 3 Topographical map indicating two primary northerly routes (purple and yellow) and one backup route of flight (green) for helicopter crews transiting from KGRF to KYKM for military training missions (Image courtesy of P. Dulfer).

The mid-latitude location of the PSB limits the time of year from which stratus cases can be selected, favoring warm season events to isolate stratus events with only liquid cloud water. In the months of June, July, and August, the Pacific High reaches its northernmost

point and is at its strongest, deflecting the mean storm track into Canada. As a result, the fewest migratory lows and synoptic-scale air mass changes take place in the summer than any other season (14WS, 2015). This lends to the more stagnant synoptic patterns under the persistent surface anticyclone in the eastern Pacific. Climatology indicates ceilings below 5,000 ft occur within an hour of sunrise greater than 50% of summer days (Fig. 4). Ceiling and visibility below 3,000 ft and 3 mi are present at sunrise 33 to 41.5% of the time at KSEA (Table 1) (14WS 2015).

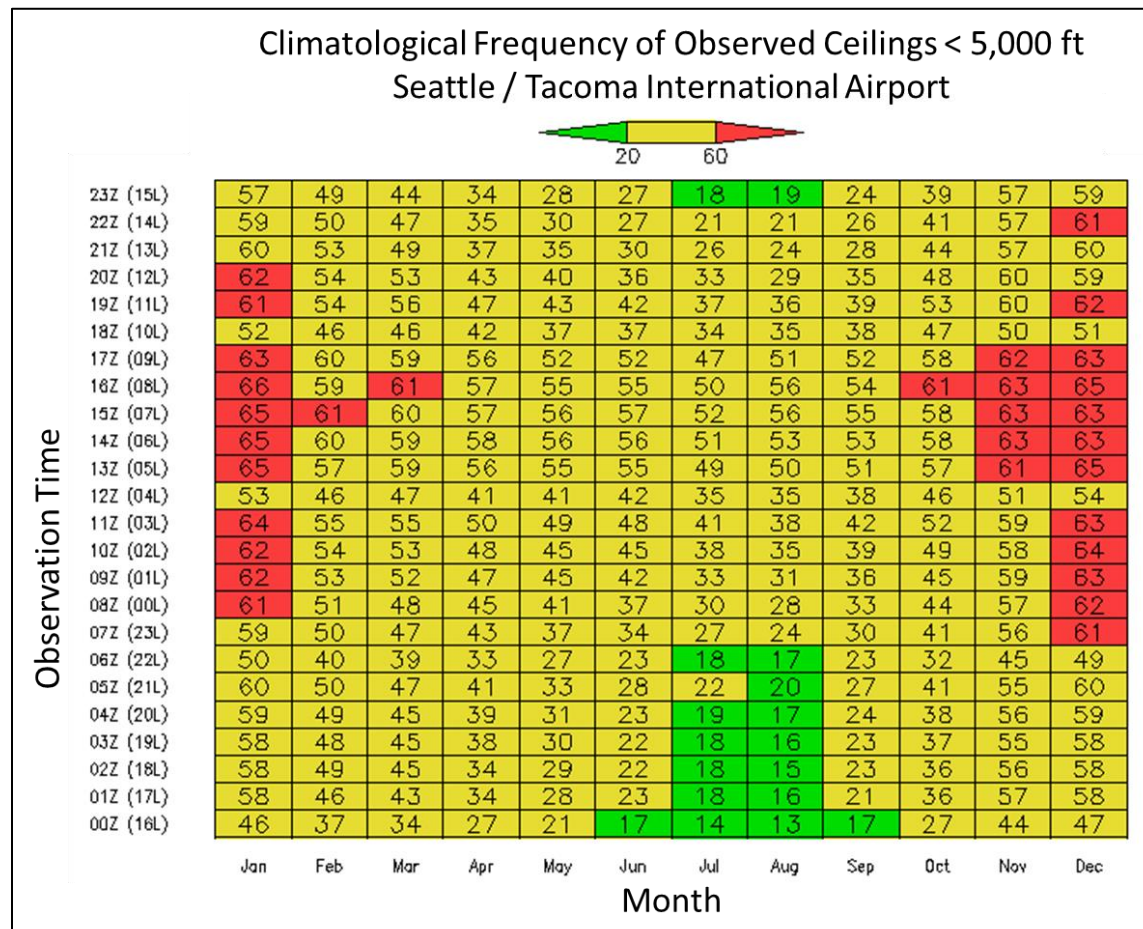


Figure 4 Climatology of ceiling height occurrence below 5,000 ft at KSEA by percent of observations of given times UTC (local) and months of the year (14WS 2015).

Table 1 Seattle / Tacoma International Airport frequency of either ceiling below 3,000 ft or visibility less than 1 mile (1600 m) or both. Given by percent of occurrence during 3-hourly local time periods and month of the year (14WS 2015).

	Jan	Feb	Mar	Apr	May	Jun	Jul	Aug	Sep	Oct	Nov	Dec	Ann
14-16 LST	37.7	22	16.1	9.9	7.7	6.2	4.1	4.8	6.7	16.8	26.1	31.1	15.8
17-19 LST	37.1	25.1	18.2	10.5	6.5	6.7	2	4.3	7.5	15.9	25.1	28.6	15.6
20-22 LST	39.1	24.9	22.6	18.8	11.7	11.5	5	6.2	11.8	18.6	28.3	33.9	19.3
23-01 LST	43.3	33.7	28.4	26.8	20.2	22	12.3	15.2	18.7	27.2	28	37.6	26.1
02-04 LST	47.1	35.2	31.4	31.9	27.4	33.1	26.1	28.6	27.4	35.5	31.5	42.7	33.2
05-07 LST	48.6	38.6	34	36.7	33.2	41.5	37.3	37.5	40.6	40.5	39	41.5	39.1
08-10 LST	49	34.8	35.1	33.4	27.8	35.5	32	29	34.3	38.3	36.9	37.3	35.3
11-13 LST	44.8	28.7	23.7	15.9	13.1	14.5	12	12.4	15.5	24.4	30	33.2	22.4
All Hours	43.3	30.4	26.2	23	18.4	21.4	16.3	17.2	20.3	27.1	30.6	35.7	25.8

2.1.1 Case Study Selection

Stratus events were adequately common in the summers of 2013 and 2014. Testing of these stratus events for the effect of cloud-aerosol interaction, particularly the cloud lifetime effect, required cases in which the primary stratus dissipation mechanism was shortwave radiational warming, as discussed in Chapter 1. Through passage aloft, indicative of cold advection, could prematurely dissipate the stratus by weakening the subsidence inversion or drying the cloud layer. It was essential that the selected cases feature no overlying cloud layers, which could prevent incident solar radiation from reaching the ground or the top of the stratus layer unfiltered, thereby artificially slowing dissipation. This would also contaminate satellite imagery and hamper later model comparison. Precipitation would indicate large droplet growth and vertical velocities beyond our target threshold, and would accelerate stratus dissipation. The University Center for Atmospheric Research (UCAR) meteorological case study selection kit (Ahijevych 2015) provided a means by which to

apply a funnel-type approach to case elimination using satellite imagery, upper-air, and surface analyses.

During the summers of 2013 and 2014, 58 stratus events occurred. Stratus cases occurring within 24 hours of frontal passage, coincident with any overlying cloud, or in which an upper level trough was analyzed to pass near the PSB near dissipation time were eliminated using the UCAR imagery. The remaining 32 cases were ranked greatest to least according to visual approximation of horizontal coverage of the stratus layer. Meteorological Aviation Routine (METAR) observations for 10 reporting stations in and 3 stations around the PSB obtained from the U.S. Air Force's 14th Weather Squadron (14WS, formerly the Air Force Combat Climatology Center) in Asheville, NC, were used to filter the remaining days. An exhaustive examination of over 10,000 observations for these locations resulted in a list of 13 case days in which no precipitation or non-stratus clouds (except fog) were observed. These 13 days were further stratified by the number of observation locations which observed stratus on each day, revealing that 9 stratus events covered every observing location, and another 4 covered more than 75% of locations. Analysis of the observations for these 13 days shows that there is a large deviation in mean sea level pressure (MSLP) tendency between case days. As stratus dissipation typically occurs within a few hours of 1800 UTC in the climatology from 14WS, the 13 potential case days were ordered least to greatest by 24-hour MSLP change at 1800 UTC. The resulting distribution of case days by pressure change was prioritized such that case days could be taken from a representative sample of pressure tendency variance and modeled in a timely manner. This was done to minimize any pressure tendency signal contribution to the variability of stratus dissipation time, which could

dominate any aerosol-cloud interaction signal. Control runs for 9 of the 13 remaining cases revealed the inability of the default model to consistently forecast stratus in the PSB during days in which pressure change is less than 1 to 2 hPa per 24 hours, with the exceptions of 6 June and 7 July 2014, during which the control run stratus decks did not cover all 11 observation locations in the PSB. The control run only produced stratus in the PSB on the days in Table 2.

Table 2 Final case days for which tests were run, with associated 24-hour pressure change observed at 18 UTC and the percentage of available METAR surface stations which observed the event.

	20130718	20130720	20130721	20130722	20140605	20140707
Δ MSLP	2.9	-2.7	-3.3	2.6	0.6	-0.9
Sites	100%	100%	100%	100%	82%	91%

2.2 Configuration of the Weather Research and Forecasting Model

The Weather Research and Forecasting (WRF) Model Advanced Research WRF (ARW) core is a modern mesoscale numerical weather prediction (NWP) system developed and made freely available to the public by the National Center for Atmospheric Research (NCAR), the National Centers for Environmental Prediction (NCEP), and several other parties. The WRF model is used in both research and operational forecasting. Since the phase out of the Mesoscale Model 5, WRF has been the primary forecast tool of U.S. Air Force aviation weather forecasters around the world. Namelist selection options make the model

extremely versatile and adaptable for simulation and forecast of phenomena on very small or very large scales. Additionally, the advent of the Thompson and Eidhammer (2014) “aerosol aware” microphysics scheme in WRF version 3.6 makes this version suited to test cloud-aerosol interaction. This means potentially beneficial WRF settings or modifications found in this study might be quickly and directly applied to real-world forecasting.

2.2.1 Model Domain

As PSB stratus is the central figure of this study, the model domain will be situated so as to provide the best framework possible for capturing the initial and lateral boundary conditions suitable for stratus development in the PSB. As these events require a broad surface anticyclone in the northeastern Pacific Ocean, the outer domain (Fig. 5) was located to ensure capture of the analyzed anticyclone center in the initial conditions.

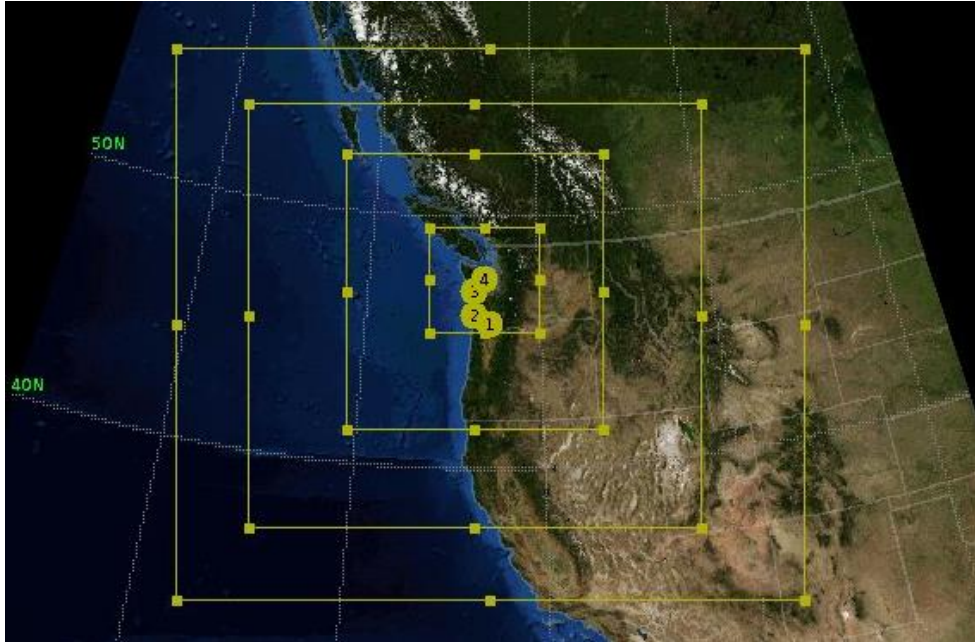


Figure 5 Map projection of WRF domains used in this study.

Large domains combined with small grid lengths are computationally cost prohibitive. Because the point of the study is to resolve aerosol-cloud interaction in stratus, the study domain must have fine enough grid spacing to account for terrain of the PSB and compare forecasts to observations. Regarding suitable grid spacing, $2\Delta x$ and $3\Delta x$ waves are often damped in numerical models, leaving $4\Delta x$ waves as the smallest possible resolvable wave, although resolution would be poor at best. Walters (2000) emphasized “due only to the geometric relationship between the numerical grid and the true solution, as many as 10 grid points may be required to assure a reasonable (e.g., greater than 95%) representation of the true solution’s amplitude . . . As a result, the shortest wavelength that can be effectively resolved by a gridpoint numerical model may be considerably longer than $4\Delta x$ ” (Walters 2000). This relationship dictates the minimum reasonable horizontal resolution required in an

inner model domain is $5\Delta x$. The spatial scale of stratocumulus is on the order of 1000 m in the vertical and 5 to 30 km in the horizontal (Wood 2012). Stratus scales similarly to stratocumulus in the vertical but, by definition lacks the cellular cumuliform inhomogeneity of stratocumulus so is nearly uniform in the horizontal. Therefore a reasonable horizontal grid spacing to resolve stratus on minimum horizontal scales of 20-30 km would be 4 km. Thus the inner domain of this study is 4km. There are 72 vertical sigma levels in all domains, logarithmically converged at the bottom and top of the troposphere such that spacing of the bottom model level is 50 to 90 m above the surface, or approximately $10\Delta x$ for stratus. Two outer nest grids were spaced at 12 km and 36 km to ease the numerical integration of potentially coarse initial and lateral boundary conditions.

2.2.2 Initial Conditions

Initial conditions are critical to model output quality (Coniglio 2013). For the purposes of this study, an initial condition data set must mimic the operational forecast setup as closely as possible. The reasoning for this approach is that the outcome of this study would mimic what a forecaster would expect if they were to have used the model changes of these tests for their operational forecasts. This makes any forecast quality statements about model output verification against real-world observations more reasonable from an operational forecast perspective. Personal operational forecast experience utilized a model configuration of the Air Force Weather Agency (AFWA) which included a 3-dimensional variational assimilation (3D-Var) of directly and remotely sensed meteorological and physical variables. A global model such as the 0.5 degree GFS (Global Forecast System) or global WRF was run from the initialization time and the global model fields provided initial

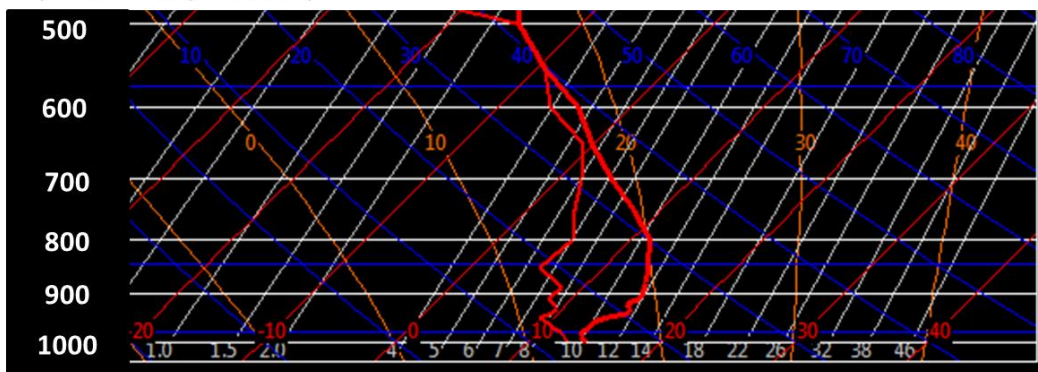
and lateral boundary conditions to 45 km, 15 km, and 5 km nested WRF runs, updating the boundary conditions for the inner domains every 3 or 6 h with freshly forecasted global data. For that reason, a data set for our historical case days used one initial and six-hourly forecast times from the initial analysis time, through the duration of the run. In the interest of balancing initial condition operational realism with a quality, high resolution dataset, two data sets were considered.

The European Re-Analysis (ERA) Interim re-analysis is the pre-eminent choice for initial conditions due to the advanced 4D-Var assimilation process used, along with superior dynamics and physics of the European Centre for Medium-Range Weather Forecasts (ECMWF) global model used to balance errors and discontinuity in observations (Dee et al. 2011). The ERA-Interim is a continuously updated global reanalysis of surface and upper air data going back to 1979. One detriment of its global coverage is the ~80 km grid length, which is rather coarse compared to the 36 km outer nest of the model setup of this study. One benefit of this dataset is the extensive 60 vertical levels of observed information it uses, from the surface up to 0.1 hPa. The ERA-Interim analysis data for this study was obtained from the NCAR and University Center for Atmospheric Research (UCAR) Computational & Information Systems Lab (CISL) for the initial time and every 6 h following, out to the 42-hours of each model run. However, one limitation of using this data in the present study is that each 6 h input interval call retrieves the simulated ERA-Interim data, not a true 6 h, 12 h, or 18 h forecast from the initial time. This provides an immediate bias at the outer edge of the outer domain toward the observed data in each WRF run using the ERA-Interim initial conditions (the ERA-based runs are simulations, as opposed to forecasts). This makes a

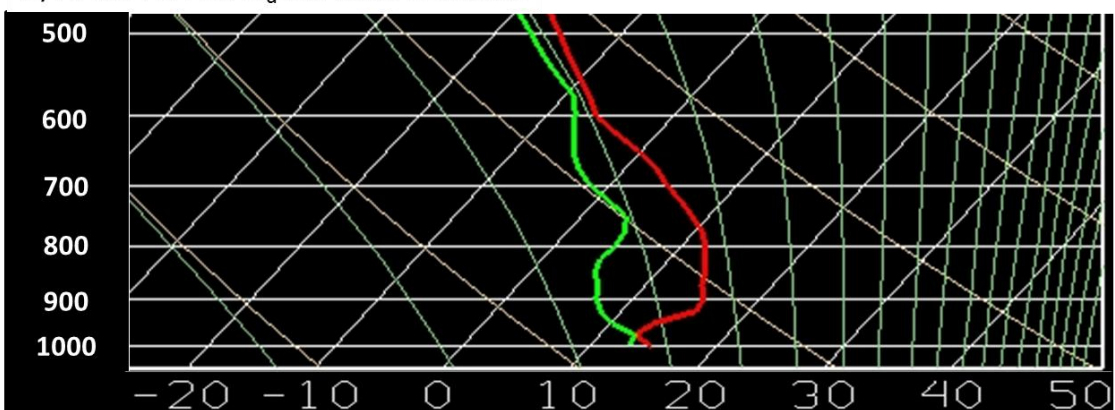
realistic comparison between WRF forecasts in this study and those of an operational forecast less than an equitable comparison. Despite this caveat, comparison of the ERA-Interim's resolution and quality to the paltry 26 vertical levels from the surface to 10 hPa, 0.5 degree (~42 km on a Mercator projection) grid spacing of the NCEP Global Forecast System (GFS, NCDC 2015), justifies preference for testing with the ERA-Interim in this study. However, the ERA-Interim does not include TAMDAR observations (Dee et al. 2011).

However, a quick comparison of a series of observed TAMDAR soundings at KSEA with the initial model time of the ERA-Interim for the stratus event on 18 July 2013 revealed a potential dry and warm bias for the southern PSB in the initial conditions (Fig. 6). This prompted comparison with another initial condition dataset.

A) TAMDAR (Descent)



B) NAM218 100 N_d run 00hr Forecast



C) ERA-Interim 100 N_d run 00hr Forecast

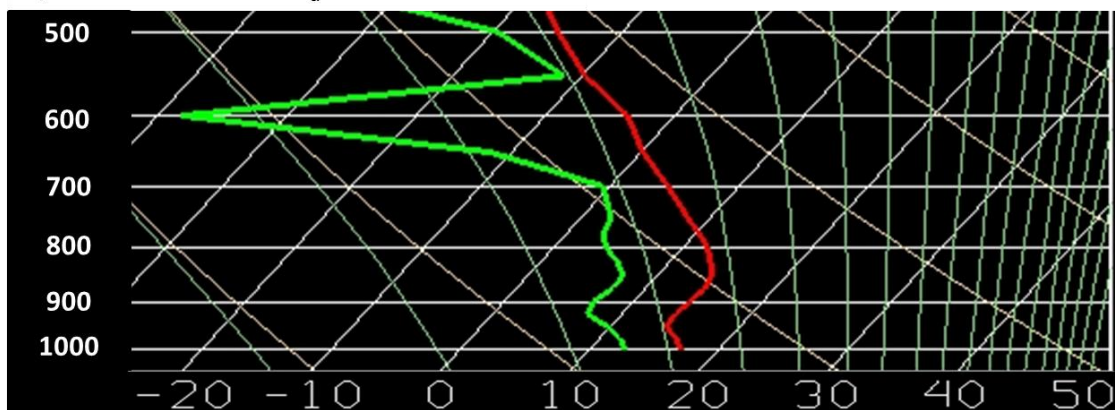


Figure 6 Comparison of Skew-T log P diagrams observed by TAMDAR (A), forecast by WRF 100 with NAM218 (B), and with ERA-Interim (C) as initial conditions for 17 July 2013 at 1200 UTC, the 00 hour forecast. Note the differing temperature scales at the bottom of the TAMDAR versus the forecast diagrams.

The North American Model (NAM), grid 218 is a 12 km analysis and forecast data set run derived from the operational NAM. It has 38 vertical levels from the surface to 10 hPa and encompasses much of North America and the northeastern Pacific. Additionally, the NAM initial conditions along with forecast lateral boundary conditions allow the WRF to be run in forecast mode, as each 6-hourly input call in the WRF forecasts of this study retrieves NAM forecast data. Although it uses 3D-Var data assimilation, the NAM initial conditions compared favorably to the observed soundings over KSEA for ambient and wet bulb temperature, as well as inversion height, with no spurious mid-tropospheric dry layer (Fig. 6b). The favorable comparison of the NAM dataset to the ERA-Interim with respect to observations for one time, in one location does not condemn the body of ERA-Interim data to a status inferior to the NAM in general. However, these observations suggest that the deficit in assimilation process and dynamic representation quality of the NAM compared to the ERA-Interim may be overcome by the NAM's fine horizontal grid spacing. These observations warrant tests for sensitivity to initial conditions which compares WRF output data using both the ERA-Interim and NAM data sets. Some results of these tests are discussed in Chapter 3.

2.2.3 Physics Choices

Properly testing the efficacy of aerosol awareness in WRF model aerosol-cloud interactions requires control and experiment model setups in which only the number of available CCN or cloud droplet number concentration changes between runs. Testing cloud-aerosol interaction in an operational setup of WRF in this study will incorporate the Thompson and Eidhammer “aerosol aware” MP scheme (WRF version 3.6 microphysics

option 28, TE14 hereafter). This scheme includes the default prescription for hygroscopicity parameter, κ , of 0.4. A coastal urban area such as Seattle, WA, might physically represent a middle ground between Feingold and Heymsfield's (1992) global means for maritime and continental hygroscopicity. The prescribed κ value in the default TE14 is 44% lower and 48% higher, respectively than those global means. However, 0.4 is 0.095 or ~20% less than the mean global value. In order to compare the results of TE14 output with that of an "aerosol ignorant" scheme, the predecessor T08, namelist option 8 is used for control runs. These choices necessitate other physics option changes.

Initially after download and compilation of WRF 3.6, pertinent namelist options are set for no longwave (LW) or shortwave (SW) radiation, no planetary boundary layer physics, and no cumulus physics (CP) parameterization. Because the TE14 MP scheme is designed to pass variables to the RRTMG SW and LW radiation physics options (Thompson and Eidhammer 2014), namelist option 4 is chosen for both. In the effort to treat model stratus cloud-aerosol interactions in the most physical possible way, a PBL scheme which represents entrainment in a stable, low shear environment is preferred. As the stable environment and moderate entrainment rate in STBL situations is better represented by local closure, the Mellor–Yamada–Janjic (MYJ) PBL scheme was used for all control and experiment runs. A sensitivity study comparing Yonsei University (YSU) and MYJ PBL schemes in one stratus case is briefly discussed in Chapter 3. The need for convective parameterization depends on stability of the situation under study and whether the domain grid length can resolve cumulus clouds. As cumulus clouds have a horizontal scale of > 4 km (Cotton and Anthes 1989) convective parameterization is turned off and convective motions calculated explicitly within

the 4 km domain. The updated Kain-Fritsch CP scheme (Kain, 2004) is used for the middle and outer domains.

2.2.4 Model Preparation for Aerosol Climatology Use

In order to prepare the initial conditions for use by WRF 3.6, significant pre-processing is required, particularly of the initial condition aerosol concentration climatology. In order for this formulation to be widely tested, Thompson and Eidhammer provided a global dataset for use in conjunction with GFS, AWIP, and ERA analyses. These three aerosol formats use the same GOCART dataset, interpolated to the levels and grids used by the GFS, AWIP, and ERA, respectively. For this study, use of the ERA-Interim initial condition was seamless, following the instruction of the WRF User's page (<http://www2.mmm.ucar.edu/wrf/users/wrfv3.6/mp28.html>). The sequence of events in the WRF Pre-processing System (WPS) includes selecting namelist.input microphysics option 28, adding "use_aero_icbc = true" to the &physics section, and inserting into the namelist.wps &metgrid section a call identifying the climatology file as the aerosol data source for use in building met_em files, which are still in isobaric coordinates, but have been interpolated horizontally to the model grid. These met-em files are passed on to WRF real.exe as usual for vertical interpolation. Use of the GFS or AWIP climatological aerosol input was information cost-prohibitive due to the low number of vertical levels in each (26 compared with the ERA-Interim. The NAM218 grid includes 38 vertical levels, but 14 of them differ from the input aerosol files of the AWIP (the NAM parent domain) aerosol climatology grid. Running real.exe will only vertically interpolate input data if all the input data are on the same pressure levels. At the time of this writing, a potentially helpful feature

of metgrid.exe in WPS, the vertical interpolation option (WRF User Guide, Ch. 3, option 20), is not implemented. Therefore Dr. Gary Lackmann devised an intermediate step for proper incorporation of climatological aerosols with the NAM218 input. Use of the mod_levs.exe utility in WPS yielded the proper number of vertical levels in the NAM218 intermediate files, at the cost of the 550 and 650 hPa analysis levels. The prepared NAM218 data were horizontally interpolated to the model grid by metgrid.exe as usual. Then Dr. Lackmann's custom interpolation created the aerosol variable on the proper pressure levels and linearly interpolated aerosol data to those levels within each met_em input file. These met_em files are passed to WRF real.exe as usual. A comparison of the original aerosol profile and those interpolated to the NAM218 pressure levels is shown in Figure 7.

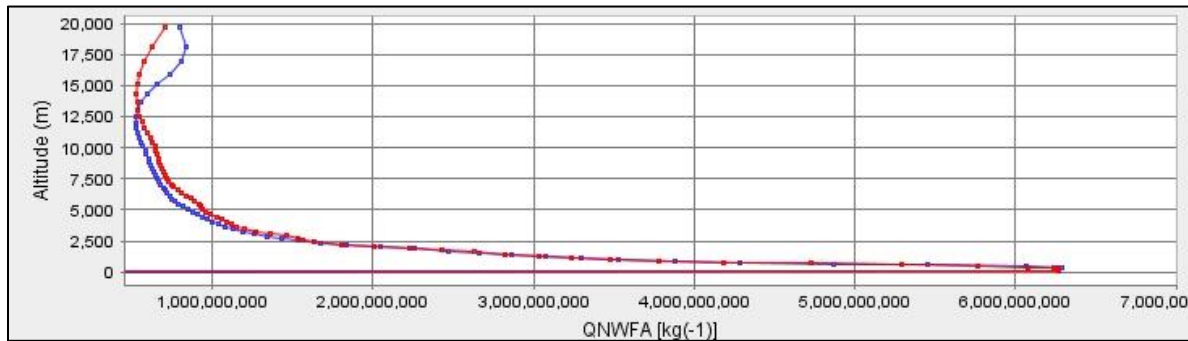


Figure 7 Vertical profiles of water-friendly aerosol initial condition over Seattle, WA from the ERA aerosol input file interpolated to the ERA (red) and NAM218 (blue) pressure levels for input to WRF. Values shown are aerosol $\# \text{ kg}^{-1}$ and altitude in meters.

The Seattle-Tacoma area is not the pristine coastal woodland habitat some people think it to be. Figure 8 shows the column-total boundary layer content of the July climatological mean concentration of water-friendly aerosols ($\# \text{ kg}^{-1}$) used in the Aero run as

calculated with the GOCART model of Colarco et al. (2010), and processed for use as a model initial condition (Thompson and Eidhammer 2014).

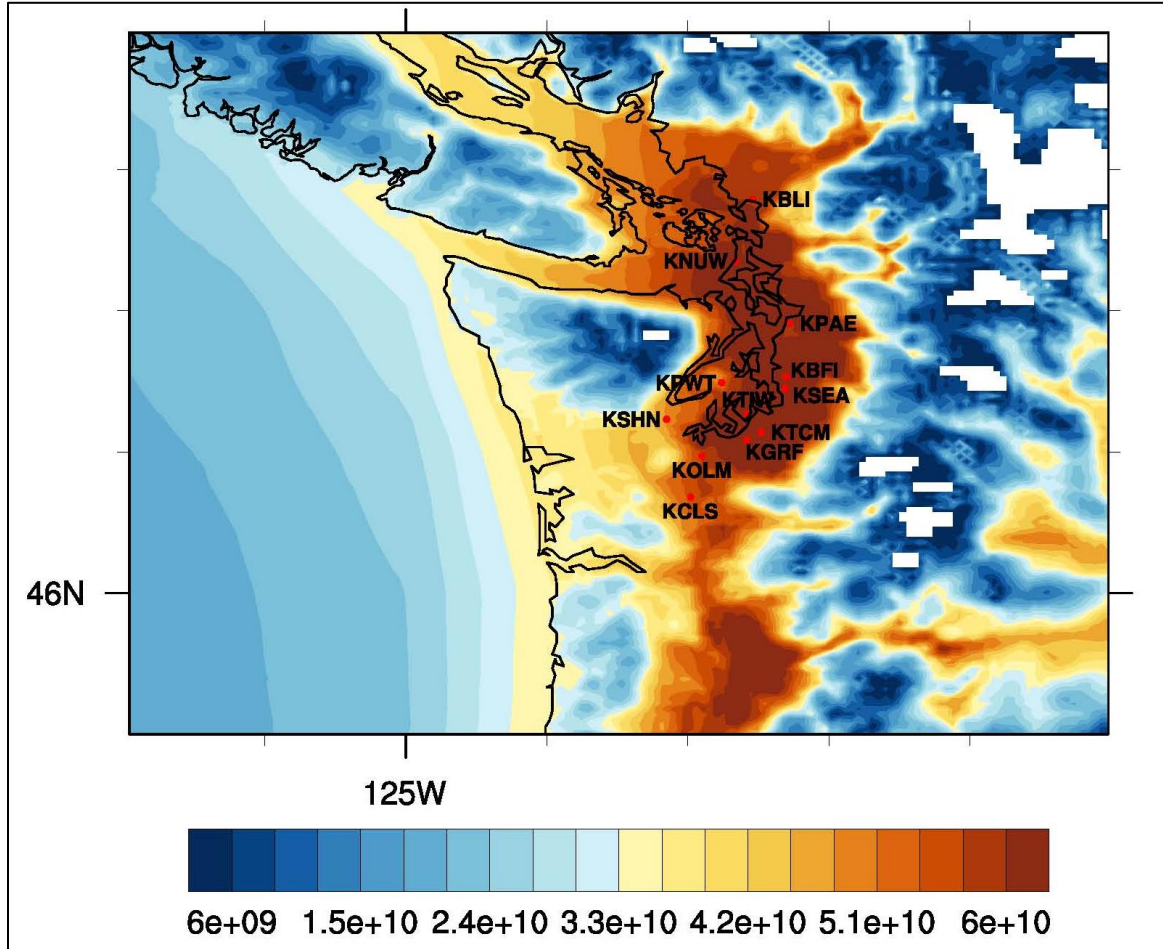


Figure 8 Water-friendly aerosol ($\# \text{ kg}^{-1}$) initial condition in Aero runs. Values are mean aerosol concentrations (number per kilogram of air) as modeled by Colarco et al. (2010) using GOCART. Values shown are column totals from the surface to 850 hPa based on inversion base heights observed in this study, summed to indicate initial BL content.

2.3 Cloud Physical and Radiative Properties of Interest

The study of cloud forecast change by explicit cloud droplet number calculation examines several cloud properties. Owing to the fact that this is a new model capability, it is

important to check whether TE14 produces the expected changes in cloud droplet number. This factor influences whether TE14 will have the expected radiative property changes observed in polluted clouds. Analysis of model cloud shortwave radiation transmissivity indicates whether any change in droplet number concentration or mean radius has the expected albedo change observed in polluted clouds. In this study, this is measured by comparing the control and experiment ratios of downwelling shortwave radiation to the amount of cloud water in a model cloud ($\text{W m}^{-2} / \text{kg kg}^{-1}$). Additional information is gleaned by examining the resulting difference in downwelling shortwave radiation observed at the ground between model runs. As these fields can give misleading results due to simple cloud location difference between runs, cloud water and shortwave radiation fields are smoothed using a Gaussian weighted filter smoothing utility. This method is chosen over area averaging because the expected variation in cloud droplet number over Pacific stratocumulus may have a different sign than that over inland areas, and area averaging will mask any such signal.

Cloud physical properties which inform this study include differences in cloud water content and cloud droplet number concentration, as examined using difference fields and vertical profiles of various runs. Examination is also made of cloud coverage, base height, top height, geometric thickness, as well as onset and dissipation times as an operational forecast would require. Cloud coverage is examined by visual comparison with satellite imagery and by comparing forecast fractional coverage with METAR reports. Fractional coverage is tested for binary conditions of greater than or equal to half the sky (broken or overcast conditions) and reported in 2 by 2 contingency tables. Cloud top heights are

measured against TAMDAR observations. Owing to suspected low height and excess cover biases in METAR compared to TAMDAR, cloud base heights are verified against METAR values with an additional look to cloud base verification comparison with TAMDAR, where available. Statistical comparison is made by the absolute difference and absolute error values for heights over time, and for the root mean squared error for daily averaged heights at each location, required by the large variations observed and strict adherence to measuring only cloud heights of “ceilings,” as discussed in the next section. The absolute mean daily difference, defined as the mean daily forecast value minus the mean daily observed value, measures error between TAMDAR and model cloud geometric thickness.

Stratus onset and dissipation timing error is measured using the mean absolute error (MAE) which is computed by taking a difference between the forecast time of an event and the observed time, then averaging the absolute values of those times. Results are presented for each location to identify any location bias, and for a model run as a whole to identify potential model bias or effectiveness. Location does contribute heavily to the timing error signal for the case analyzed in this study, therefore two measures of location bias are used. Comparison between models looks at locations organized by initial water-friendly aerosol concentration at the surface (Table 3).

Table 3 METAR locations used in this study, organized by initial aerosol concentration (# kg⁻¹) from least to greatest.

Name	ICAO	Latitude	Longitude	Elevation	Aerosol (x10 ⁹ # kg ⁻¹)
Whidbey Isl. NAS	KNUW	48.35	-122.66	47	5.53
Paine Field	KPAE	47.91	-122.28	606	5.98
Chehalis Centralia	KCLS	46.68	-122.98	176	5.72
Sanderson Field	KSHN	47.23	-123.15	273	5.56
Bremerton National	KPWT	47.49	-122.76	444	6.05
Boeing Field	KBFI	47.53	-122.30	21	6.25
Seattle/Tacoma Intl	KSEA	47.45	-122.31	433	6.31
Olympia	KOLM	46.97	-122.90	209	6.17
Tacoma Narrows	KTIW	47.27	-122.58	292	6.58
Gray AAF	KGRF	47.08	-122.58	302	6.77
JB Lewis/McChord	KTCM	47.14	-122.48	322	6.67

2.4 Observational Data

Satellite imagery is the comparison data set with the most horizontal coverage. Due to the low, warm stratus being the focus of this study, visible satellite data (0.6 μm) collected by GOES15 geostationary satellite (NCDC 2015) is preferable for this study. Considerable effort was made to reconcile the satellite data with the model grid for pixel-to-pixel comparison of cloud coverage, but no amenable method was found by the time of publication. Therefore, only a qualitative comparison with satellite data is presented here, with METAR and TAMDAR used for statistical evaluations.

The most widely available surface observational data set for the verification purposes of this study is the METAR data set for the 11 PSB locations. This study utilized over 10,000 of the nearly 45,000 METAR observations provided generously by the 14WS (2015). The

METAR locations used here provide a minimum of 24 hourly observations per day of wind, temperature, dew point, pressure and most directly applicable here, cloud coverage and base height. Cloud coverage and base height observations are reported any time ceiling coverage or height fall below or increase to equal or exceed set criteria. These observations are called SPECI, and in this study are used only for onset and dissipation timing (Chapter 3). Sky conditions in METAR are observed using 0 through 8 oktas of the sky using the labels clear, few, scattered, broken, and overcast (CLR, FEW, SCT, BKN, OVC) to denote cloud coverage of 0, trace to 2, 3 to 4, 5 to 7, and 8 oktas, respectively. Each okta represents 12.5% of the sky when viewed as a celestial dome. The celestial dome is defined as the visible horizon from an observation point, usually a central location on an air field. Due to earth's curvature, the celestial dome has an approximate radius of 12 mi or 19 km. However, METAR cloud observations use laser beam ceilometers orthogonal to the horizontal plane, which account for cloud coverage and height every 30 minutes (AFMAN 15-111 2015). For this reason, an unknown amount of error exists between the model forecasts for coverage, height, and timing in this study. This study observed sensitivity to the definition of the coverage of a METAR cloud observation due to the horizontal area over which model data must be gathered to be representative. A model radius of 19 km about a location resulted in additional cloud base error values due to the wider horizontal sample, yet METAR ceilometer values are those immediately above the sensor. To balance these two constraints, model data retrieval techniques were adapted to gather model cloud values at each METAR location within a radius which included 3.5 grid lengths, representing a celestial dome of radius 14 km or 8.7 mi. Heights in METAR observations are made in hundreds of feet AGL

but model output and TAMDAR data have been retrieved in hundreds of feet above mean sea level (MSL). Therefore, METAR observed heights have been added to station elevation for the final height comparisons at each location.

In addition to surface observations, TAMDAR observations provided in-situ measurement of GPS height, temperature, and relative humidity over KSEA and KBFI. This study examined approximately 30,000 TAMDAR observations among the over 650,000 individual observations provided graciously by Panasonic AirDat (2014). These observations are taken on board regional-range aircraft and provide this study with a temperature and dew point profile of the flight path, usually from ~10,000 ft AGL to near ground level. Measurements for this study were taken at a mean interval of 15 seconds, on board aircraft travelling between 120 and 250 kts in their ascent or descent envelopes, which are seen as clover-like loops in the routes plotted in Figure 9. This resulted in a horizontal sample area of radius ~15 miles for heights below this study threshold of 6,000 ft AGL. These values were filtered by a simple radius about KSEA and KBFI, respectively, to gather the pertinent observations used in Chapter 3. To minimize uncertainty, observations were filtered such that only those indicating relative humidity greater than 99.5% were included as cloud. A cloud layer in this data set is defined as a continuous series of observations meeting relative humidity criteria with no missing values, above and below which reasonable dew point depressions were observed. The closest cloud base observation reported at KSEA was 2 mi away. Thus, a sample radius was determined to be 10 mi because of the obvious “cone of silence” of ~2 mi around the center of the airfield resulting from cloud base heights immediately over the airfield being unobservable by TAMDAR. The 10 mi radius criterion

provides adequate horizontal sampling area approximate to that of the model data gathering criteria. Ideally, differences between an aircraft samples from different approach and departure envelopes would be eliminated by time-averaging. However, approach and departure envelopes are determined by air traffic control based on surface wind, ceiling, and visibility such that some corridors may be favored over others for certain periods of time. This means a cloud-free sample on a northwestern approach may miss stratus observed over the southeastern part of the airfield, and is a known weakness. Figure 9 shows a sample of TAMDAR observation distributions for 18 July 2013.

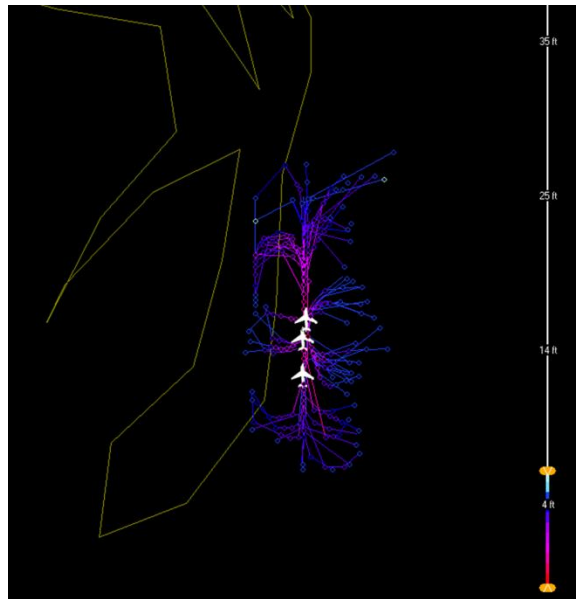


Figure 9 Map of TAMDAR observations for KSEA sampled on 18 July 2013 for flights below 6,000 ft MSL (vertical scale) with cool colors representing heights above 3,000 ft and warm colors representing heights below.

Observation error can be an important source of verification uncertainty in this study. Gao et al. (2012) found TAMDAR observation error comparable to that of rawinsonde

observations (RAOB) for temperature and within 7% on average, but less than RAOB below 700 hPa in the summer. Never the less, it is suspected that sensor wetting may occur such that a sensor departing a cloud layer may have residual moisture on it which leads to error in the next observation. For that reason, only descents were used for cloud top height measurements, and only ascents were used for cloud base measurements. Additionally, some data above, below, and between cloud layers were observed to be contaminated with missing height or relative humidity values. For this reason, any observation profile which included missing data was excluded from use in this study. Eliminating observations due to missing data and possible sensor wetting greatly reduced the number of observations available for comparison to model output. Use of a more sophisticated data assimilation technique may increase the number of observations suitable for comparison, but such means are beyond the ability of the author at this time.

2.5 Limitations and Statistical Significance

Several limitations have been presented thus far, including available cloud observation or analysis data sets, satellite data comparison techniques, and observation error. In addition to these, this study is limited by time. The analysis conducted within the time allowed by personal professional commitments to the Air Force resulted in the presentation here of just one detailed analysis. Additional analysis was conducted on many of the other case days in Table 2, but time does not allow inclusion here. Therefore, summary information of additional case days is presented in the Sensitivity Test section. In all, this study included 52 runs of WRF (each with pre- and post-processing) which compared 2

initial condition data sets, 2 PBL schemes, 2 microphysics schemes, and 4 different configurations of TE14 aerosol characteristics.

For this reason, the statistical significance of the conclusions is limited. Where available, statistics presented are robust for the case under study except in the following ways. The 11 METAR locations and 2 TAMDAR locations all observed the same stratus event. This means the data are neither independent, nor random. Including data from additional case days would alleviate this weakness.

CHAPTER 3

3. Analysis

This chapter examines observed and forecast data with respect to the hypotheses presented in Chapter 1. Therefore, the primary focus is model forecast verification against observations, with an eye to comparisons of default WRF output (hereafter 100) to that of WRF with TE14 aerosol accounting (hereafter Aero) and that of a prescribed order of magnitude increase for the default cloud-droplet number concentration (hereafter 1000).

3.1 Stratus Case 20130718

The 18 July, 2013 1200 UTC 300 hPa chart (Fig. 10a) shows that a low-amplitude upper ridge centered in southern California (CA) extended weakly to Vancouver Island (VI), and closed cyclone over the deep Pacific brought weakly zonal flow over WA. The 500 and 700 hPa charts showed a well-defined ridge axis extension from the Gulf of CA to west of VI. The surface analysis showed a 1025 hPa anticyclone centered ~700 km west of the OR/WA border with a weak ridge extension into northern WA. The lower pressure over eastern WA is likely the result of troughing which is frequently induced lee of the Cascades, and not a major synoptic feature which dominates this case. As high pressure developed late on the 17th, the pressure gradient between the PSB and the Pacific increased. A marine push brought moist, west-southwesterly low level Pacific flow through the Chehalis Gap. Stratus formed in this flow, and is seen as an extension of the large ST/SC field in the eastern Pacific at approximately 0800 UTC (Ahijevych 2015) 18 July. Visible imagery (Fig. 10f) shows the ST field has a relatively high top in the PSB, encroaching approximately 80 km into the Cascades, extending west across the Chehalis Gap to the Pacific, and south across the OR

border down the Willamette River valley where it was predominantly fog. Looping the visible imagery (not shown) reveals this ST deck eroded out of OR from the south and British Columbia (BC) from the north by 1845 UTC. The most visually dense ST remained east through south through southwest of KSEA (Fig. 11a) until complete dissipation by 2245 UTC (Fig. 11b). Surface observations indicate ceiling minima in the PSB ranged from 900 ft AGL at KCLS to 3,300 ft AGL at KNUW.

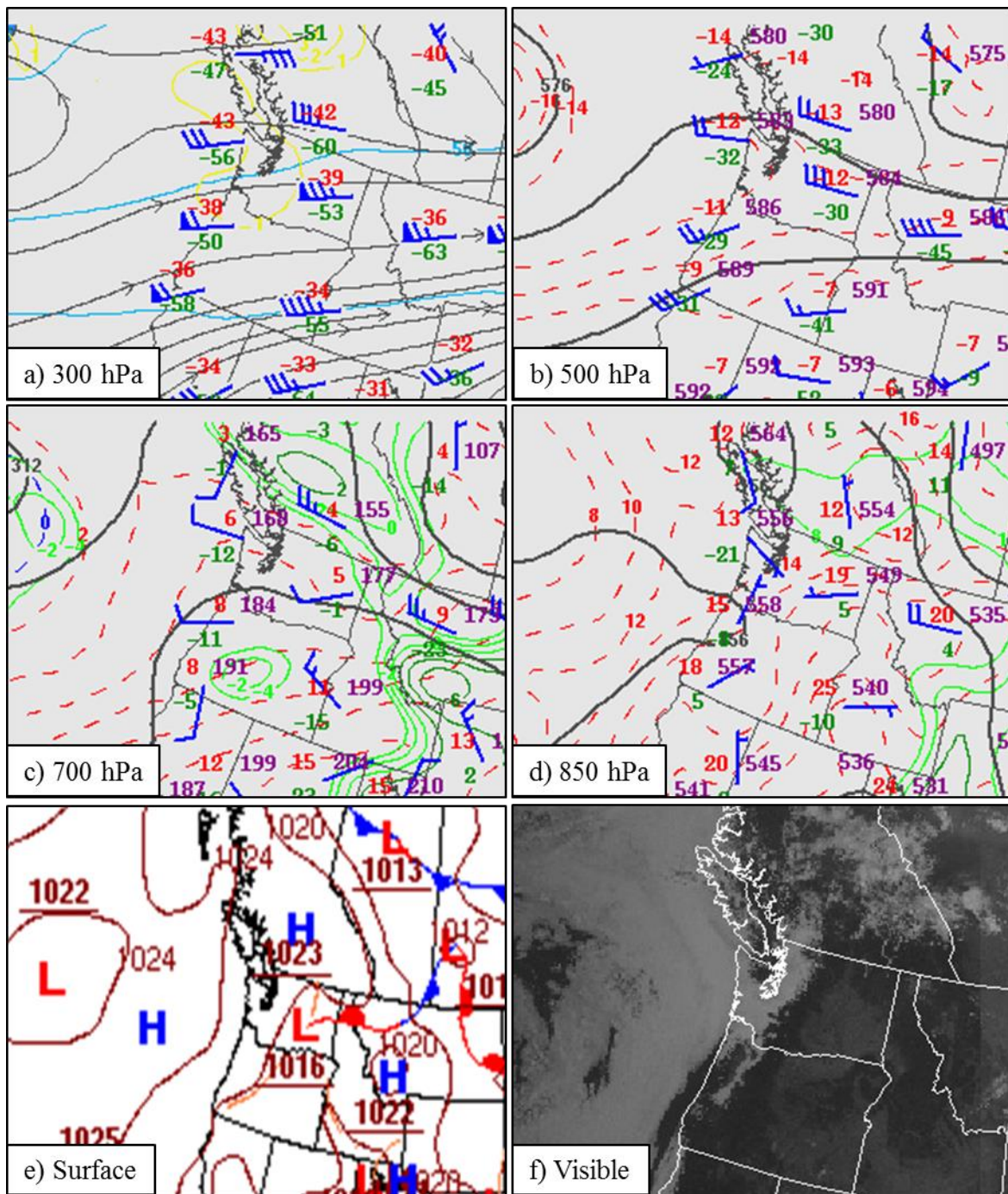


Figure 10 18 July 2013 observed 300 (a), 500 (b), 700 (c), and 850 (d) hPa level and surface (e) charts valid at 1200 UTC and GOES15 visible channel satellite image (f) valid 1515 UTC (Ahijevych 2015, mmm.ucar.edu/imagearchive, WPC 2015, wpc.ncep.noaa.gov/archives/web_pages/sfc/sfc_archive.php).

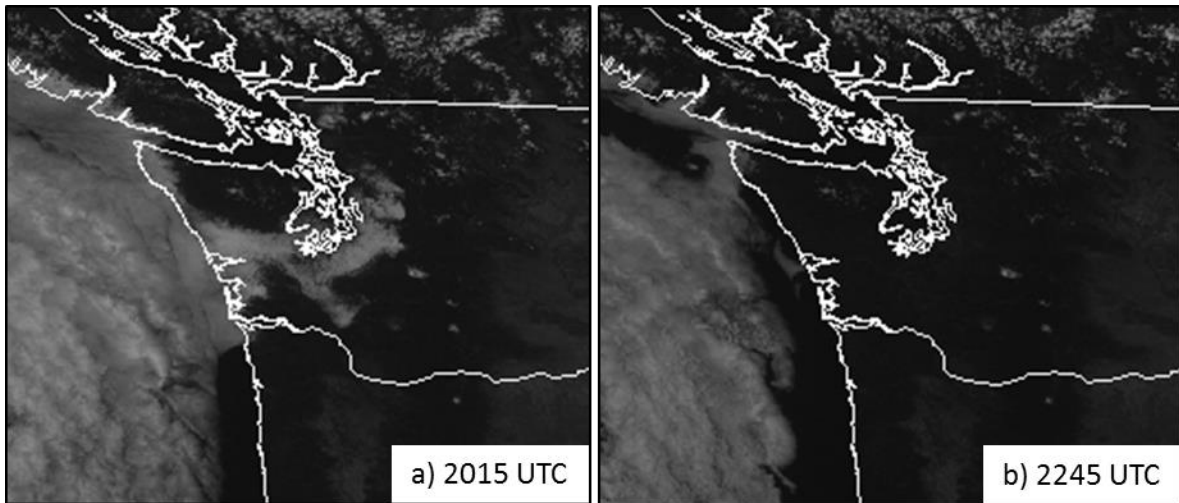


Figure 11 GOES15 visible satellite image valid 2015 (a) Stratus remains along the southeastern PSB and the western Cascade slopes but dissipates by 2245 UTC (b).

The formation, maintenance, and dissipation mechanisms for this event are important determinants as the applicability of any model stratus representation. The 3-hourly observed surface winds in Figure 12 confirm that winds brought a marine push of moist, clean air from the Pacific through the Chehalis Gap toward the southern PSB.

For locations located upwind of the mean pollution center of Seattle-Tacoma (under clean, westerly Pacific flow), surface cloud base height observations (Fig. 13) indicate generally rising cloud base height trends between solar heating (sunrise occurred at 1231 UTC) and dissipation. This suggests heating by insolation as the primary dissipation mechanism during which solar radiation penetrated cloud and warmed the surface, which lifted the LCL to the inversion base or destabilized the stratus layer such that stratus fractured into open stratocumulus and quickly evaporated.

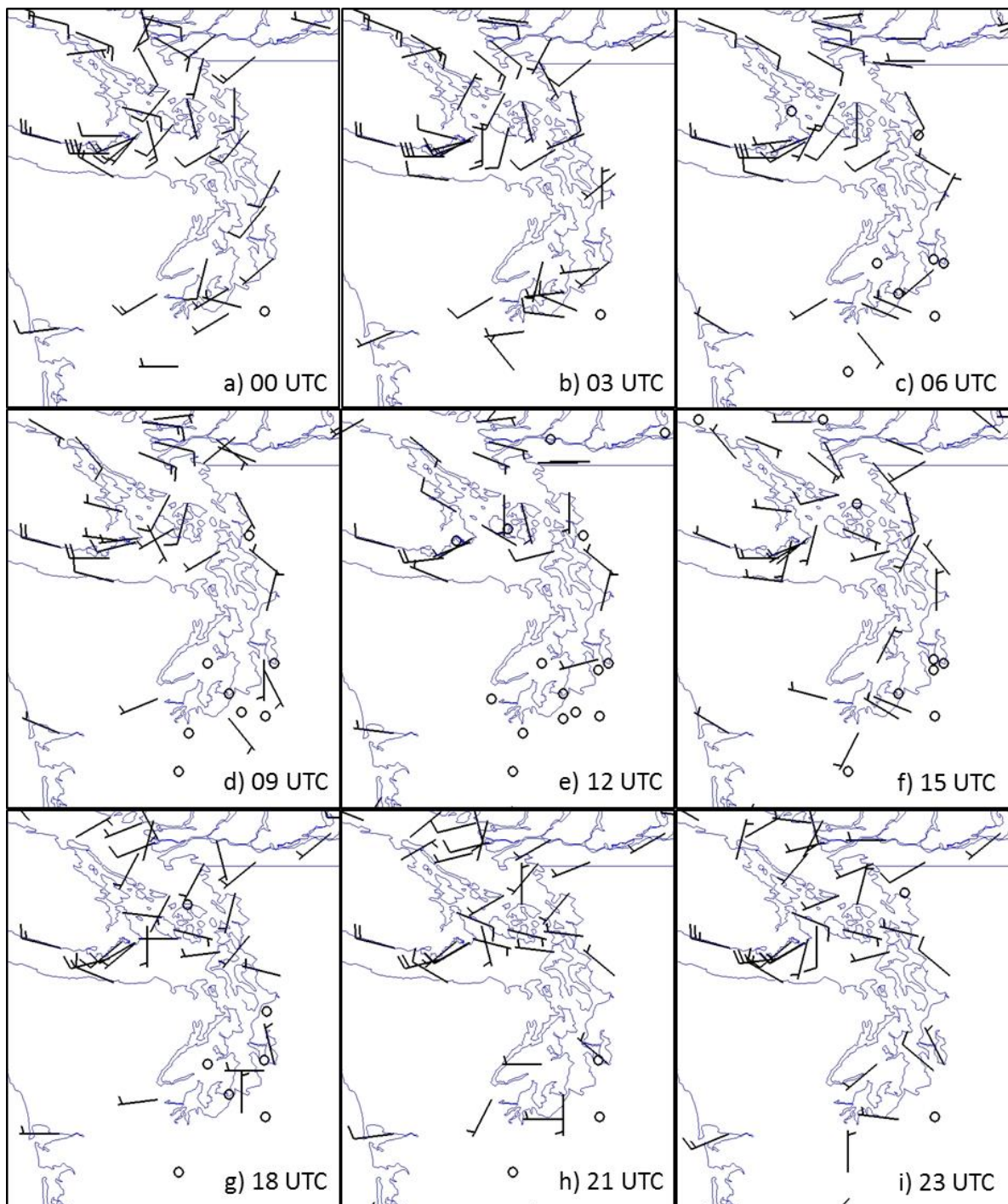


Figure 12 Observed surface wind plots from 18 July 2013 from 00 (a) to 23 UTC (i) (Data courtesy Iowa State University, <http://mtarchive.geol.iastate.edu/> 2015).

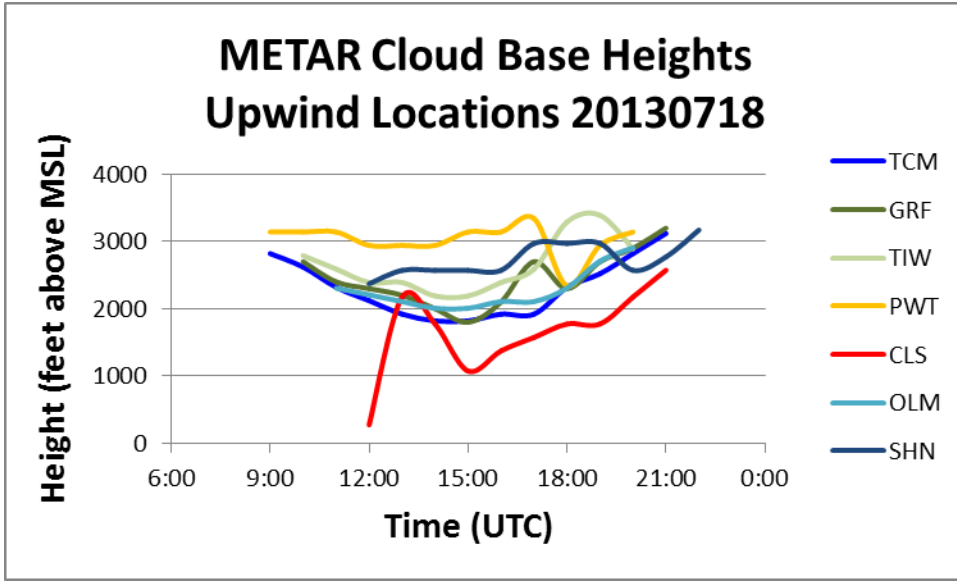


Figure 13 Time series of METAR cloud base heights at locations upwind of Seattle-Tacoma during the 18 July 2013 stratus event. Cloud base heights are observed to rise with time after solar heating began.

Without cloud top height or temperature profile observations for those locations, it may be impossible to say whether another dissipation mechanism contributed. A view of observed cloud base height trends for the four locations downwind of the climatological aerosol concentration maximum and closest to the lingering stratus (Fig. 14) reveals a morphological difference in cloud base height trends there compared to the upstream locations.

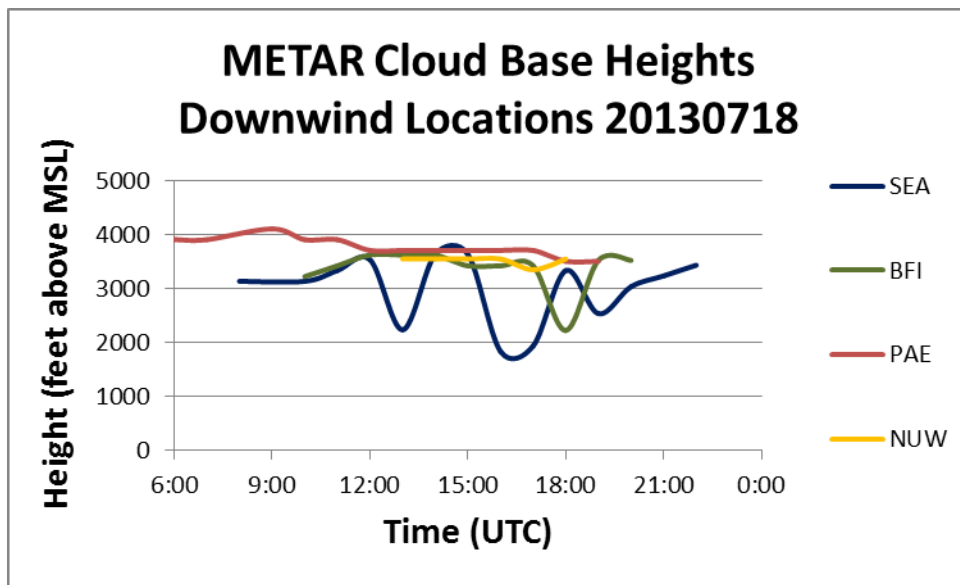


Figure 14 As in Figure 13, except for locations downwind of the climatological aerosol concentration maximum.

Cloud bases are seen to generally trend at the same height (despite scattered low cloud observed at Seattle) or lower over time, as in the cases of Paine Field (PAE) and Whidbey Island Naval Air Station (NUW). The map view in Figure 15 provides geographic context to this finding, showing LCL lifting in southern and western locations, but subsidence in northern and eastern locations.

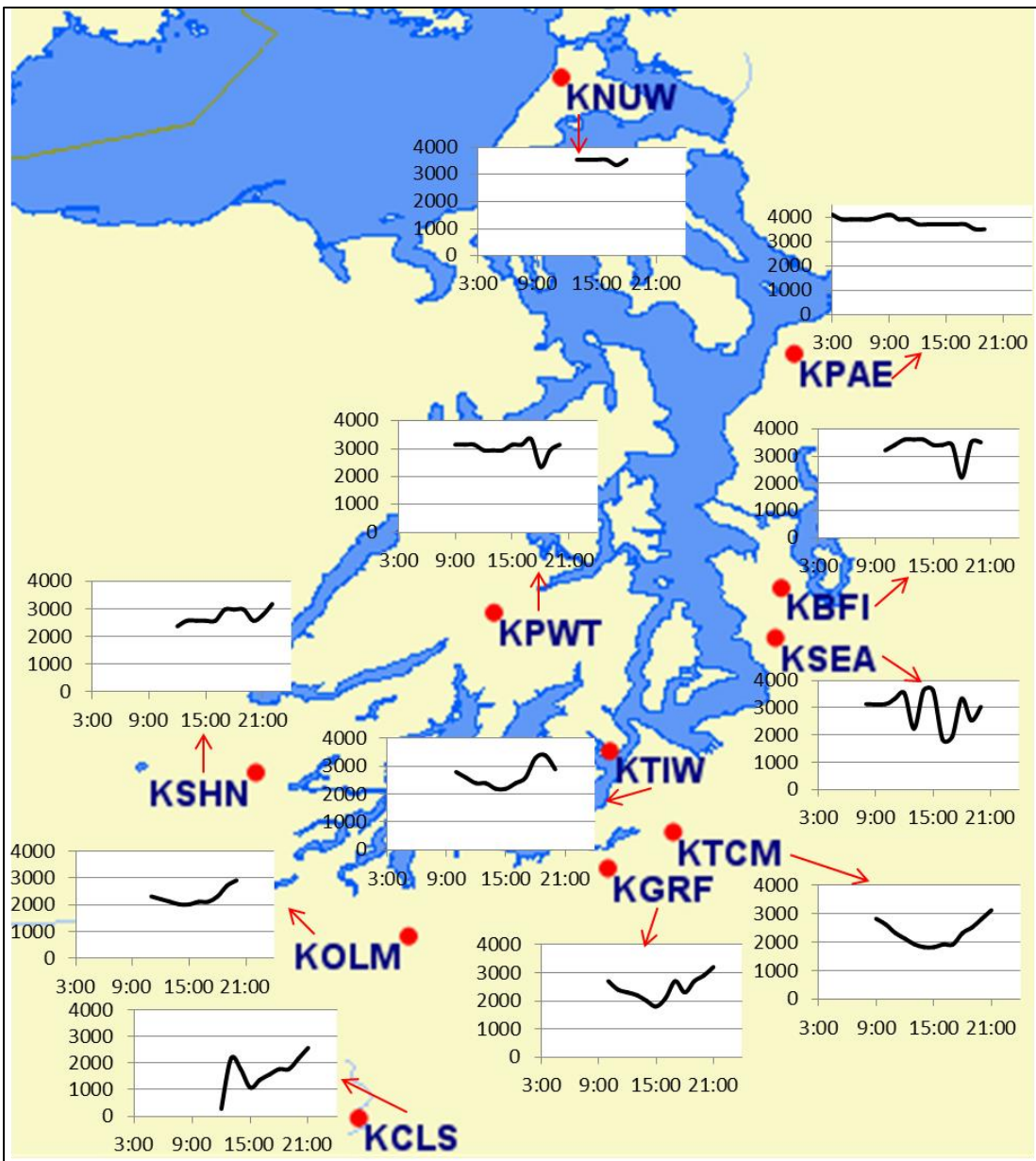


Figure 15 Map of METAR observation stations with insets displaying cloud base height trends from the surface to 4,000 ft (vertical axis) at each location from 03 to 24 UTC 18 July (horizontal axis). General trends show increasing cloud base heights with time before dissipation for all but those locations between the Sound and the Cascades.

A series of TAMDAR observed temperature and dew point profiles taken during ascents and descents at KSEA in the hours leading to dissipation (Fig. 16) indicate 10 to 20

hPa variability inversion height and increasing surface dew point depression (lifting LCL) with time.

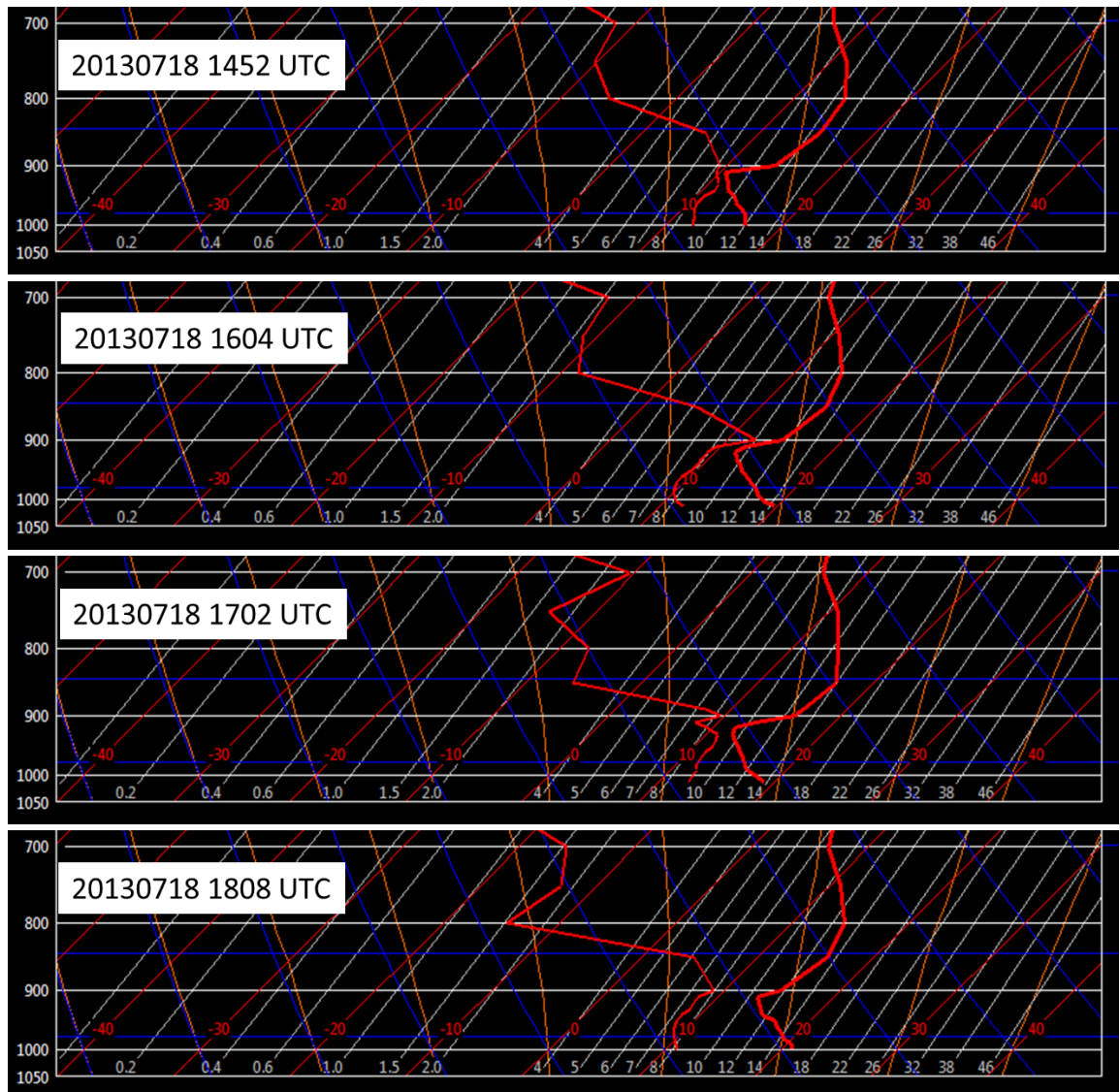


Figure 16 TAMDAR soundings at KSEA on 18 July 2013 at 1452, 1604, 1702, and 1808 UTC, as indicated.

This information viewed in aggregate is evidence that the dynamic or physical properties and processes responsible for stratus dissipation over the eastern Basin may have been different than for the rest of the basin, not just simply that the same mechanisms acted more slowly there. Instead, TAMDAR sounding at 1604 and 1702 UTC show evidence of inversion lowering simultaneous to surface warming, which would increase the rate at which the LCL approached the cloud base, and the pace with which the stratus eroded over KSEA, and perhaps other locations in the eastern PSB. Additionally, disparity in cloud cover between METAR and TAMDAR is likely due to METAR algorithms representing the celestial dome and TAMDAR representing a single point in time and space along a flight route, as discussed in Chapter 2.

The presence of the stratus against the Cascades after erosion elsewhere (Fig. 11) does not seem coincidental. Figure 17 shows the METAR observed wind direction and speed at KSEA on 18 July 2013. Southerly winds were observed at KSEA during stratus formation around 08 UTC. Winds became variable to calm from 10 to 16 UTC as the stratus loomed overhead. Sunrise (1231 UTC) began warming the region, and winds became westerly and remained westerly until stratus dissipation at 2049 UTC.

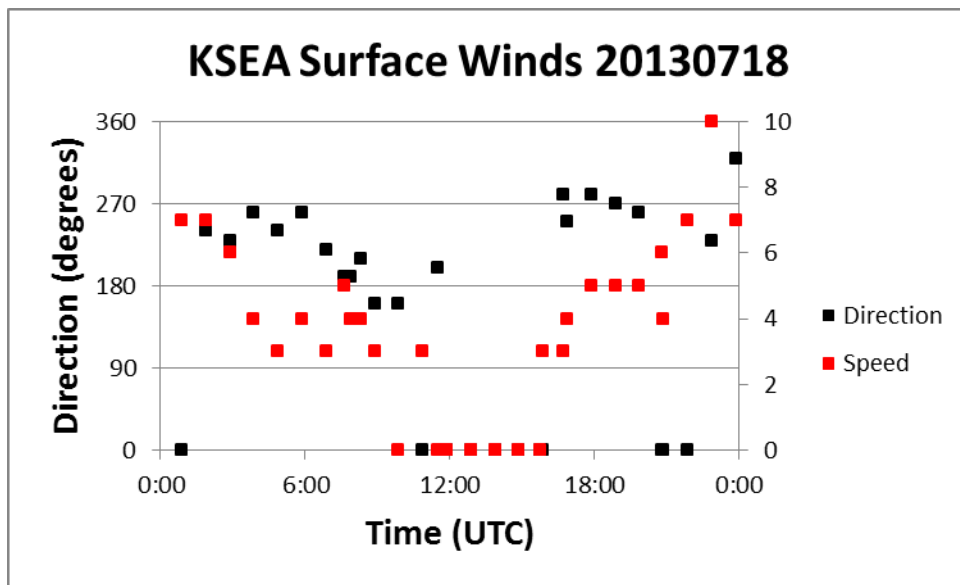


Figure 17 Time series scatter plot of surface wind direction (black, left vertical axis in degrees magnetic) and speed (red, right vertical axis in knots) observed at Seattle-Tacoma International Airport (KSEA) on 18 July 2013 (data courtesy 14WS).

Figure 18 shows model aerosols transported east against the Cascades at 12 and 18 UTC. This may have produced the cloud lifetime effect due to the nucleation and growth of droplets on numerous aerosols carried from the polluted Seattle-Tacoma metropolis.

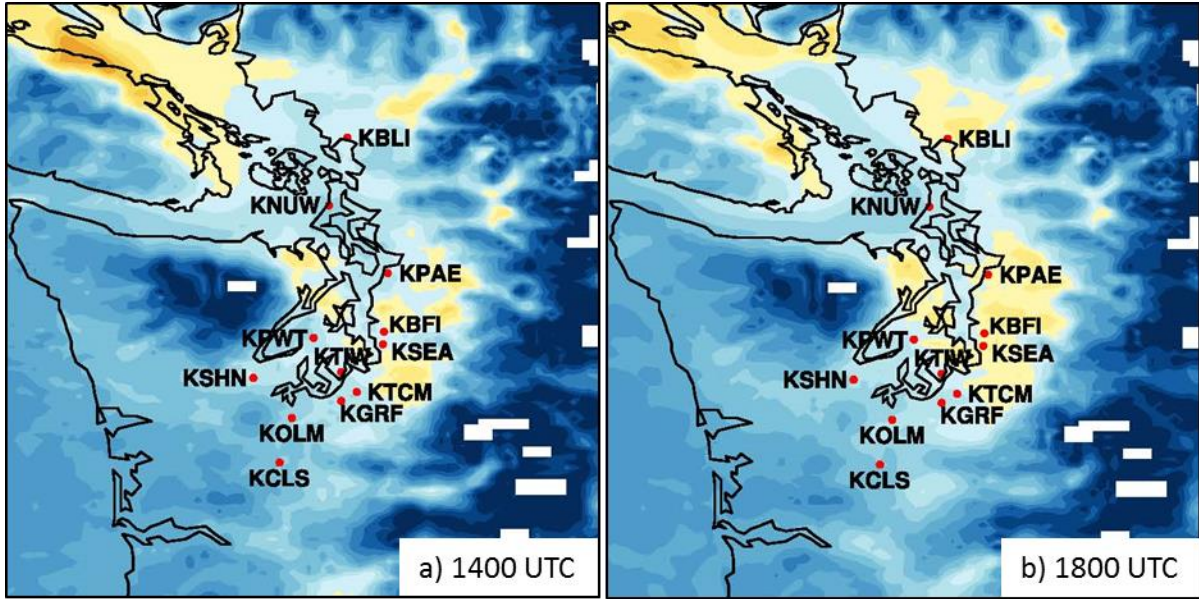


Figure 18 As in Figure 8 but at 14 (a) and 18 (b) UTC.

3.2 Model Cloud Microphysical Properties

This section seeks to identify general similarities and differences between the observed and theoretical physical and modeled cloud and to test the primary hypothesis that allowing model cloud droplet number concentration to vary could result in more representative forecasts for cloud properties such as cloud lifetime and radiation transmissivity. Initial examination compares clouds produced by the 100, Aero, and 1000 runs to determine whether the changes to droplet number concentration prescription (1000 run) or explicit accounting for aerosol-cloud interaction (Aero run) produced expected changes in model cloud.

3.2.1 Model Cloud and Shortwave Radiation

Model cloud forecasts are examined with respect to shortwave radiation transmissivity. If no difference is observed between model cloud properties produced by

default settings and those generated by a tenfold increase in N_d prescription (1000 run), then either the configuration used here is incorrect or investment of time and money in aerosol observation assimilation into model initial conditions may be avoided until more influential model weaknesses are addressed and computational capability improves. However, if there is a difference between how a model cloud with domain-wide droplet concentrations equal to those of the near-surface values observed only near major urban pollution centers, then further testing and investment may be worthwhile.

A basic test of the model changes is whether the forecast Skew-T for the 1000 run is cooler and LCL lower than that of the 100 run during stratus dissipation time. Examination of the overlaid profile samples in Figure 19 indicates that at the 17 UTC (a) and 18 UTC (b) stratus burn-off times, the 100 (blue) temperature and dew point depression are greater than for the 1000 (red). By definition, the 1000 run LCL is also lower. The time series of Seattle temperatures in Figure 20 indicates that for nearly all times, the 1000 run indicated the lowest surface temperature. Even the 00 to 06 UTC timeframe shows the 1000 as the lowest temperature, while the PSB was cloud-free. Instead of showing a cool bias, this temperature anomaly is likely due to similar lack of heating through lower transmissivity cloud of the 1000 persisting the previous afternoon.

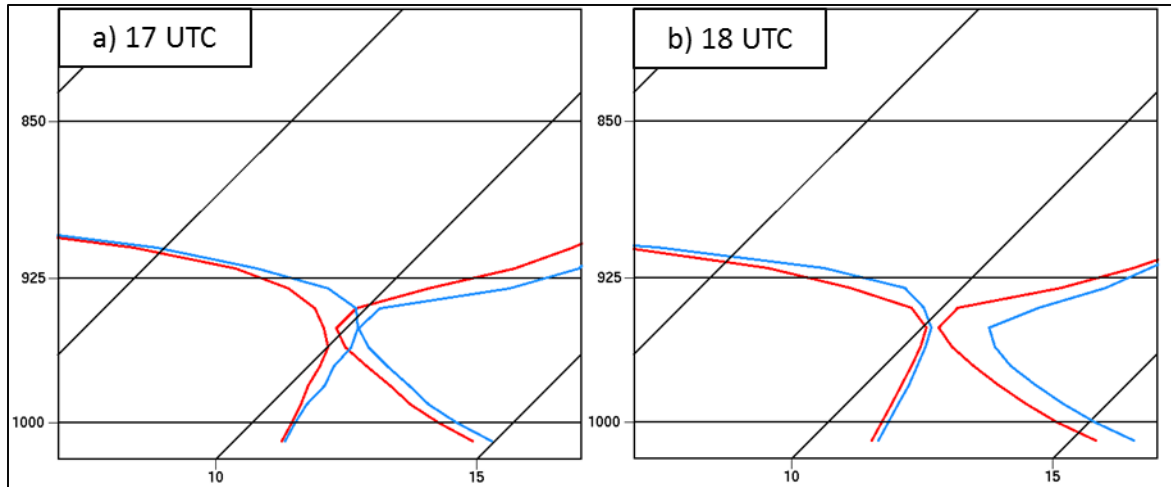


Figure 19 Overlaid Skew-T log P diagrams for the 100 (blue) and 1000 (red) runs valid for 18 July 2013 at 17 (a) and 18 (b) UTC indicating that the 1000 run is cooler at the surface, and has a lower lifted condensation level than the 100 at each time.

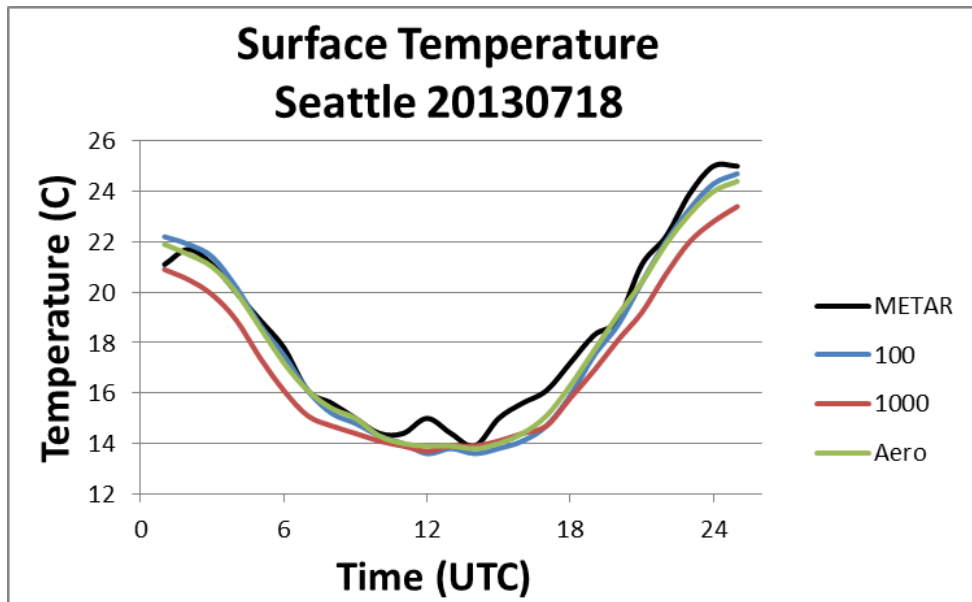


Figure 20 Time series of METAR observed surface temperature (black) with 2-meter forecast temperatures from the 100 (blue), 1000 (burnt orange), and Aero (green) runs valid for Seattle on 18 July 2013.

Cloud transmissivity to incoming sunlight is most easily measured in the present model setup by downwelling shortwave radiation (W m^{-2}) reaching the ground. Difference

fields for this variable (Fig. 21) between the 1000 (a and c) the 100 control run and the Aero (b and d) show that there is significant difference in direct solar shortwave radiation penetrating clouds of different models at 1400 (a and b) and 1800 UTC (c and d). Some of these values are certainly due to location differences between clouds forecast by each model. However, the raw fields were heavily smoothed before differencing in order to mitigate this effect, as discussed in Chapter 2. Shortly after sunrise, some differences in coverage exist between the 1000 and the 100 runs (a), but the solid negative values (green through white color shading) indicate that clouds in the 1000 run were more opaque to solar radiation than the control run.

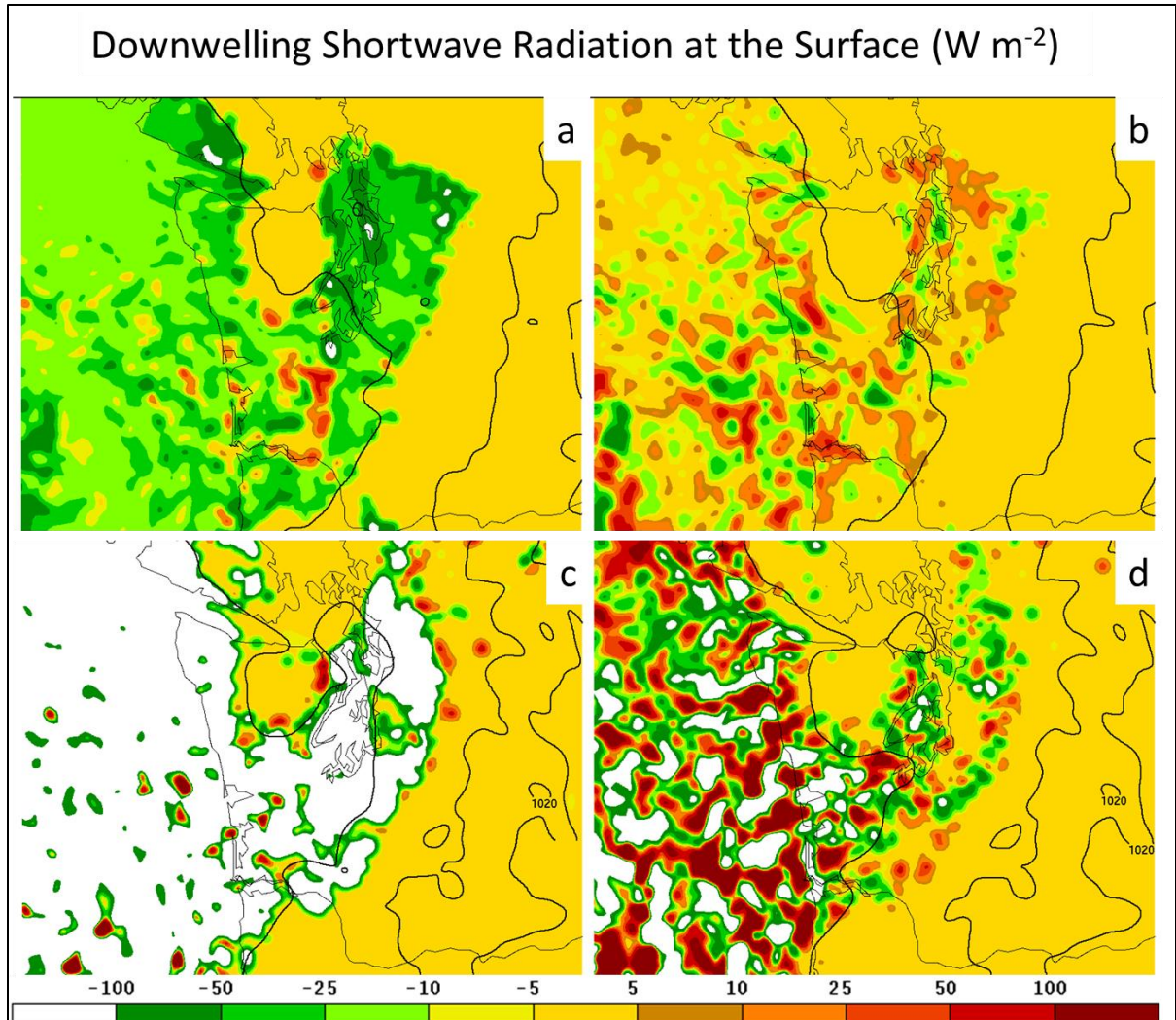


Figure 21 Difference fields in downwelling shortwave radiation at the surface (W m^{-2}) at 1400 (a, b) and 1800 UTC (c, d) between the 1000 run (a, c) and the Aero run (b, d) and the control, respectively.

The Aero run (Fig. 21b) shows approximately equal area of negative as positive values, indicating that most of the variation in downwelling shortwave radiation between that and the control is due to cloud location differences for that forecast time. However, at 1800 UTC (Fig. 21d) the Aero run was more opaque to shortwave radiation than the control between the eastern Sound and the western slopes of the Cascades. The 1800 UTC

differences between the 1000 and 100 (Fig. 21c) show that a tenfold increase in cloud droplet number concentration has a significant influence on model cloud shortwave transmissivity at this time, on this case day.

However, what is not shown in these images is whether the true reason for the noted differences is due solely to a higher number of smaller droplets creating a larger total reflective and refractive cross-sectional surface area, as Twomey (1974) showed, or that smaller drops delayed precipitation as Albrecht (1989) showed, or that the increased cloud density to shortwave radiation acted as a thermodynamic positive longevity feedback loop as Ackerman (1995) showed. Figure 22 shows total column cloud water differences for the Aero (a) and 1000 (c) compared to the control at 1400 UTC on 18 July 2013. Differences between Aero and control are clear over the central and eastern PSB (a) where the Aero produced a greater amount, not simply a different location of cloud water than the 100 control run. Comparison with the downwelling shortwave radiation difference (Fig. 21b) between runs shows close correlation between areas of higher Aero cloud water amount and greater differences in opacity. Similarly, the cloud water produced by the 1000 run columns exceeds that produced by the 100 run (Fig. 22b) which is reflected almost perfectly by Figure 21a.

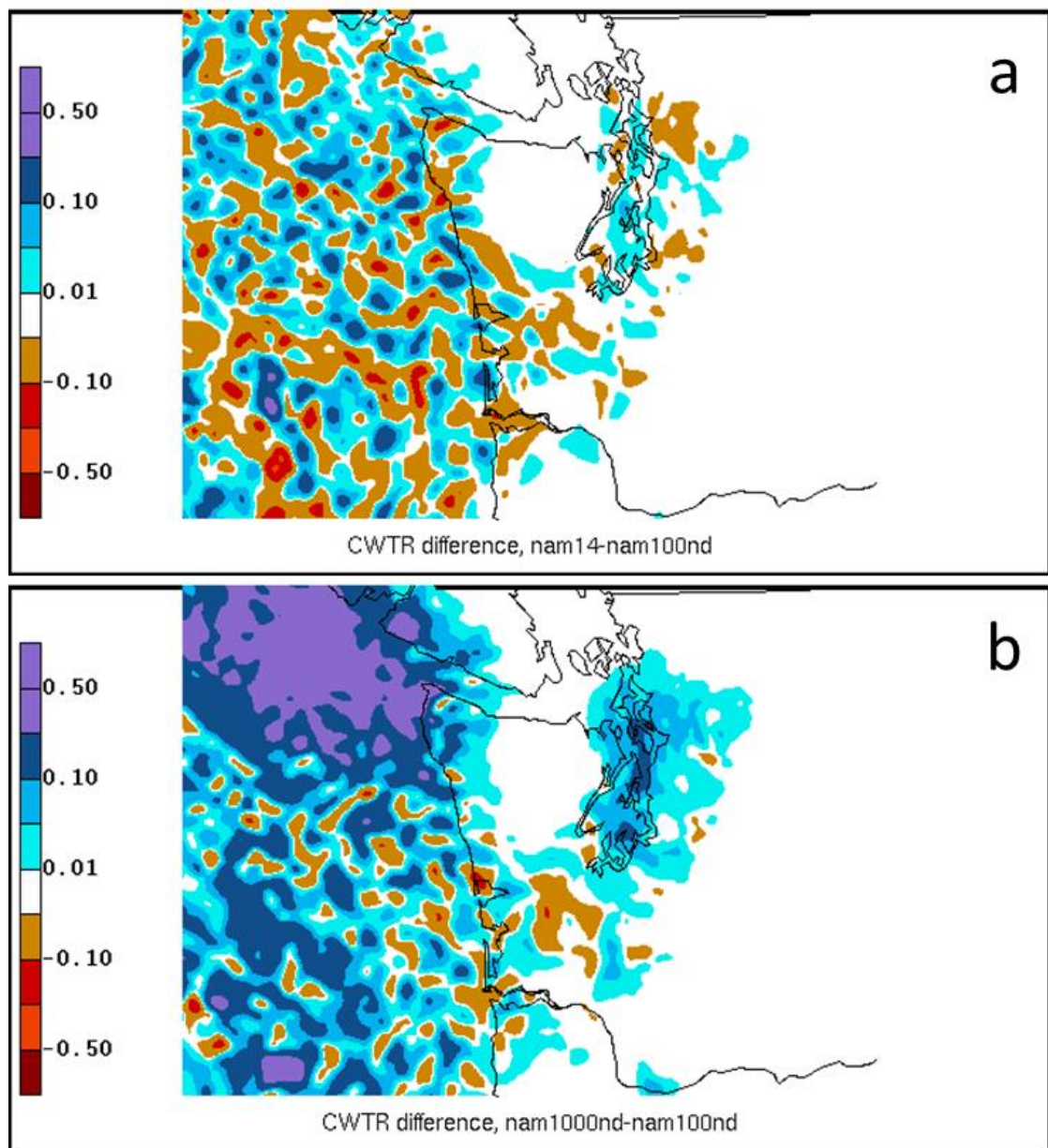


Figure 22 Difference fields of total column cloud water (kg kg^{-1}) between the Aero (a) and 1000 (b) and the control 100 run, respectively, valid 18 July 2013 at 1400 UTC.

The apparent causal relationship between total column cloud water content and shortwave radiation deficiency at the ground muddies the waters of attribution pertaining to

what macro or microphysical process is responsible for the increased shading in the 1000 and Aero runs. It is a foregone conclusion that more water would lead to less surface incident shortwave radiation. Therefore, a more direct test is required.

The most direct test of model cloud difference relevant to this study is to measure cloud radiation transmissivity relative to the amount of cloud water present in any given cell. If the ratio of incident shortwave radiation passing through a cell per given amount of cloud water is less for the Aero or 1000 than for the control, the test model configurations under study here are exerting the expected influence on cloud optical properties. Figure 23 shows this ratio, gathered from the area enclosed by the box indicated on the accompanying plot of water friendly aerosol valid at the same time. These values were measured through the each vertical model column every 15 minutes for the two hours centered on solar noon. (When the sun is at its zenith, it is less likely that variability in radiation from changing sun angle will contaminate results.)

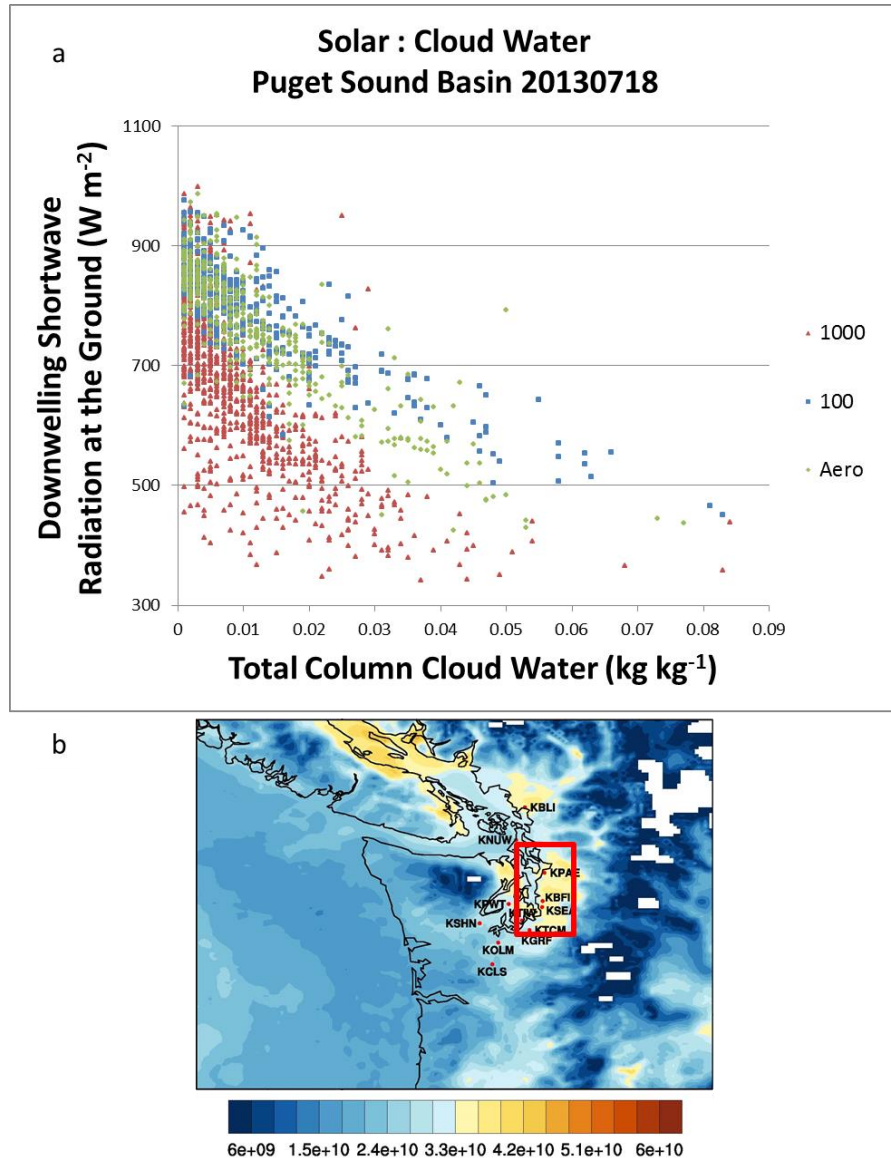


Figure 23 Scatter plot (a) indicating the ratio of downwelling shortwave radiation per unit cloud water from 19 to 21 UTC for the 100 control run (blue), Aero (green), and 1000 (burnt orange) runs, respectively. Map (b) indicating the area for which radiation to cloud water ratios (a) were gathered, overlaid on column-total water-friendly aerosol concentration (kg kg^{-1}) at 2015 UTC. Data was calculated at every vertical grid column of the area shown in the map (b) during the two hour period centered on solar noon 18 July 2013.

The distribution of the shortwave to cloud water ratio for the Aero run is visually different than that of the control run. Statistical examination of these data revealed that the

data are not normally distributed and that a linear fit to the data is not the most accurate fit available. Figures 24 and 25 show the relative difference between a linear fit and the fit when a square root transformation is performed on the cloud water values, which are quite small (on the order of 10^{-2} kg kg $^{-1}$) in comparison to the radiation values (on the order of 10^3 W m $^{-2}$).

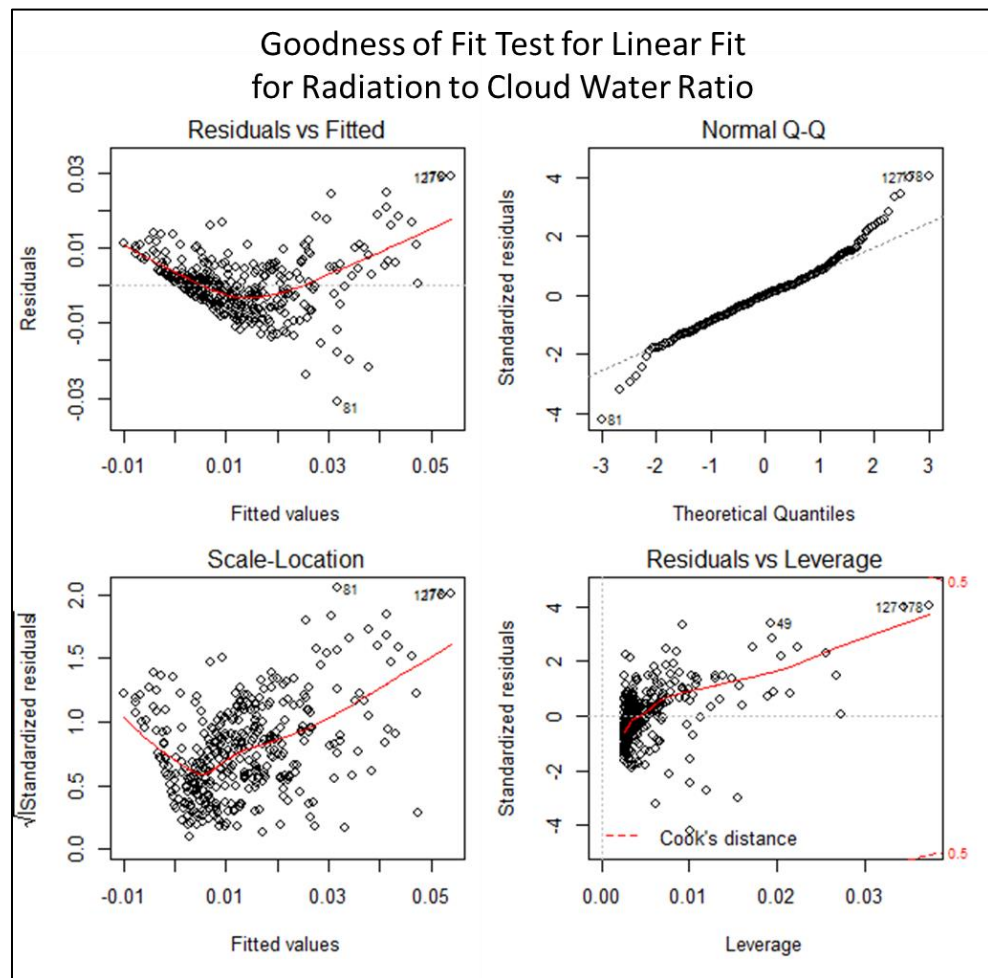


Figure 24 Goodness of fit of a linear regression fitted to radiation per cloud water data presented in Figure 23. Note the poor conformance of the data to the quantile-quantile plot (top right panel). Data were analyzed using R Studio analysis scripts (Constructed with assistance by Suchit Mehrotra).

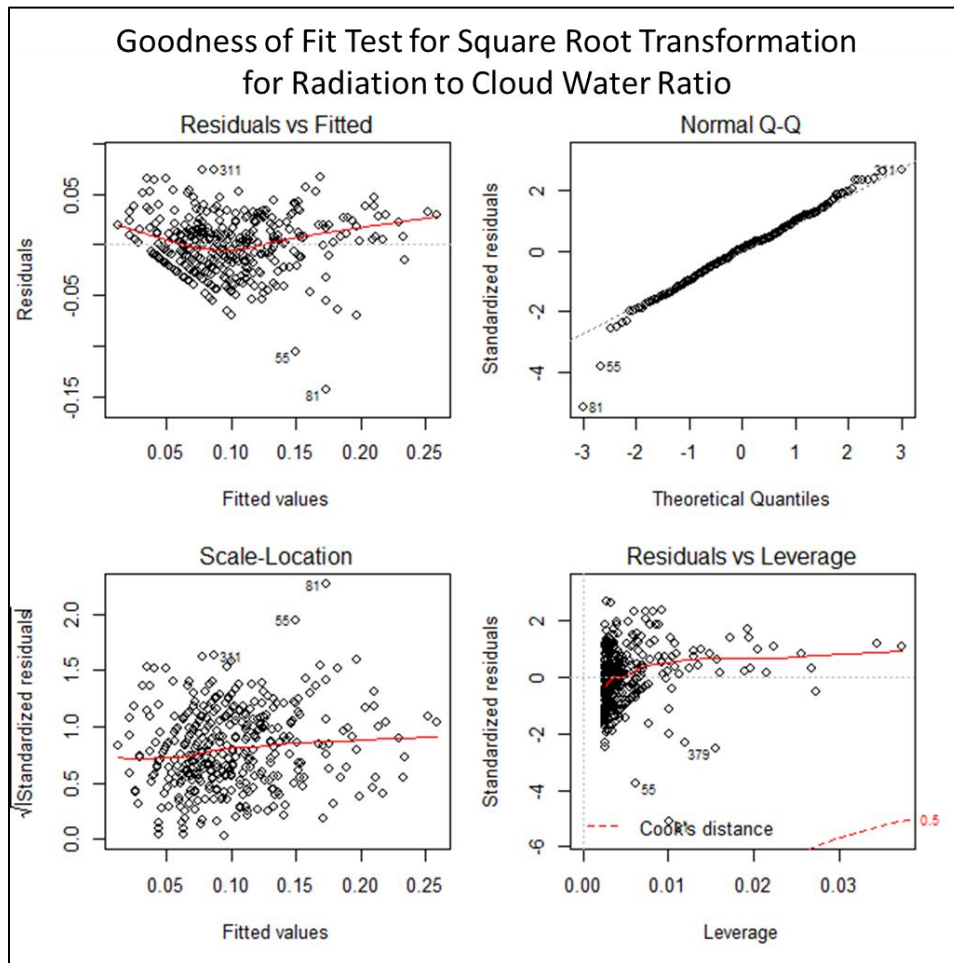


Figure 25 As in Figure 24, except for a square root transformation of the data. Note the improved fit of the data in the quantile-quantile plot (top right panel) (Constructed with assistance by Suchit Mehrotra).

Confidence intervals (CI) calculated for the square root transformed cloud water indicate that at a 95% confidence level, the interval containing the 100 run sample mean slope (CI of -1,611.9, -1,417.5) contains neither the Aero run sample mean (CI of -1,916.4, -1,703.0) nor that for the 1000 run (CI of -2,345.9, 2,067.0). This means we can reject the null hypothesis for equal means. This finding shows that there is a statistically significant

difference between the magnitude of radiative filtering of cloud produced by the Aero and 1000 runs over that of the 100 run, regardless of how much cloud water is produced in a column of air.

This finding takes on even more significance in light of two additional facts. First, the mean cloud water content and shortwave radiation allowed through the 100 cloud were 12.6 g kg⁻¹ and 789.9 W m⁻², respectively. However the Aero and 1000 runs allowed passage of only 768.2 and 661.5 W m⁻², respectively despite including only 11.8 and 9.9 g kg⁻¹ of cloud water each. These figures indicate a 3% and 16% decrease in cloud transmissivity to shortwave radiation with 6% and 21% less cloud water, respectively. Second, comparing the cloud droplet number concentration of the 1000 run and that of the Aero run makes the Aero run's low transmissivity surprising. Figure 26 shows the vertical profiles of aerosol and cloud droplet concentrations (cm⁻³) forecast by the Aero run over KSEA (a) and a downwind point between KSEA and the Cascades (b) 1200 UTC on 18 July 2013.

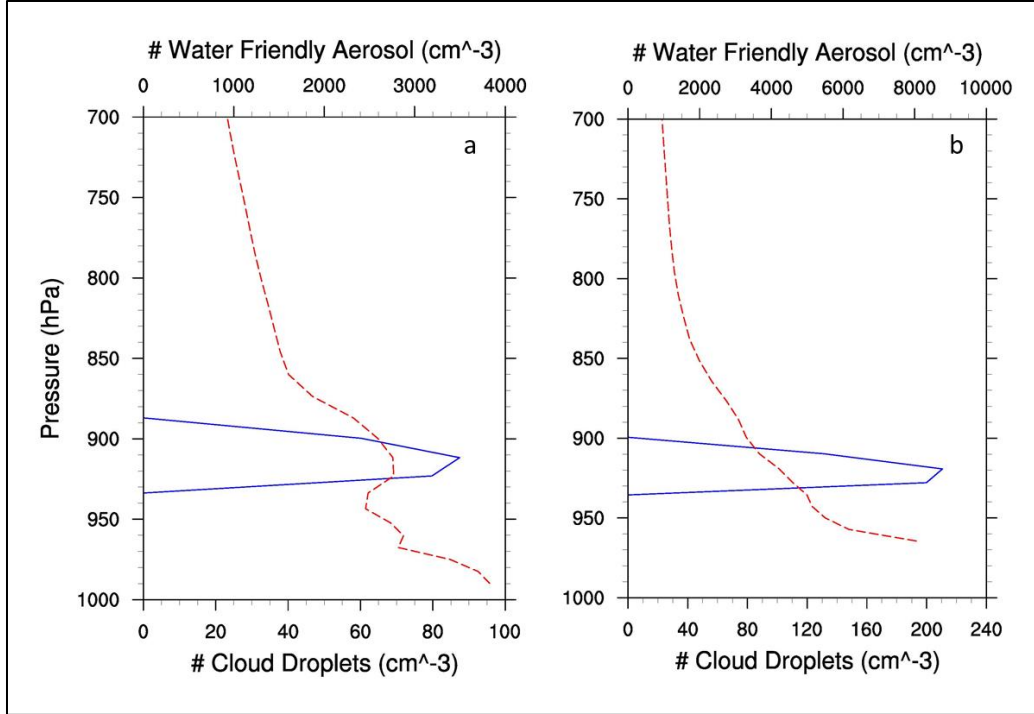


Figure 26 Vertical profiles of Aero run number of water-friendly aerosols (red dashed line) and cloud droplet number concentration (blue solid line) overhead KSEA (a) and approximately 30km northeast of KSEA (b) on 18 July 2013 at 1200 UTC. The vertical axis denotes pressure level heights (hPa), the bottom horizontal axis shows droplet concentrations ($\# \text{ cm}^{-3}$), and the top horizontal axis shows aerosol concentrations ($\# \text{ cm}^{-3}$).

This figure shows that the aerosol content of the model column was physically reasonable. More importantly, the fact that the Aero-produced cloud contained a maximum of 90 cm^{-3} droplets (at this point and time) over KSEA and 220 cm^{-3} at a downwind, perhaps air-dammed location makes achieving a statistically different mean than the control that much more remarkable. After all, the 1000 run had factors of 5 to 10 more droplets per unit volume with which to accomplish its feat.

These results motivate a closer look at other measurable differences between the clouds produced by each model forecast. This effort aims to extract benefits or detriments resulting from this change, as well as attribute cause for the Aero's surprising performance.

3.3 Model Forecast Verification and Intercomparison

In this section, each model operational forecast element under inspection is compared to relevant observations. General horizontal morphology of model cloud is compared to visible satellite imagery. Specific point forecasts of cloud cover and cloud base height at 11 points of ground observation will be compared to sky cover and height as reported by hourly METARs. Model cloud top height is evaluated against irregular TAMDAR observations at KSEA and model cloud geometric thickness is compared both to the TAMDAR-derived value and a value obtained combining TAMDAR and hourly METAR values at that location. Stratus onset and dissipation times are compared with those observed in METARs, including SPECIs as discussed in Chapter 2.

3.3.1 Model Cloud Morphology

The GOES15 visible satellite image from 1345 UTC (Fig. 27) shows stratus veiling the PSB, many Cascade valleys, and well north into Canada. The 100 model forecast three-dimensional isosurface of $5 \times 10^{-5} \text{ kg kg}^{-1}$ cloud water mixing ratio, overlaid in blue on the satellite image, qualitatively shows that the model under forecast ST cover in and around the PSB by a wide margin, particularly in the northern Sound and BC, including several unrepresentative holes.

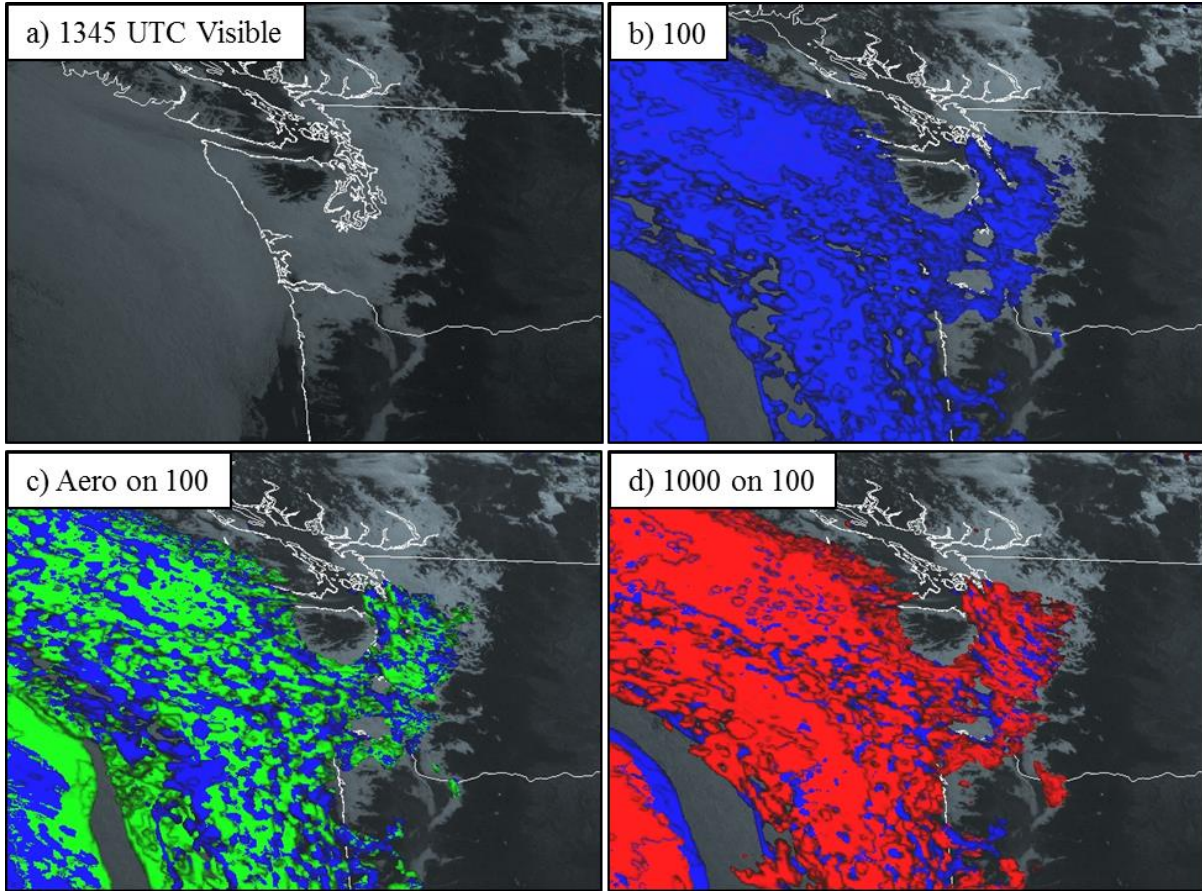


Figure 27 July 18, 2013, 1345 UTC GOES15 visible satellite imagery with the Unidata IDV visible/fog enhancement applied and overlaid with the $5 \times 10^{-5} \text{ kg kg}^{-1}$ 100 (blue) model cloud water mixing ratio as a three-dimensional isosurface. The Aero (green), and 1000 (red) are overlaid onto the 100 image for ease of comparison.

The 100 run produced a ST field which struggled to follow the overall pattern and placement of the observed cloud, predicting far less horizontal extent and uniformity. The three-dimensional overlay of the Aero run (green) onto the control run in Figure 27c shows no drastic differences between the two, the Aero run qualitatively produced wider horizontal and vertical extent of cloud water, as well as filled some of the gaps left by the 100. A slightly improved representation of the open ocean SC and ST placement is evident. Whether

differences between Aero and 100 cloud droplet number concentrations (if any) accounted for the resulting change in coverage is the subject of following paragraphs. However, three-dimensional overlay of the 1000 run onto to the 100 in Figure 27d provides a first indication that qualitatively, the cloud number concentration made some difference at this time, for this case. The morphology of the 1000 cloud is overall the same as the other two runs, but the vertical extent and horizontal coverage are clearly greater than that of the 100 cloud over the PSB at this time. Compared to the Aero overlay, the 1000 produces more cloud water in the vertical, but its horizontal extent is not significantly greater than the Aero. The satellite image and model clouds are all valid for 1345 UTC, only one hour after sunrise. This is reasonably within the time frame at which the ST fields of both the physical and model worlds should be at their greatest horizontal coverage before solar radiation begins its work on them. Yet, the model horizontal coverage noted here is underwhelming in all three configurations. Model cloud isosurfaces plotted with an order of magnitude lower cloud water threshold show no perceptible change in horizontal coverage (not shown).

At 1745 UTC (Fig. 28a), five hours after sunrise, the visible satellite imagery shows that the erosion process was well underway, but there was incomparably more physical cloud remaining in the PSB than 100 model predicted. In fact, Figure 28b shows that by this time the 100 ST deck had already eroded over many of the ground observation stations in the Sound. Close visual inspection of the satellite imagery alone reveals that the physical cloud in the PSB with the most albedo is located between the southeastern shores of the Sound and the Cascades (Figure 28a). Interestingly, the 100 cloud has eroded there by 1745 UTC.

Cloud predicted over the Sound by the Aero run visually appears to have slightly outlasted that produced by the default settings of the 100 run. The fact that the green isosurface of the Aero run is visible above the blue of the 100 run indicates that Aero-produced cloud extended to greater vertical height. Whether that greater height resulted in greater geometric thickness is the subject of later discussion.

The 1000 run clearly predicted more cloud water in the eastern PSB than either of the other runs. Additionally, skies over the northern reaches of the Willamette River valley along the OR border contained physical cloud which neither the 100 nor the Aero predicted, but the 1000 produced. The most distinguishing attribute of the 1000 cloud at this time is the cloud height and coverage produced over the Pacific. To the credit of the 1000 run, most of the open-ocean cloud on the satellite image is obscured by red.

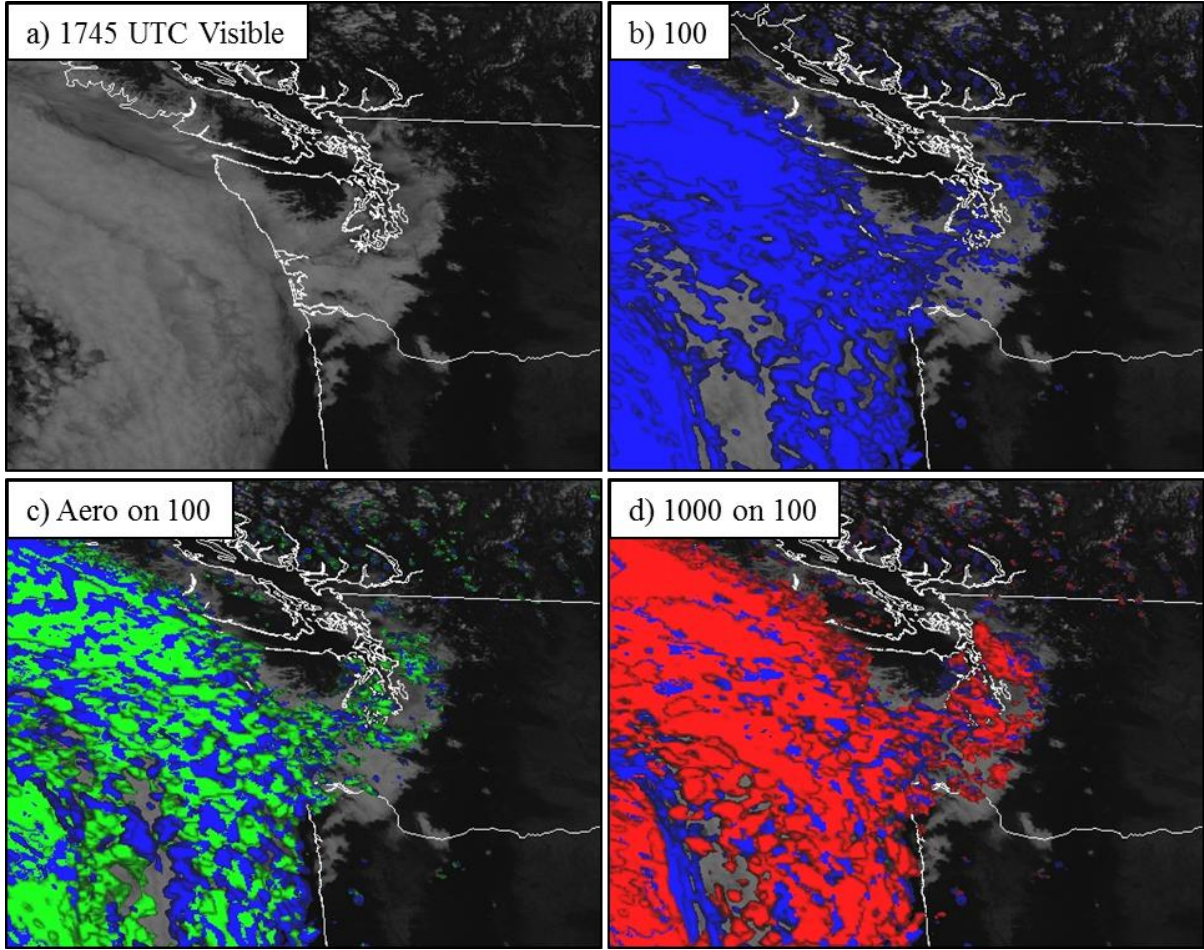


Figure 28 As with Figure 27, but valid 1745 UTC and without enhancement to the visible satellite image.

By 2015 UTC, cloud produced by all three model setups had completely eroded out of the PSB (Fig. 29). Clearly, none of the model configurations examined here accurately predicted the coverage of stratus over the PSB on July 18, 2013, though they only underpredicted duration in most areas by 1 to 2 hours (Fig. 29b through d). It is perhaps noteworthy that the Aero maintained a slight qualitative margin over the 100 prediction of cloud top height over the ocean, and that the 1000 run dominated both others in horizontal and vertical extent. The 2015 UTC visible image once again indicates that the most persistent

stratus around the PSB was that southeast of what is the area's highest mean pollution concentration. As mentioned in the overview, this was the last cloud in the PSB and it persisted until 2245 UTC (Fig. 30).

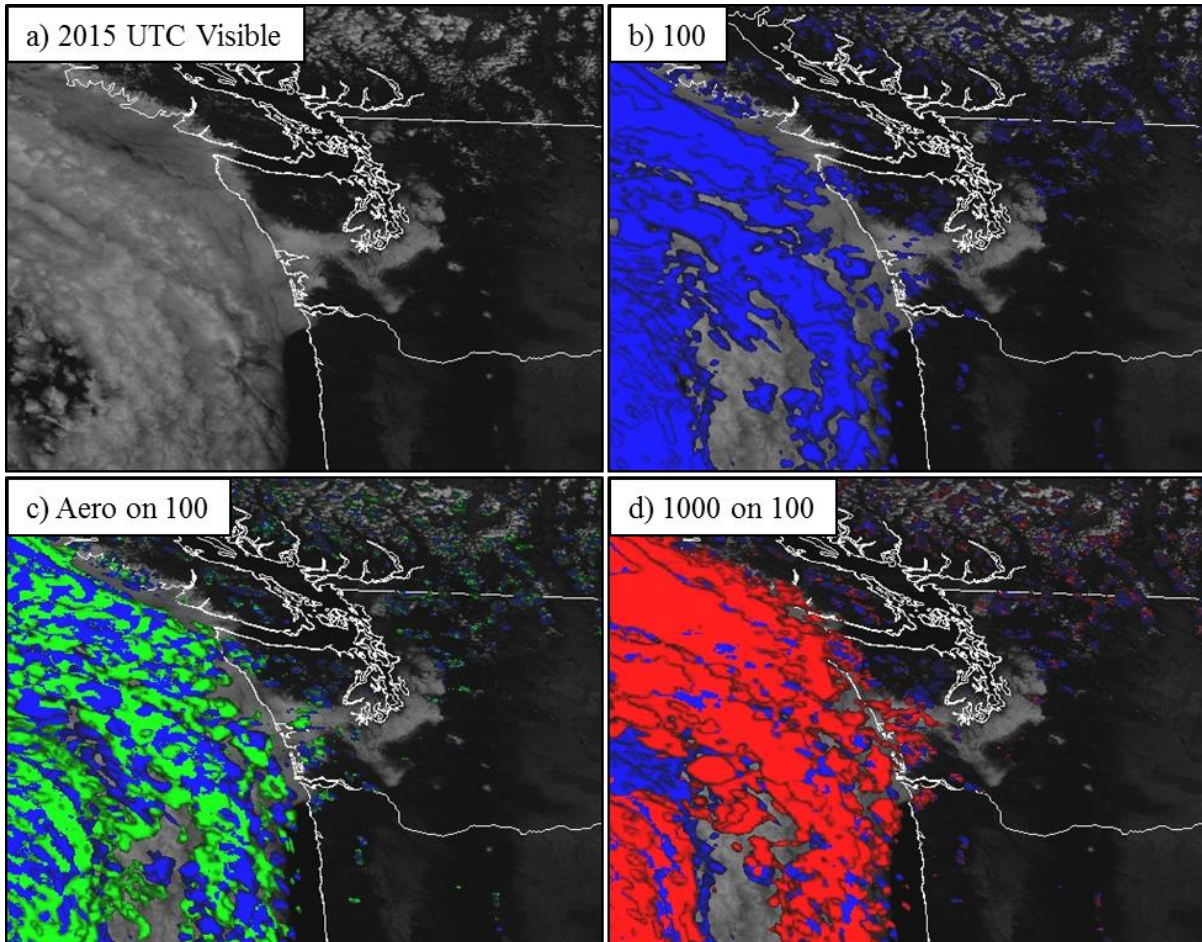


Figure 29 As with Figure 28, but valid 2015 UTC.

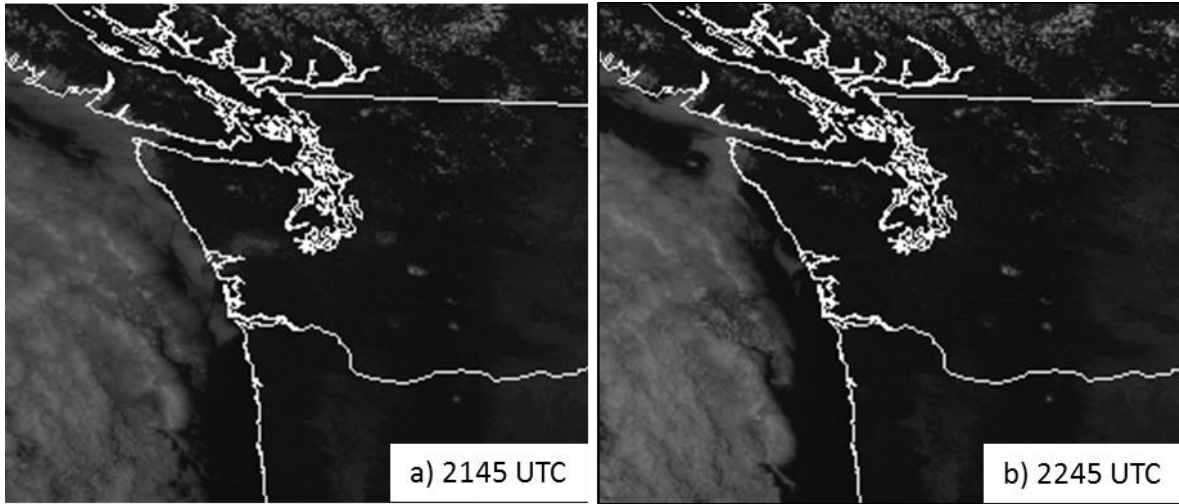
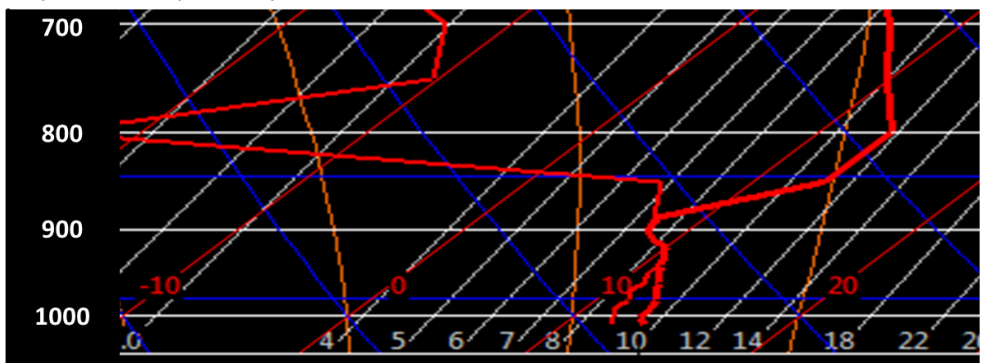


Figure 30 GOES15 visible satellite images valid 2145 (a) and 2245 UTC (b) showing complete stratus dissipation in the PSB.

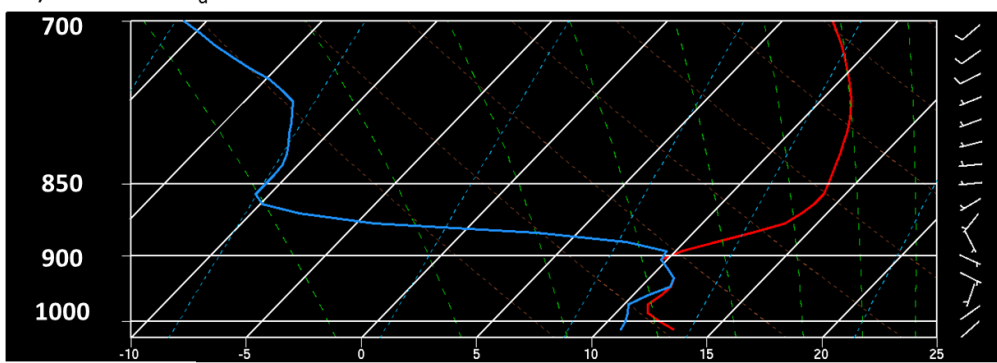
In quantifying forecast error, the best possible verification observation is in-situ data. Figure 31 compares an ambient temperature and dew point profile observed by an aircraft using TAMDAR in an ascent from KSEA at 1409 UTC on 18 July 2013 (A) with those of the 100 (B), Aero (C), and 1000 (D) forecasts valid for 1400 UTC. Because the TAMDAR sounding presented was taken during an ascending trajectory, the dew point indicated near the 850 hPa level is likely an artifact of sensor wetting, as discussed in Chapter 2. Despite the slight differences between the horizontal and vertical scales of the TAMDAR sounding versus the model soundings, comparison can be made of surface temperature and dew point, inversion height, and inversion strength, as well as cloud base and top heights.

Figure 31 Comparison of Skew-T log P diagrams observed by TAMDAR (A) at 1409 UTC, and forecast by the 100 (B), Aero (C), and 1000 (D) runs valid for 1400 UTC on 18 July 2013. Note the horizontal and vertical scale of the TAMDAR sounding differs slightly from those of the forecast soundings.

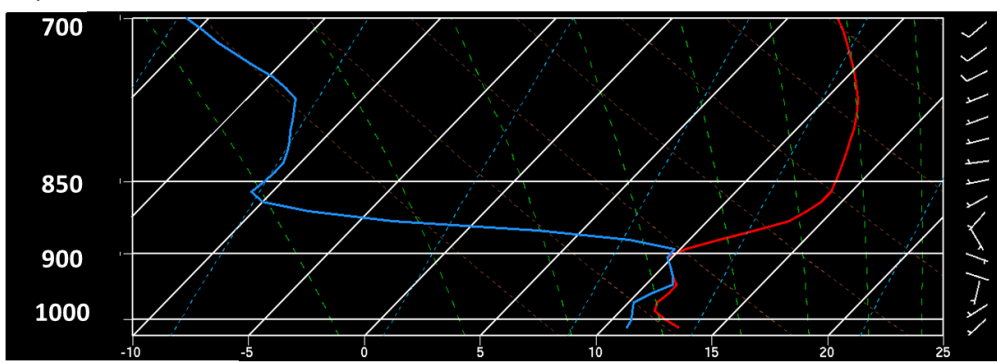
A) TAMDAR (Ascent)



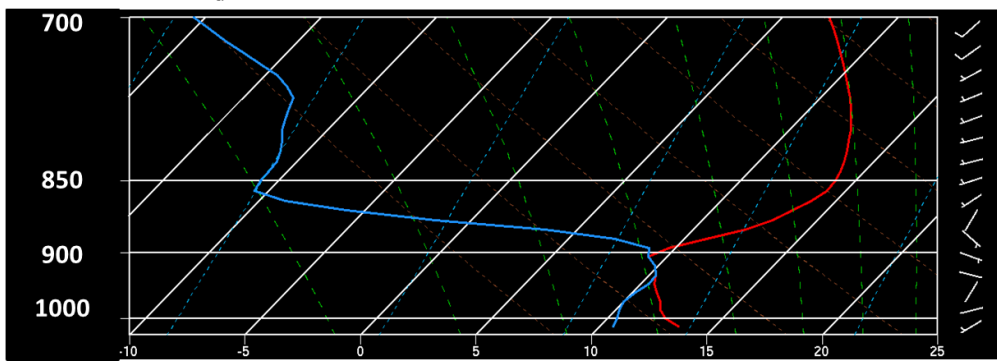
B) NAM 100 N_d



B) NAM Aero



D) NAM 1000 N_d



The first temperature observed by TAMDAR on this ascent was 13.8 C at ground level, followed by an observation of 13.2 C 377 ft AGL. The dew point observed by TAMDAR was 11.8 C (Fig. 31a). The surface METAR report from 1353 UTC indicates a temperature of 15.0 and dew point of 11.1 C (not shown). This indicates the possibility of a moist, cool bias in TAMDAR at the surface. Each model run reproduced TAMDAR and METAR dew point to within a degree, and temperature to within 2 degrees. The stability indicated on the TAMDAR sounding is greater than that shown for all three of the model representations. Each model run's lapse rate from the surface to approximately 975 hPa was too unstable and dew point too low. It appears as though the 100 and Aero model environments allowed too much solar radiation through the cloud, which allowed the ground to warm too quickly and destabilized the lower PBL more than was observed. This result is consistent with the lack of realistic cloud cover discussed in the previous section. The moistening observed in the TAMDAR at and above approximately 950 hPa is represented by the models, but model representations are slightly too warm for both the ambient temperature and dew point at this level. The comparative low level drying shown in the 1000 sounding up to approximately 940 hPa may be the result of a TAMDAR cool, moist bias. However, the 1000 sounding most closely represented the observed profile from 940 hPa to the inversion base. The TAMDAR profile above and below the 900 hPa level indicates the cooling expected by entrainment and evaporation at cloud top, and is best replicated (without shallow mixing) by the 1000. The 100 and Aero runs produced an inversion base temperature of 10 C, while the 1000 predicted approximately 9 C, only 0.4 C higher than the observed value. Several other ascending and descending soundings taken within 15 minutes of 1400 UTC

show cloud top temperatures between 7.2 (1349 UTC, descent) and 11.2 C (1411 UTC, ascent), indicating that the model representations were all within the observed range. It is worth noting that the point forecasts of the three model soundings represent the area overhead of KSEA and therefore are technically unobservable by aircraft on descending glide paths or ascending departures, and that aircraft ascend and descend at different rates, causing different space resolution between their observations, as discussed in Chapter 2.

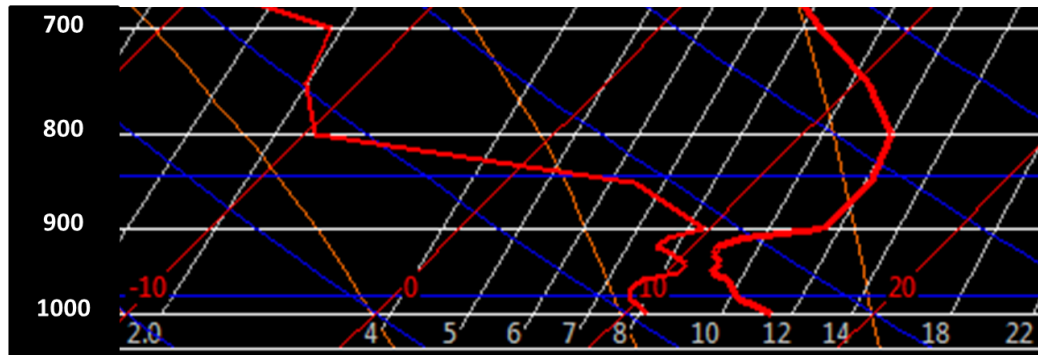
The height at which the inversion top was observed was clearly above 900 hPa. Forecasts show lower values in all three cases by as much as 10-20 hPa. The subsidence inversion in the observed sounding reaches a maximum temperature of 13.3 C, at a pressure level of 800 hPa. Each of the three models forecast this value to within a degree but the three models under predicted this height. Other aircraft within 15 minutes of this time recorded inversion top temperatures and heights that ranged from of 13.8 C at 4,220 ft (1401 UTC ascent to the north) to 13.3 C and 5,300 ft (1418 UTC ascent to the southeast).

At 1800 UTC, model soundings show the bottom-up erosion of stratus as previously discussed compared to a TAMDAR observation from 1808 UTC (Fig. 32). The TAMDAR sounding indicates an inversion base which was once again lower than observations from previous hours, and this particular aircraft descent observed more moisture below the inversion than other soundings from within 15 minutes ascending or descending through different quadrants of the KSEA approach corridors. Regardless of quantitative fluctuations in temperature and dew point by 1 to 2 degrees C, the model forecasts for all three configurations indicated a realistic evolution toward dissipation. The 100 and Aero runs were nearly indistinguishable at KSEA at this time, but both showed dry adiabatic lapse rates up to

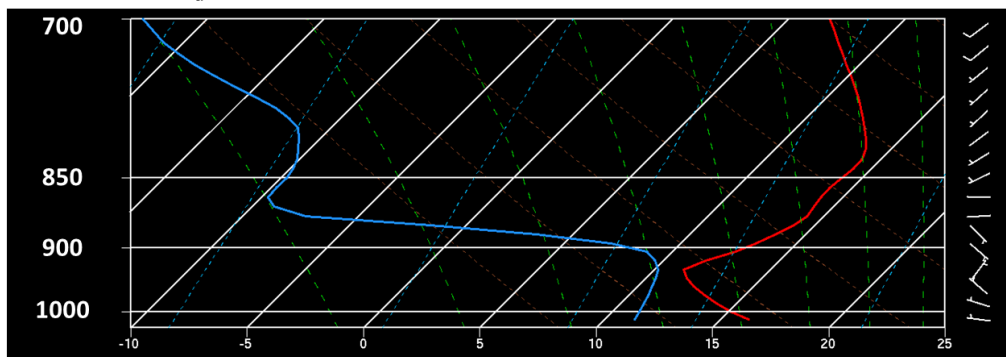
the inversion base, confirming that solar surface warming was a contributing factor to stratus dissipation in those runs. The 1000 run did a much better job representing the moisture observed in the TAMDAR, although the inversion base forecasted is noticeably lower than that observed. As expected, the 1000 forecast a lower surface temperature than the 100, Aero, TAMDAR and METAR (18 C).

Figure 32 Model forecast sounding comparison to TAMDAR as in Figure 31 except valid for 1800 UTC (model runs) and 1808 UTC (TAMDAR).

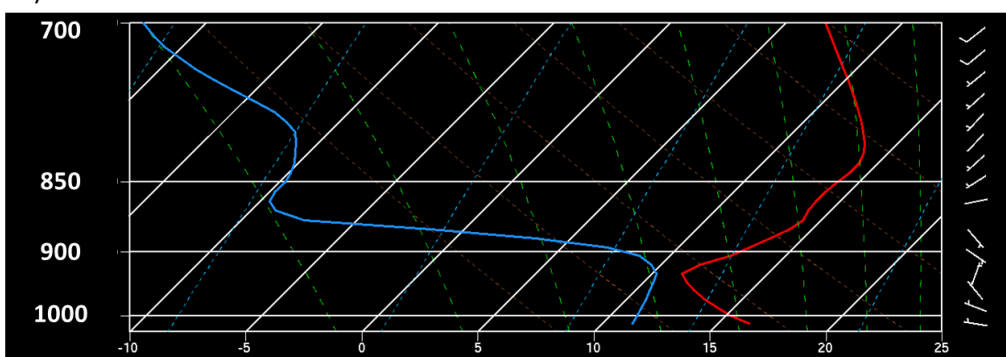
A) TAMDAR (Descent)



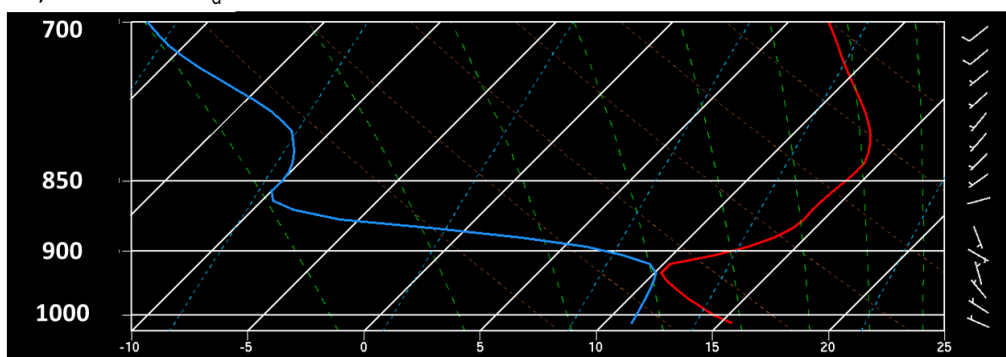
B) NAM 100 N_d



C) NAM Aero



D) NAM 1000 N_d



3.3.2 Point-Forecast Cloud Coverage

Using the grid cell averaging technique described in Chapter 2, model data were evaluated at each of the 11 ground observation locations for average cloud cover. This area-average coverage value was output and collected every 15 minutes for model data but is compared to the hourly observations of sky cover in METARs. Therefore, each location has 24 coverage observations and point forecasts. These are compared graphically and statistically with discussion in the following paragraphs. Given that these data are for just one case day, it is prudent to note that the significance of these results can easily be overstated.

The site-to-site variability in cloud coverage over time is small. Figure 33 shows a time series of the hour-by-hour all-site average of fractional cloud cover for observations and the average of the predicted values of each model run. All three model runs predicted stratus onset and dissipation early. Each run represented the mean cloud cover within 25% until dissipation began in model cloud. Every forecast under-predicted the longevity of higher coverage values at each time after ~1500 UTC. Area averaging of the model and observed cloud cover values at every site mitigates the potential that such a distinct failure could be caused by simple location difference between the forecast cloud and the observed cloud for each location.

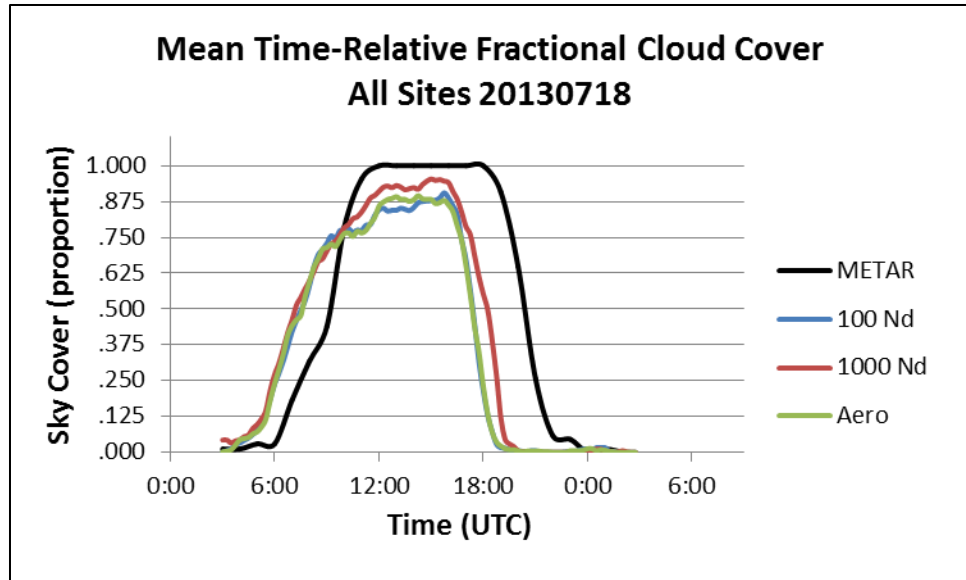


Figure 33 Time series of mean cloud cover proportion averaged across all locations for METAR (black), the 100 (blue), 1000 (burnt orange), and Aero (green) runs.

Differences between runs and locations become readily apparent in examination of Figure 34. The top row in Figure 34 shows the differences between 100 (blue), 1000 (burnt orange), and Aero (green) model runs and observed coverage for all sites averaged over time (a), for each site averaged over all times (b), and displays RMSE of all sites averaged over time (c) and for each site averaged over all times (d).

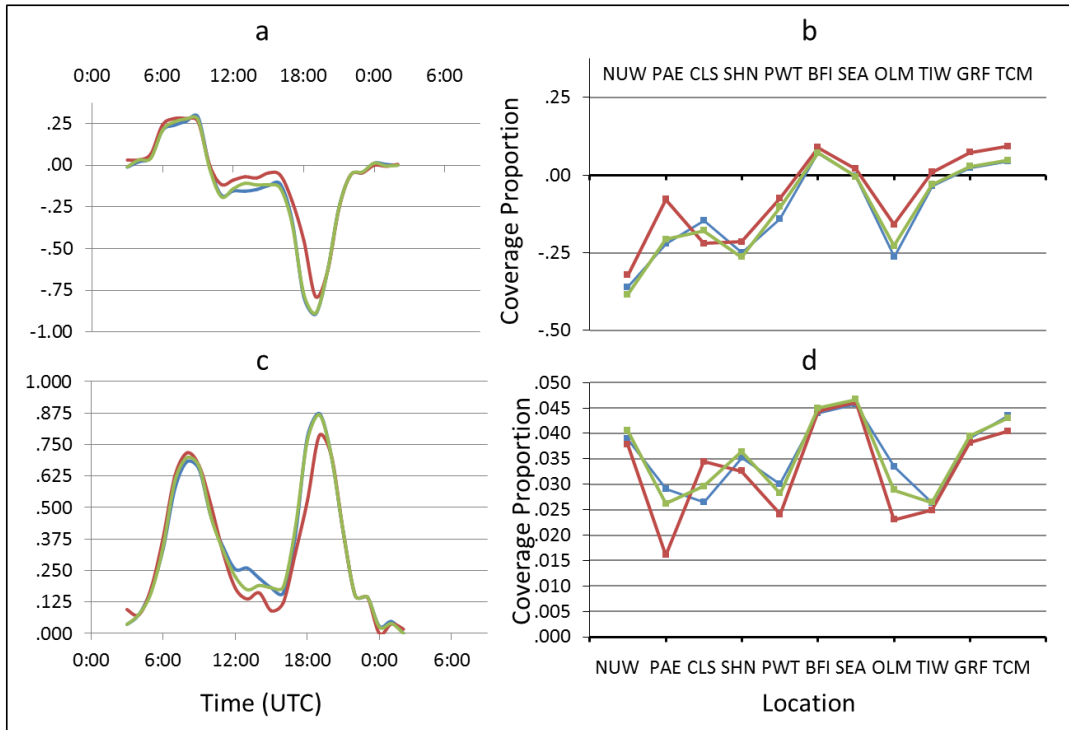


Figure 34 Cloud coverage proportion mean difference (a and b) and root mean squared error plots (c and d) as evaluated against METAR for the 100 (blue), 1000 (burnt orange), and Aero (green) runs. Comparisons of all sites averaged together at each time are presented in the time series in a and d. Comparisons of each site averaged over all times are presented in b and d.

Remarkably, all models performed within 25% of the observed sky cover during onset (a) but their cumulative error shows at approximately 0700 UTC in panel c, as in Figure 33, that all configurations had significant difficulty maintaining the coverage over time, on average, until dissipation was complete and sky cover returned to near zero for all observations and forecasts. This is especially marked in Figure 34c, in which the RMSE is greatest for all configurations during dissipation time, yet low during the 1200 to 1500 UTC time in which stratus was observed to have set in and uniformly covered the PSB. Site to site, variation is not as marked as in the time series.

All three runs' mean daily coverage differed from observations by less than 25% at all but KNUW (the furthest location north downwind in this examination), and in the case of the 100 run, at KOLM. The 1000 run did show a trend of improvement over the 100 control run. Figure 34 shows that for half the sites, the 1000 run had the lowest mean daily difference from observations, and for 8 of the 11, the lowest RMSE. While the 1000 run produced quantitatively little or negative improvement in mean daily difference (Fig. 34b) over the 100 for locations greater than 20 mi upwind of the highest mean aerosol concentrations (KCLS, KSHN), the 1000 maintained more cloud cover (values numerically greater) on average over 10 of the 11 sites. While the 100 and Aero runs performed nearly identically in their improvement over the 1000 run at KBFI, KSEA, KGRF, and KTGM, the 1000 run's positive difference values at those locations indicate that it had greater cloud cover than the 100 and Aero, and greater coverage than was observed, on average. While these performance differences are small (0.05 and 0.04, respectively), and well within the standard deviation of each (0.14 of the sky for both), this qualitatively shows the order of magnitude increase in prescribed droplet concentration did make some difference in coverage over the default N_d prescription of the 100 model configuration. The RMSE differences for the 1000 (Aero) versus the 100 are likewise indeterminate, at only -0.003 (-0.0001) of the sky. Finally, note the anecdotal fact that for every location within 5 to 10 mi (KTGM, KGRF, KTIW) or downwind from the highest climatological concentration of anthropogenic aerosol (KSEA, KBFI, KPAE, KNUW), both the daily mean difference and RMSE are smaller for the 1000 run than the 100 run.

A punctuating statistical evaluation of the coverage data for this case day is obtained when examining the binary forecast skill of each model for the occurrence of ST ceilings or no ST ceilings. Counts of these forecasts are shown the contingency tables for binary occurrence prediction of fractional coverage greater than half (Table 4). The site data are aggregated for the case day such that all model “hits” across sites are shown in one table for each model. Summary statistics for these data are presented in Table 5.

Table 4 Two by two contingency tables for the binary prediction versus observation of sky cover less than half (CLR to SCT) or greater than or equal to half (BKN to OVC) on 18 July 2013 for the 100 (A), Aero (B), and 1000 (C) runs, gathered for each model run at each site and then aggregated to one daily table for each model run.

A) 100 N _d		Observed	
Forecast	\geq BKN	< BKN	Total Fcst
\geq BKN	76	25	101
< BKN	57	130	187
Total Obs	133	155	288

B) Aero		Observed	
Forecast	\geq BKN	< BKN	Total Fcst
\geq BKN	79	25	104
< BKN	54	130	184
Total Obs	133	155	288

C) 1000 N _d		Observed	
Forecast	\geq BKN	< BKN	Total Fcst
\geq BKN	88	24	112
< BKN	45	131	176
Total Obs	133	155	288

Verification frequency of ST ceilings was closer to perfect for the 1000 run than either of the other two. All three configurations fared relatively well in the 40th to 50th percentile of observed frequency, but that there were deficiencies for all models just above this frequency, on the order of 30-40% missed. This result adds weight to the body of evidence that each model under-forecast cloud cover in general. Greater differences can be gleaned from the summary statistics calculated for this case (Table 5).

Table 5 Summary statistics for prediction of occurrence or non-occurrence of cloud cover greater than or equal to half (BKN) on 18 July 2013 computed hourly for each station and then aggregated hourly for all stations. Columns 1 through 5 represent Percent Correct (PC), Hit Rate (HR), False Alarm Rate (FAR), Equitable Threat Score (ETS), and Frequency Bias, respectively for the given criteria.

A	PC	HR	FAR	ETS	Frequency Bias	
					0.759	\geq BKN
100	71.5%	75.9%	0.16129	0.264	0.813	< BKN
					0.782	\geq BKN
Aero	72.6%	78.2%	0.16129	0.282	0.832	< BKN
					0.842	\geq BKN
1000	76.0%	84.2%	0.15484	0.345	0.877	< BKN

For the 288 opportunities across the 24-hr period of observation (0300 to 0259 UTC) at 11 locations, the 100, Aero, and 1000 runs produced 71.5, 72.6, and 76.0 percent correct (PC) forecasts, respectively (Table 5). The Aero (1000) performed 1.5% (6.3%) better than the control 100 run as a percentage of the control forecast PC. Hit Rates for the Aero and 1000 runs were 3% and 11% improvements over the 100 HR, although the False Alarm Rate (predicted but not observed, FAR) for all runs was practically equal in mediocrity. The FAR

shown for every model (at almost every location) was primarily due to early onset of predicted stratus compared to observations. Similarly, the miss rate (occurred but was not forecast, not shown) was mostly due to early dissipation of model cloud at every location, with the penalty accruing hourly. Comparing Equitable Threat Score (ETS), in which 0 indicates no skill and 1 is perfect in a range from -1/3 to 1, reveals that all model configurations exhibit skill in a forecast accounting for potential success due to random chance. Both the Aero and the 1000 runs exhibited greater skill (6.8% and 8.1%, respectively) than the 100 forecast. Frequency bias (1 is perfect) indicates that while all model configurations under predicted cloud cover on this day, both the Aero and 1000 run showed improvement over the control, at 2.3% and 10.9% (2.4% and 7.8%) better for coverage greater than or equal to (less than) 50% of the sky.

Paired sample t-tests were performed for the Aero and 1000 run versus the 100 for the binary conditions. The p-values for both (0.781 and 0.2188, respectively) indicate that the null hypothesis of equal means cannot be rejected for the Aero and 1000 forecasts versus the 100. Furthermore, the 95% confidence interval for the 100 mean (with a range of 0.621 to 0.789) does contain the sample estimate for the Aero forecast (0.726) showing that the Aero forecast is not different from the 100 at a confidence level of 95%. These results are confirmed for the 90% confidence level. However, the 95% confidence interval for the 100 versus the 1000 is 0.588 to 0.753, and the sample estimate for the mean of the 1000 forecast is 0.760. This value is outside of the 100 95% confidence interval, indicating that there is a statistically significant difference between the 1000 and the 100.

The persistence forecast (defined as the previous day's METAR observations for each location at each time are used as a forecast for the following day) was worse than every other predictor on this case day. Persistence missed 110 of 288 opportunities (38%, not shown). The persistence forecast was equal to the 100 at Bremerton, with only the Aero and 1000 showing a better forecast over persistence there. These results are not significant indicators of good model skill at KNUW and KPAE. Instead, they are likely indicators that persistence faltered in those locations due to the fact that an upper level cold pocket and 500 hPa minor short wave trough transited British Columbia the previous day, causing the first half of 17 July to be unrepresentative of 18 July for stations like KNUW and KPAE in the northern PSB.

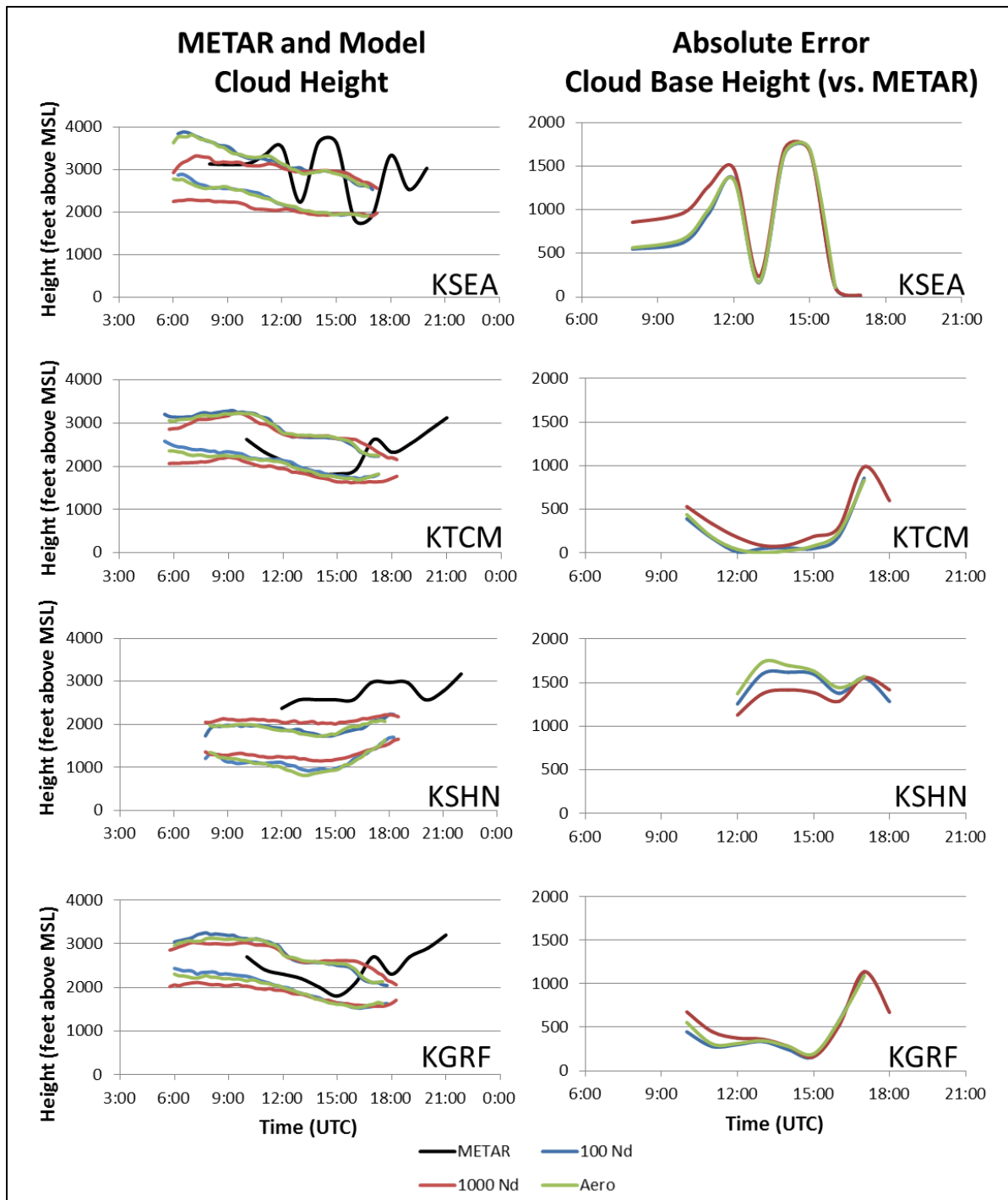
3.3.3 Point-Forecast Cloud Base and Top Height and Geometric Thickness

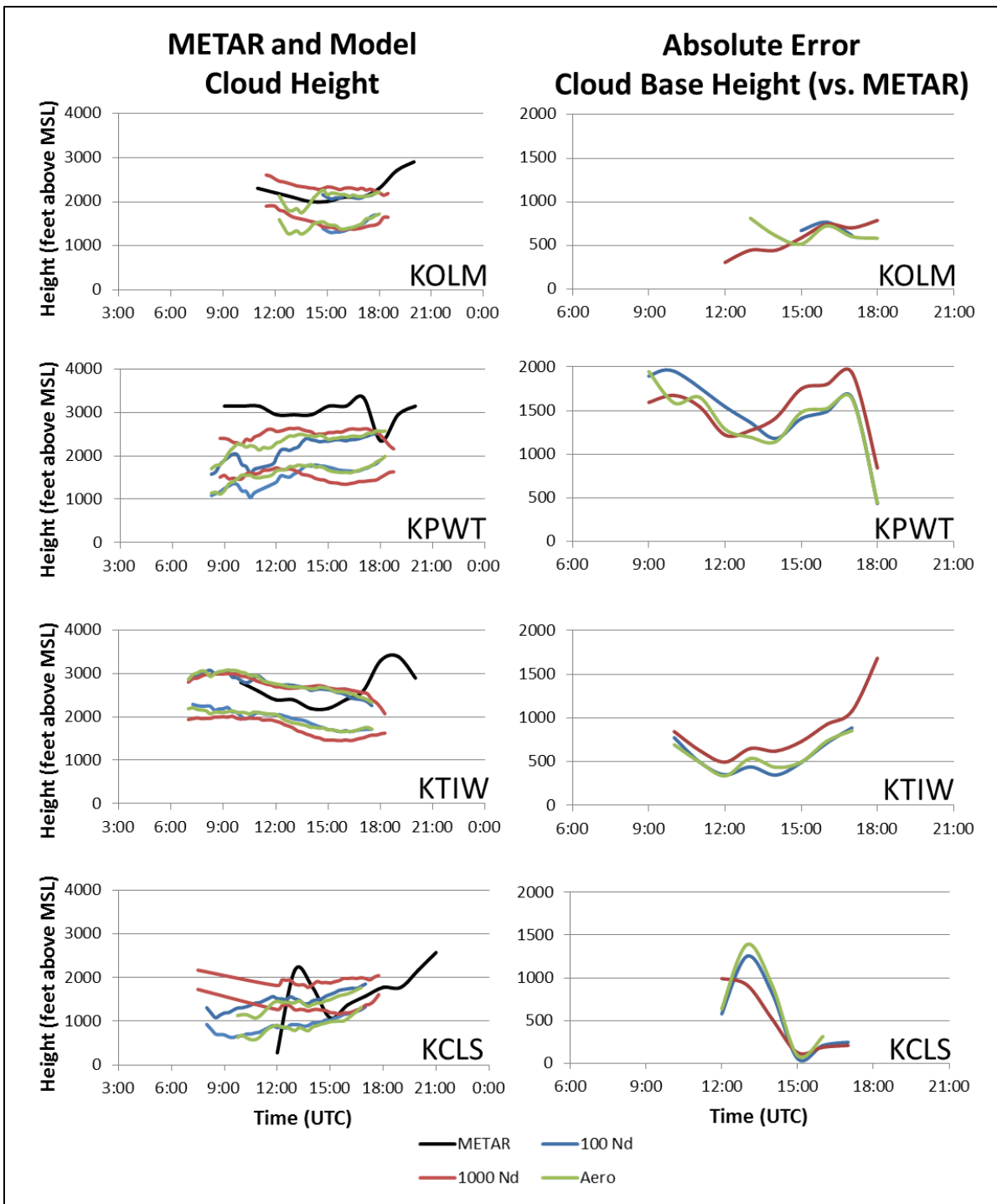
This section explores the value of the three model configurations in correctly forecasting cloud base and top heights and geometric thickness. Personal experience indicates the exceeding difficulty of cloud base height forecasting at 24 to 36 hours out. Accurate forecast aids greatly assist in this task. This analysis follows the verification comparison of model ceiling forecasts (averaged heights when greater than or equal to half of the grid columns within a 10 mile radius contained cloud) versus observed ceilings (greater than or equal to 5 okta, or BKN skies). As the previous section discussed, cloud cover was a difficult forecast parameter for the three model configurations presented here, making consistent representation of breaks in lower versus upper ST layers beyond the reasonable reach of the present model settings and data collection practices. This necessitated a

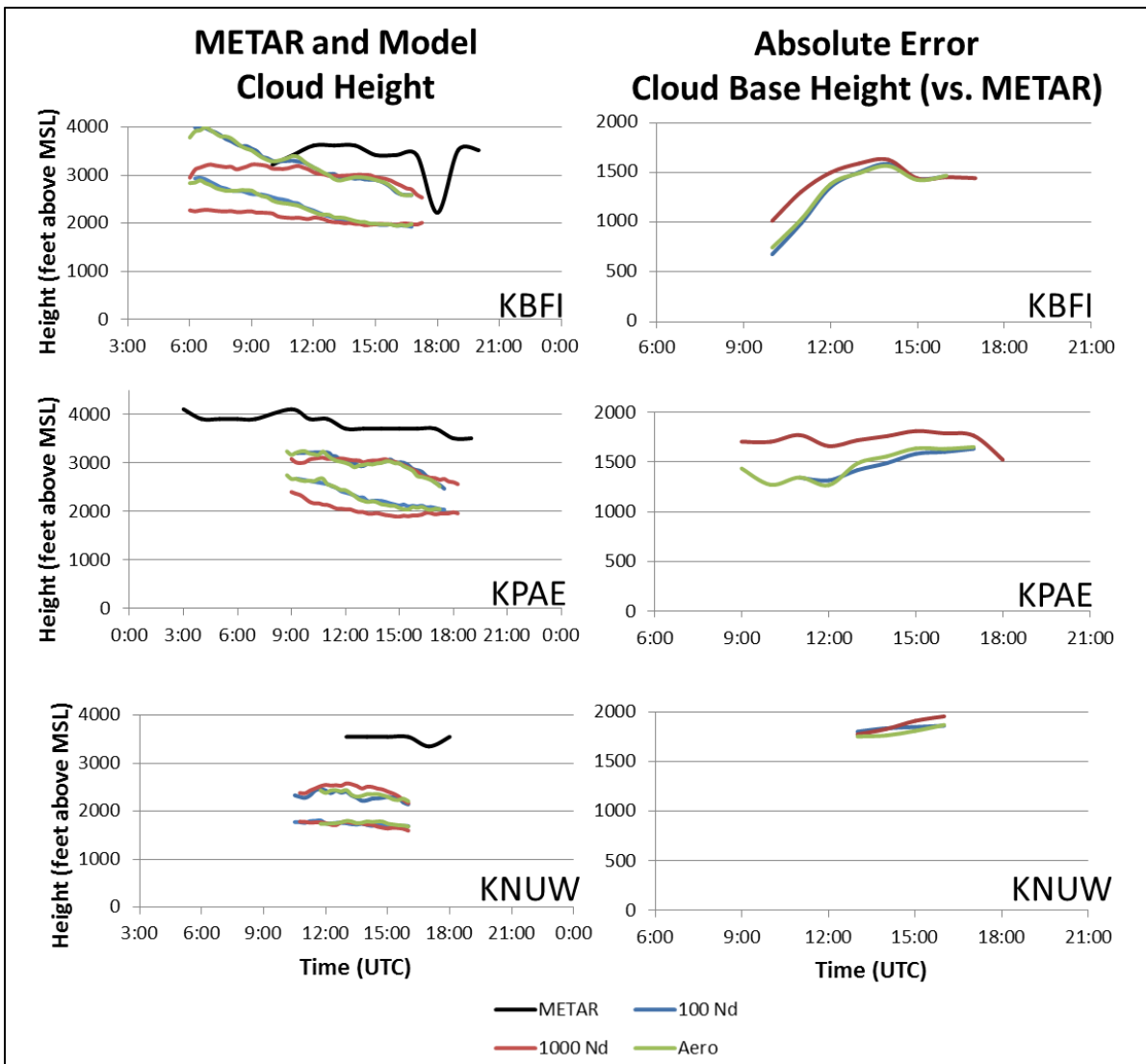
verification approach in which all “ceiling” heights were used for both model and observed cloud, regardless of duration.

Figure 35 shows mean model ceiling base and top heights with METAR ceiling height for the 11 locations of observation (left column) as well as hourly absolute error plotted for each model (right column) by time of observation. One key aspect of this data is that at times, even the cloud top forecast for KSEA was below the METAR ceiling height, due in part to the method with which model data were tabulated, and due in greater part to the inability of each model to accurately forecast ceiling heights, as this analysis will show.

Figure 35 Observed and model forecast cloud heights (left column) and absolute error (right column) for 18 July 2013 at locations in the Puget Sound Basin. METAR heights are bases only, while model forecasts for 100 (blue), Aero (green), and 1000 (blue) base and top height are provided for perspective.







Another key aspect of Figure 35 is the difference in ceiling forecast accuracy between various locations. At KTCM, for example, much of the observed ceiling was accurately predicted to within 9 feet measured by absolute error (Aero run 12 through 15 UTC). However, the same model runs under predicted ceiling heights at KSHN by about 1,500 ft the entire day despite the fact that KSHN is only 28 miles from KTCM. Although KSHN is upstream of the main pollution source for the wind direction of this event, even the 1000 run under predicted ceiling heights by over 1,000 ft the entire day. This finding is evidence that other controls besides cloud droplet number concentration alone, such as initial conditions or boundary layer parameterization, are more important in determining cloud base height, as found by Coniglio et al. (2013) and others.

Examination of the observations for KCLS elucidate that the cause for the curious observed evolution of cloud from 1200 to 1500 UTC was that dense fog obscured the sky to 100 ft vertical visibility in the several minutes leading up to and including the 1200 UTC observation. This fog layer fractured before the 1300 UTC observation, leading to a sudden increase in the cloud base trend shown, and illustrating sensitivity to dense fog events in the methods used here. The 1400 UTC METAR reports a ceiling of 1,400 feet before the appearance of a 900 ft layer at 1500 UTC. Once the lowest cloud layer stabilized there, it was well predicted by all three runs.

The model cloud base height trend is clearly similar for the 5 upstream stations. When viewed on a map, a pattern to this finding emerges (Fig. 36).

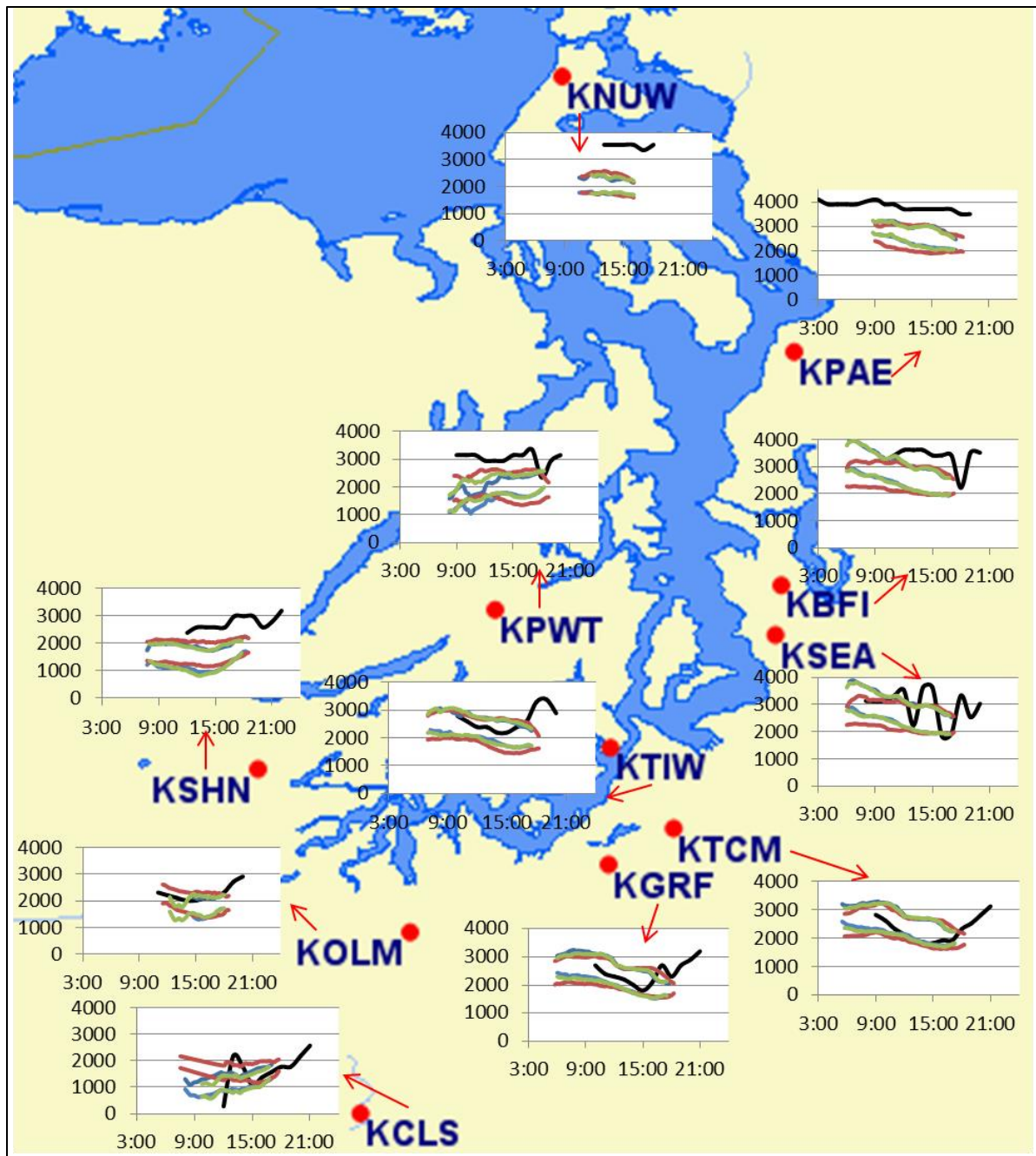


Figure 36 As in Figure 15, except with model cloud base and top forecast by the 100 (blue), 1000 (burnt orange), and Aero (green) runs added to location plots.

This is further evidence that either the cloud in both the model and the observations was different along the windward slopes of the Cascades, that another mechanism besides solar heating contributed to model stratus dissipation these sites, or both.

The purpose of Figure 36 is to show that model representations of cloud height evolutions are different for different geographic locations, showing a trend in model behavior. The plots for KCLS, KOLM, KSHN and KTIW and KPWT show classically rising cloud base heights indicating bottom-up stratus erosion consistent with observed trends. Model trends are most dissimilar from the observations at KTCM and KGRF where the downward trend in model cloud base heights continues even while observed values rise significantly after 1500 UTC. The remaining locations observed cloud either steady with time, or with entire layers lowering with time for most of the day at until an undiagnosed model dissipation process began and the model cloud was evaporated. All of these locations are along the southeast, east, and northeast periphery of the Sound. At all other locations besides KTCM and KGRF, both the observations and the forecast show cloud layers rising with time. These two locations are very close to the eastern locations which observed steady or falling inversion tops over time. The forecasted change in sign of vertical velocity above the inversion from 15 to 18 UTC (Fig. 37) suggests that each model attempted to represent the additional subsidence observed atop the inversion, but extended this forecast to points further west than observed as evinced by the bull's-eye near KTCM and KGRF at 18 UTC.

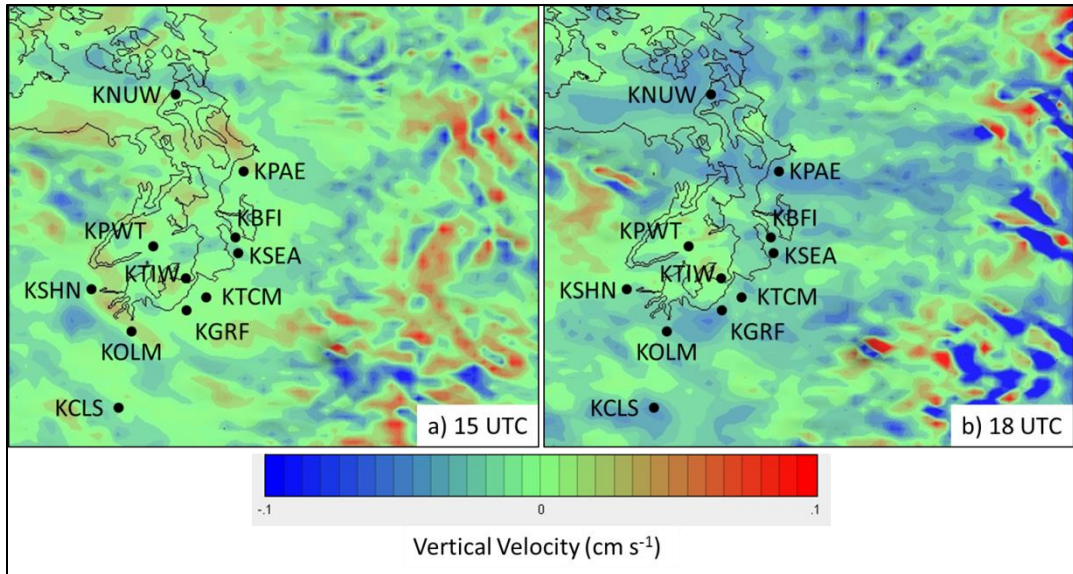


Figure 37 Vertical velocities (cm s^{-1}) at sigma level .851 for 15 (a) and 18 UTC (b).

Due to the timing differences of the forecast cloud versus the observed cloud, hourly absolute error is not an effective statistic to determine accuracy for model base height forecasts presented here. Therefore, each hourly model and observed height was aggregated into a daily mean value for each location, removing the signal of timing error from base height error. The RMSE was then calculated for these values, as the difference of the means is equal to the means of the differences. The plot in Figure 38 shows the daily mean value for the observed and forecast cloud base height (a) and the RMSE for each (b).

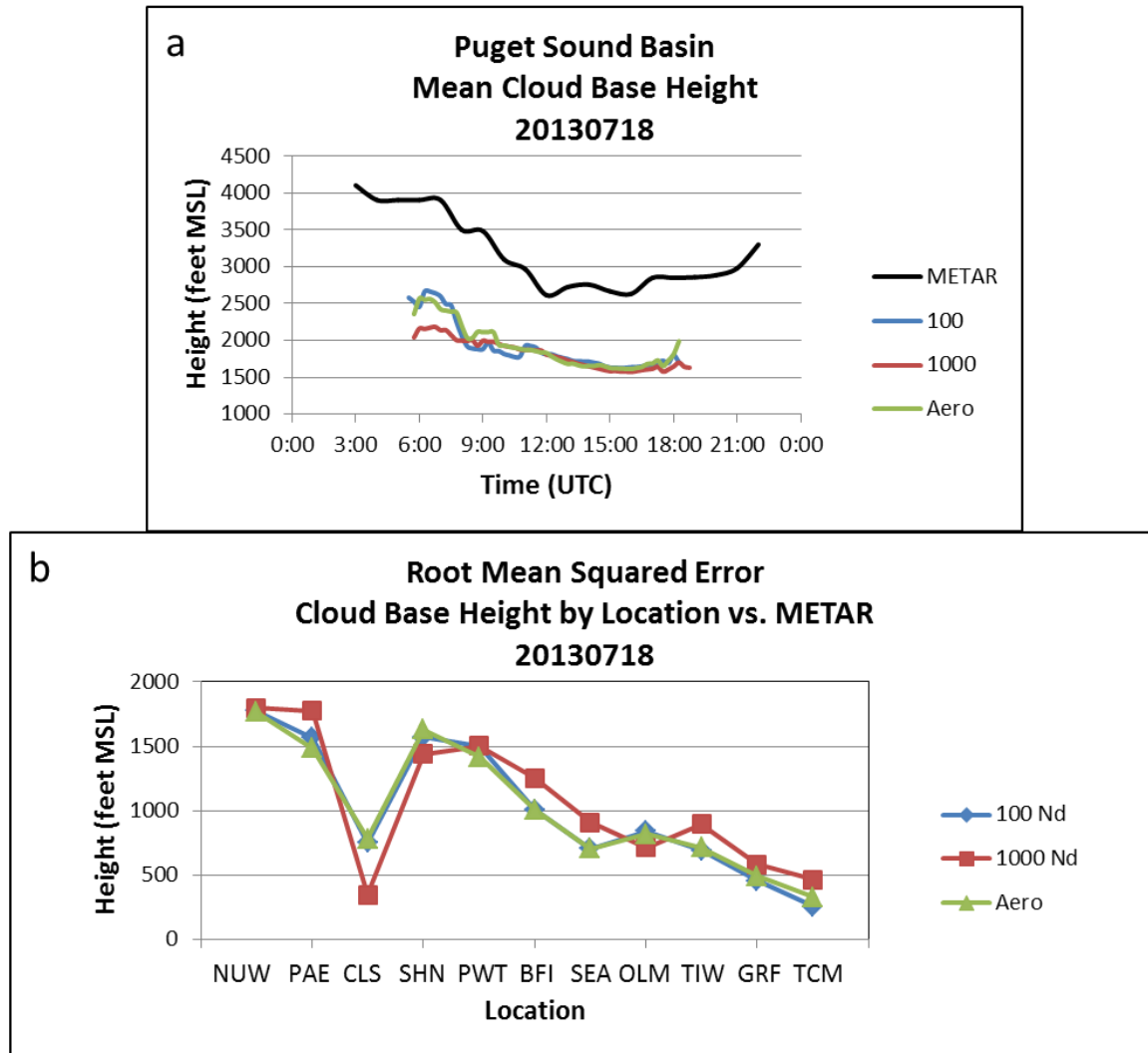


Figure 38 Time series of mean cloud base heights for 18 July 2013 over all locations (a) and RMSE calculated for each location's daily mean versus METAR (b) in feet MSL. Values shown are for METAR (black), 100 (blue), 1000 (burnt orange), and Aero (green).

Based on the RMSE shown here, the 1000 (burnt orange) was consistently the worst performer, under forecasting cloud base height by an average of 1,062 ft, compared to 1,011 ft and 1,013 ft for the 100 and Aero, respectively. None of these values are outside the standard deviation and none are statistically significant. The results here indicate that

models' variation by location has a far greater impact on ceiling height forecast than cloud droplet number concentration variation.

While the METAR data set is more widely available, there is a suspicion that the METAR observations include a high bias for cloud bases. Comparison with the TAMDAR data set for this case could provide some clarity. Figure 39 shows a time series of all the TAMDAR observed values for cloud base height and top height observed in this case day within 10 mi each of KSEA and KBFI.

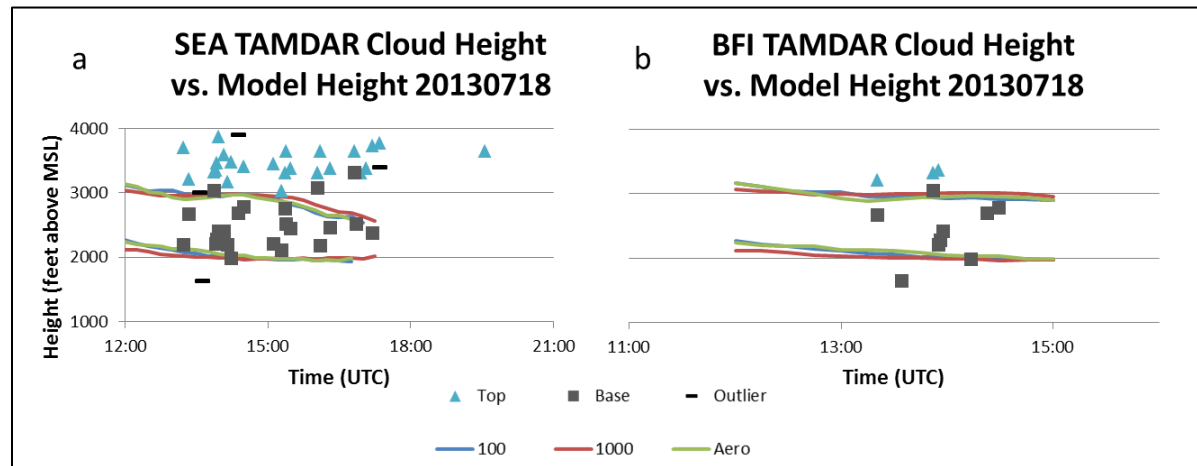


Figure 39 Time series of TAMDAR observed relative humidity values of $\geq 99.5\%$, indicating cloud base (gray boxes) and cloud top (blue triangles) observed during 18 July 2013 KSEA (a) and KBFI (b). Statistical analysis of the samples for cloud base and cloud top heights excluded the outliers (black dashes) as values lying outside the mean by more than two standard deviations.

The observed TAMDAR data present wide variability (Table 6) and model forecasts for these heights (Table 7) are more representative than the METAR comparison shows.

Table 6 Statistical data for the TAMDAR observation values (in feet) taken 18 July 2013 and presented in Figure 39.

a) KSEA	Count	Mean	Min	Q1	Median	Q3	Max	Std Dev
Top	21	3476.7	3030.0	3360.0	3470.0	3670.0	3740.0	194.4
Base	23	2515.7	1980.0	2210.0	2440.0	2725.0	3320.0	344.8
b) KBFI	Count	Mean	Min	Q1	Median	Q3	Max	Std Dev
Top	7	3322.9	3000.0	3210.0	3360.0	3440.0	3480.0	169.5
Base	10	2473.0	1640.0	2227.5	2540.0	2757.5	3040.0	454.5

Forecast verification against these data for the period of observation in which TAMDAR were collected was performed by taking a daily mean and differencing the observed value from the forecast value.

Table 7 Forecast for KSEA (a) and KBFI (b) cloud base and top heights (in feet) compared to TAMDAR observations in Table 6.

a) KSEA		100	1000	Aero
Base	Mean	2290	2088.9	2292.4
	Std Dev	316.177	135.714	292.856
	Diff	-225.7	-426.8	-223.3
Top	Mean	3212	3232	3227
	Std Dev	380.837	177.203	358.973
	Diff	-264.7	-444.7	-249.5
b) KBFI				
Base	Mean	2355.7	2113.6	2357.1
	Std Dev	332.699	115.393	313.626
	Diff	-117.3	-359.4	-115.9
Top	Mean	3249	3041.8	3262.2
	Std Dev	414	168.109	412.635
	Diff	-73.9	-281.1	-60.7

It is clear from the statistical analysis that all three model runs still under forecast the height of the cloud base observed by TAMDAR, although the performance is better than when compared to METAR. However, given the small sample size, and the fact that these data are for one location, these results are hardly conclusive.

Using these same data, we can glean a small clue about each model's mean representation of cloud geometric thickness (Figure 40). According to TAMDAR, the absolute mean geometric thickness forecast error for both sites for all hours was 41.2 ft, 130.2 ft, and 41.1 ft for the 100, 1000, and Aero, respectively. The 1000 produced the thickest mean cloud deck at 1035.7 ft, followed by 919.6 ft and 907.7 ft for the Aero and 100, respectively.

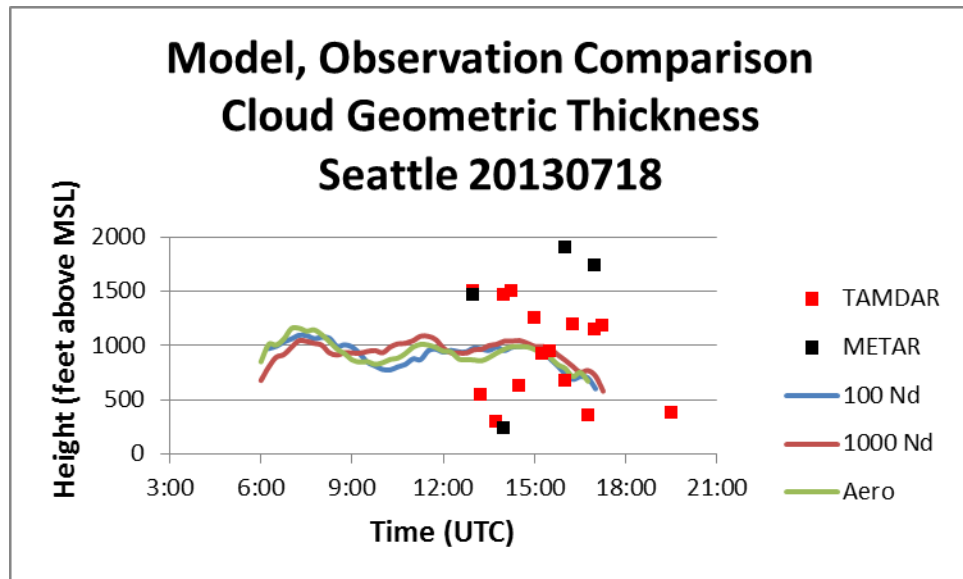


Figure 40 Time series showing mean daily cloud geometric thickness forecasts for all sites averaged at each time for the 100 (blue), 1000 (burnt orange), and Aero (green) forecasts versus TAMDAR (red squares) and METAR (black squares) values.

Although these data are limited to two locations and only a few hours of observation, they agree with previous findings for cloud depth changes with increased droplet concentration (Ackerman 1995, 2000; Randall 1984). Figure 41 shows (as does Fig. 40) that in the hours immediately after formation, the stratus predicted by the Aero run was the deepest of the three model clouds. Importantly, as the marine push continued to mix clean Pacific air into the PSB and replace the aerosols (Fig. 18), thickness dropped off sharply, while the stratus produced by the 1000 run maintained its depth. This is another indicator that that model setup may be responsible for premature removal of aerosols. The wind fields (Fig. 12) and aerosol distributions (Fig. 18) point to depletion of numerous CCN as the cause. If the Aero cloud seeds had lingered or been replaced rapidly enough, it is possible the Aero stratus could have maintained the greatest depth, and thereby maintained the greatest lifetime. A sensitivity test for increasing aerosol production rate is discussed in the next chapter.

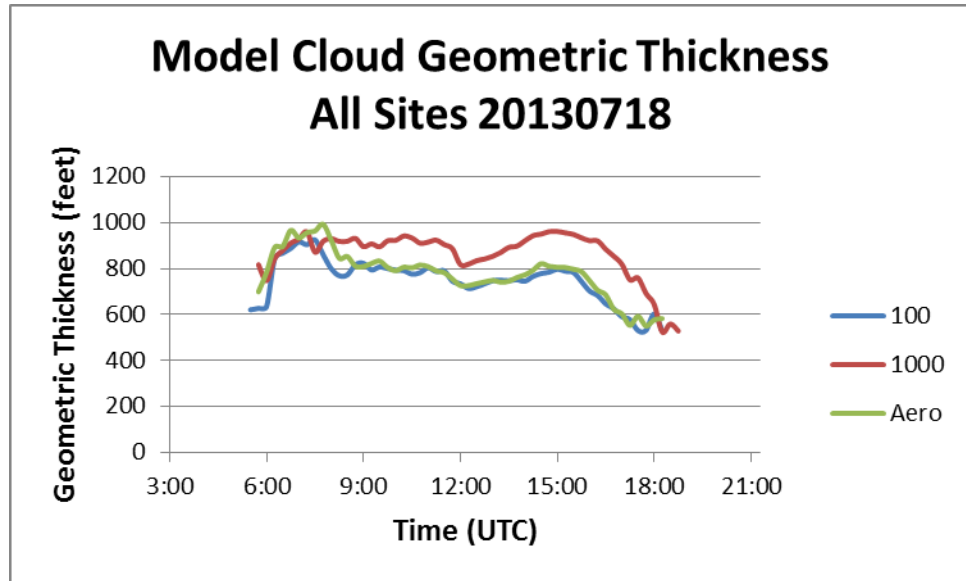


Figure 41 Time series of model cloud geometric thickness (in feet) valid 18 July 2013 for the 100 (blue), 1000 (burnt orange), and Aero (green) runs.

3.3.4 Point-Forecast Timing Forecast Verification

Using the metric mean absolute error, each forecast for the onset (sky cover becoming greater than half) and dissipation (becoming less than half) for the event of 18 July 2013 is compared in the box-and-whisker plot below (Fig. 42) and Table 8.

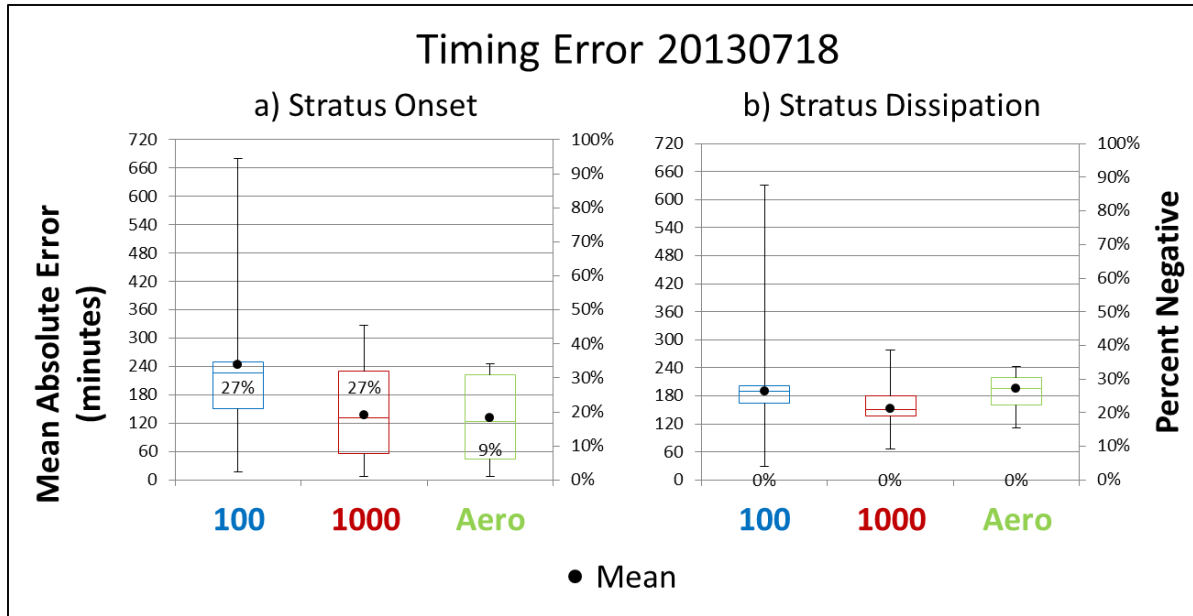


Figure 42 Box-and-whisker plot of mean absolute error (MAE) in timing (minutes) stratus onset (a) and dissipation (b) forecasts for all locations aggregated for 18 July 2013 for the 100 (blue), 1000 (red), and Aero (green) runs. The percentage of forecasts which were late predicting an event (% Negative) is overlaid (right vertical axis). Percent Negative is a measure of forecast bias in distribution (50% = normally distributed, 0% = early bias, 100% = late bias). MEA observed for each forecast is shown with a solid black dot.

Consistent with results throughout this study, the 1000 run exhibited value over the control and the Aero, to the tune of over 2 hr improvement over the default on average. The Aero run improved the onset forecast more than the 1000 did, and was well within the margin of error at dissipation timing. These data are evidence that at even a small amount of variability, double-moment droplet number concentration prediction improved stratus onset timing in the PSB in this case. The early burn off of the Aero stratus compared to the 100 run in this case adds to building evidence suggesting a systematic fault in how TE14 supplies aerosol to the boundary layer, particularly under stagnant conditions such as a stratus regime, a time in which pollution typically accumulates in the physical world. The MAE of stratus

timing in this case is high compared to under other conditions and other cases tested. A very brief summary follows in the Sensitivity Tests section.

Table 8 Change in mean absolute error between the 100 control run and the 1000 (a) and Aero (b) forecasts for the onset and dissipation of stratus for 18 July 2013. Values shown are control minus experiment such that positive values are improvement over the control. The “Combined” column indicates the total error difference when using one model (onset MAE + dissipation MAE) versus the control total or a proportion of the control combined MAE.

a) 100 - 1000	Onset	Dissipation	Combined
Median Difference	95.0	38.0	133.0
Median % Change	42.0%	20.1%	32.0%
MEA Difference	108.2	36.8	72.5
MEA % Change	44.2%	19.4%	33.4%

b) 100 - Aero	Onset	Dissipation	Combined
Median Difference	102.0	-7.0	95.0
Median % Change	45.1%	-3.7%	22.9%
MEA Difference	112.6	-5.5	53.6
MEA % Change	46.0%	-2.9%	24.7%

3.4 Sensitivity Tests

The general model representation of inversion height (lowering with time) aided in premature stratus dissipation. Figure 43 shows 850 hPa omega (shaded, 10^{-1} Pa s $^{-1}$) for the NAM218 00 hr analysis (a, NCDC 2015) and for the 100 forecast, both valid for 18 July 2013 at 18 UTC, during dissipation of model stratus.

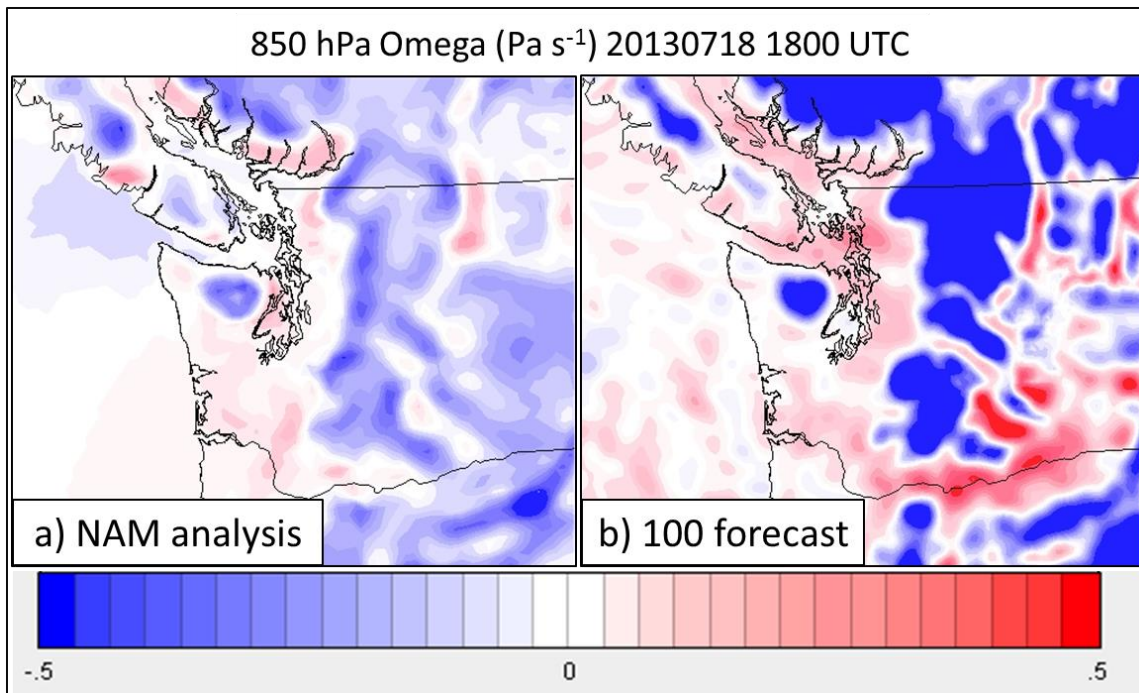


Figure 43 Comparison of 18 July 2013 1800 UTC 850 hPa Omega (Pa s^{-1}) observed (represented by the NAM218 grid analysis, a) and forecast by the 100 run (b). The 100 over-forecasted subsidence above the inversion (indicated by the excess of pressure increase over the PSB in b as compared to a) during the stratus dissipation period, leading to early dissipation in the model.

At 18 UTC, the model produces relatively large values of subsidence over the eastern PSB (b), in excess of the observed subsidence above the inversion (a). This excess in model subsidence was conducive to lowering the inversion height for eastern Sound locations. This is evidence that a small forecast error in dynamic controls such as vertical velocity had a much greater impact on cloud lifetime than even a tenfold increase in cloud droplet number concentration, as model cloud dissipated near the valid time of Figure 43, yet lasted three more hours in reality.

If vertical motions are removed, as with a single column model, it is possible to test to see whether the model cloud would have lasted, given the changes applied to the 1000 run.

Figure 44 compares the single column model forecast cloud water mixing ratio (a and c) and surface downwelling shortwave radiation (b and d) of the 100 run (a and b) versus the 1000 configuration (c and d) initialized from the 12 UTC 100 model sounding at Seattle on 18 July 2013.

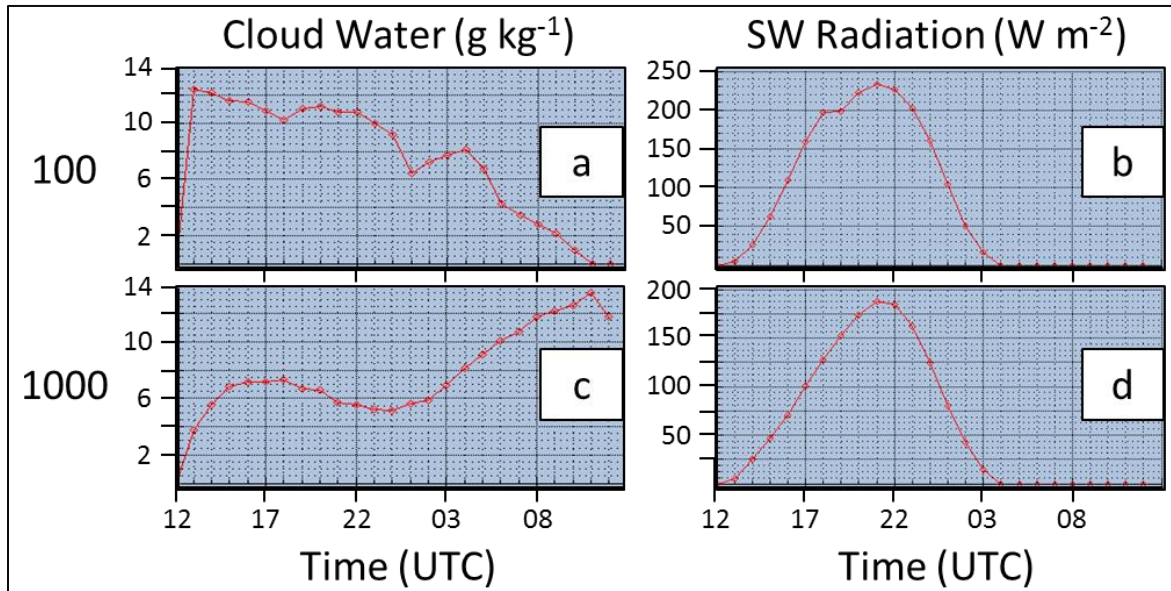


Figure 44 Time series of Seattle forecast cloud water (g kg^{-1} , a and c) and downwelling shortwave radiation at the surface (W m^{-2} , b and d) for the 100 run (a and b) versus the 1000 run (c and d) for 18-19 July 2013. Note the different vertical axes values of b and d.

This figure shows what may have happened in the absence of the greater forcing of subsidence. The 100 run cloud dissipated (a), albeit later than the observed 2049 UTC, while letting 230 W m^{-2} of sunlight reach the ground (b). Compare this to the 1000 forecast cloud, which let only 185 W m^{-2} of sunlight in and lasted overnight.

Failure of the model to represent dynamics could also result from inadequate initial conditions. Comparison of MAE for onset and dissipation time at all locations for two stratus

case days (18 and 22 July 2013) for which the ERA-Interim (80 km grid spacing, taken as an analysis input every six hours during 42-hr model evolution) are presented in Figure 45 versus the NAM218 grid used for this study.

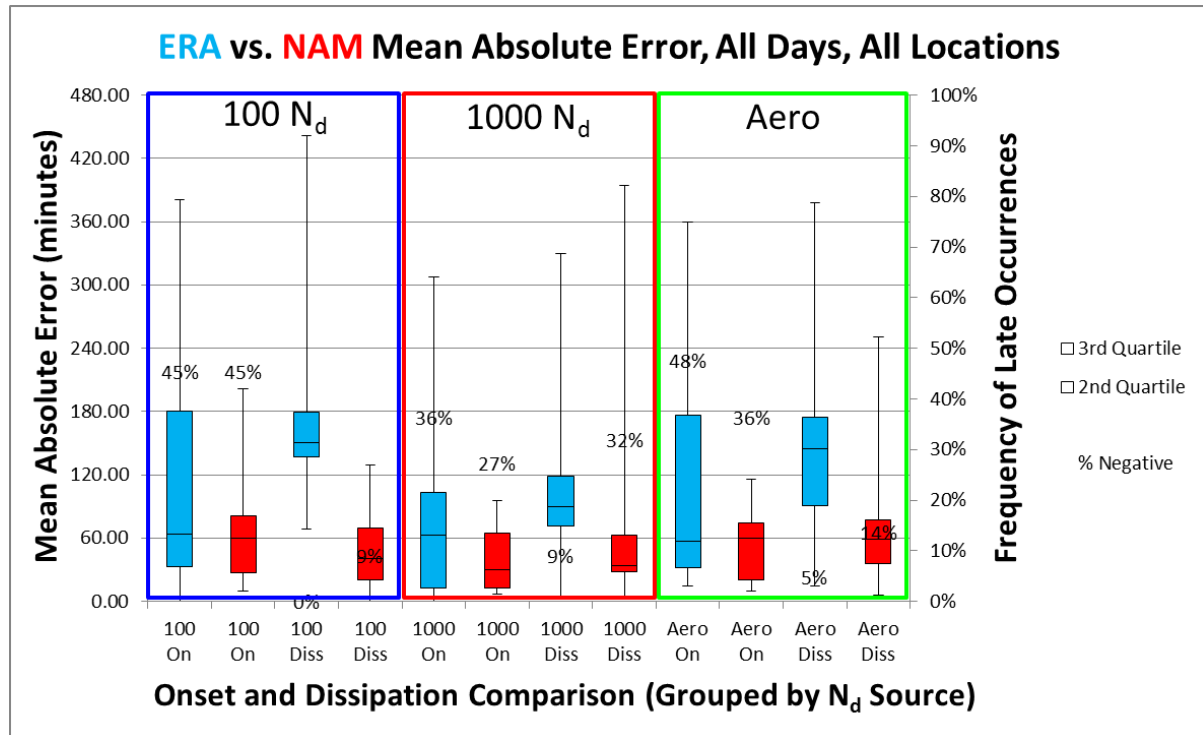


Figure 45 As in Figure 42 except for the 100 (royal blue box), 1000 (red box), and the Aero (green box) forecast onset (leftmost of each box) and dissipation (rightmost of each box) times calculated at each location daily for six model runs using the ERA-Interim (Carolina blue plots) and NAM grid 218 (NC State red plots) as initial conditions.

The gross inadequacy of the model to forecast stratus onset and dissipation timing with the ERA initial condition compared to the NAM is evident in the disparity between box and whisker plots for each run, 100, 1000, and Aero. This evidence is quantified further in Table 9, showing the MAE for the 1000 run of each initial condition calculated in the last row of each data column.

Table 9 Absolute Error (minutes, 0 = perfect) tabulation for 8 PSB observation locations comparing the performance of the ERA to the NAM as initial conditions for one run of the 1000 configuration. Mean Absolute Error is calculated at the bottom of each column. Note the ERA MYJ combination produced no cloud at CLS, PAE, and NUW.

	ERA MYJ		NAM MYJ	
	Onset	Diss.	Onset	Diss.
SEA	82	229	233	274
TCM	273	190	408	115
GRF	283	148	253	148
BFI	248	203	-67	128
OLM	131	159	-49	129
PWT	115	115	-5	115
SHN	76	166	226	136
TIW	107	158	32	128
MAE	164	171	129	147

The NAM-initialized runs outperformed those initialized with the ERA in head to head forecasts for ceiling onset and dissipation by margins of 27% and 16%, respectively. The NAM resolution is more than a factor of three finer than that of the ERA-Interim, although direct attribution of forecast difference cannot be made with the information given. However, a comparison of the initial model hour (analysis) Skew-t of the control run using ERA as the initial condition to that of the NAM analysis and to observed TAMDAR at the same time show a misrepresentation of the moisture profile existed for the grid cell nearest KSEA in the ERA data (Fig. 6) . The fact that this control produced such a large magnitude of change in model performance indicates that stratus onset and dissipation times are far more sensitive to initial condition than to cloud number concentration prescription. In

addition to varying initial conditions, running additional cases yields a clearer picture of whether value may be gained from explicit N_d prediction.

Beyond the initial conditions, this study observed additional sensitivity to PBL scheme choice. The cloud isosurface overlaid on satellite imagery in Figure 46 shows that cloud produced with YSU governing subgrid-scale PBL processes forecast too little cloud and, by the 1700 UTC valid time of this image, had eroded it even more quickly than the MYJ setup used in the body of this study. The table (10) following this graphic quantifies the timing error due to the PBL scheme selection.

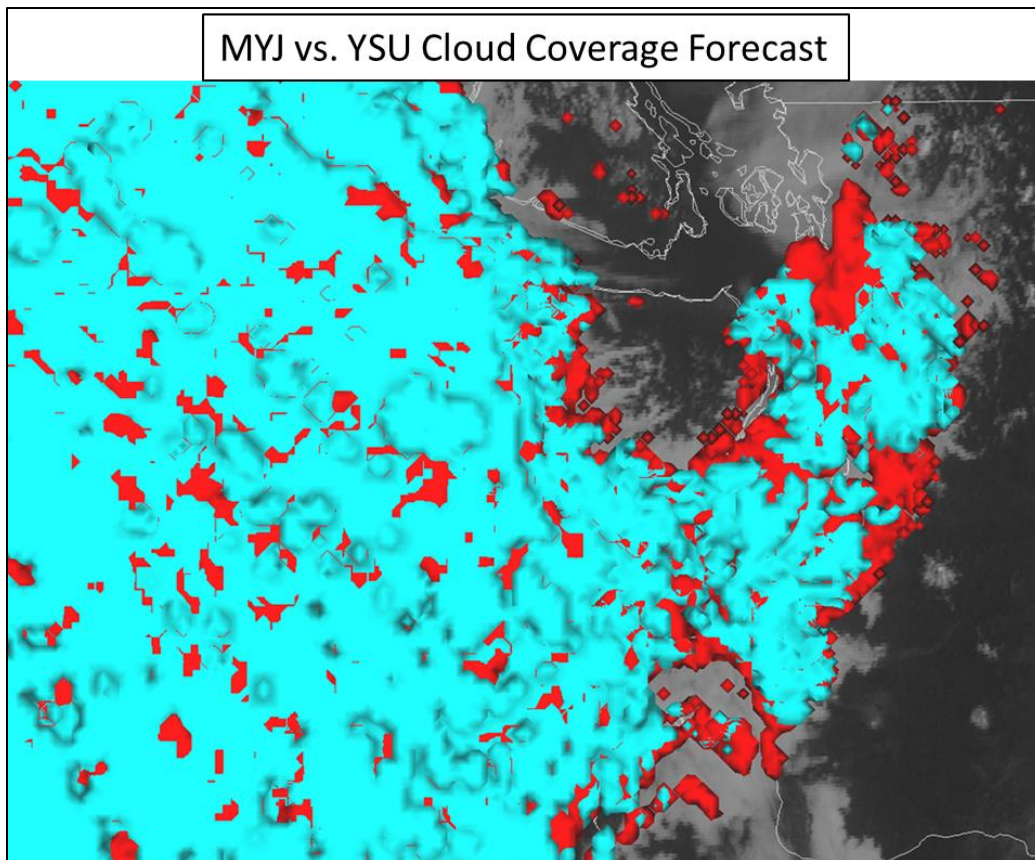


Figure 46 GOES15 Visible satellite image valid on 18 July 2013 at 1715 UTC with three-dimensional overlays for $5 \times 10^{-5} \text{ kg kg}^{-1}$ cloud water isosurfaces produced by a 1000 run with YSU (cyan) and MYJ (red) PBL schemes.

The YSU PBL scheme uses non-local closure, making it well suited to convective situations and other conditions requiring efficient and thorough mixing of the boundary layer. Initially, it was thought this scheme would produce more cloud water and denser cloud droplet number concentrations due to more thorough mixing of the scalar aerosol variable vertically through the PBL. The former did not happen because the latter happened too well. The vertical mixing of the YSU scheme was so efficient, that at the 1700 UTC image above, it had already eroded cloud out of many observation locations, leading to the disparity in

coverage seen in Figure 46, as well as the paltry MAE values in the Table 10. The YSU includes entrainment parameterization, which likely mixed dry air from the inversion layer into the PBL, dissipating cloud too early.

Table 10 As in Table 8 but comparing the NAM 1000 forecasts using YSU versus those using MYJ PBL schemes.

	NAM YSU		NAM MYJ	
	Onset	Diss.	Onset	Diss.
SEA	229	233	233	274
TCM	175	438	408	115
GRF	163	283	253	148
BFI	233	248	-67	128
OLM	174	131	-49	129
PWT	175	10	-5	115
SHN	211	151	226	136
TIW	158	62	32	128
CLS	840	400	100	210
PAE	79	98	-22	34
NUW	326	206	146	161
MAE	251	205	114	143

The YSU scheme fell behind the MYJ scheme by 120% for onset timing error, and 43% for dissipation timing error, a far greater spread than any noted between NAM runs differing N_d by even an order of magnitude.

Coniglio et al. (2013) found that mean evening and morning PBL height forecasts valid at hour 23 are 150 to 200 m too shallow when using local closure PBL schemes with WRF-ARW, as this study used, although that finding was for pre-convective stable boundary

layers, not marine ones. This amount would only account for half of the mean error observed in this study and as this study found, Coniglio et al. conclude that initial conditions are among the variables which contribute to this error.

Thompson and Eidhammer (2014) noted that the aerosol content of their model domain remained near that of the climatological average used as the initial condition. However, this study observed that under a much more docile regime, the aerosols in the Aero run were transported quickly from the southern Sound, dropping the concentration well below the climatological mean initial condition. One hypothesis as to why the Aero cloud did not maintain the duration or cloud geometric thickness of the 1000 cloud is that the once-plentiful CCN used as initial conditions were removed too quickly and the cloud did not endure for this reason. Investigation of the surface flux term in the TE14 scheme reveals that for grid lengths less than 20 km, surface production of aerosols is scaled down, despite the units remaining the same ($\# \text{ kg}^{-1}$). This takes Thompson and Eidhammer's constant flux value of 0.875×10^6 down to 0.2×10^6 for a grid length of 4 km, as in this study. A sensitivity test was run to examine whether the increase of surface production rate within the TE14 microphysics scheme would remedy this possible error. Cloud droplet number concentration increased at hour 24 of the forecast from 90 in the original Aero run to 130 (Fig. 47), while cloud layer (surface) QNWFA are seen at 5,000 to 6,000 ($10,000$) cm^{-3} compared to the original 2,000 to 3,000 (4000) cm^{-3} at this time. For comparison, the initial condition value for KSEA ($6.31 \times 10^9 \text{ kg}^{-1}$) results in an initial surface value of $\sim 7,700 \text{ cm}^{-3}$. These results suggest that despite an increase in aerosols to greater than the mean, the cloud

still did not endure, and reinforces the conclusion that other elements are more important than aerosol concentration.

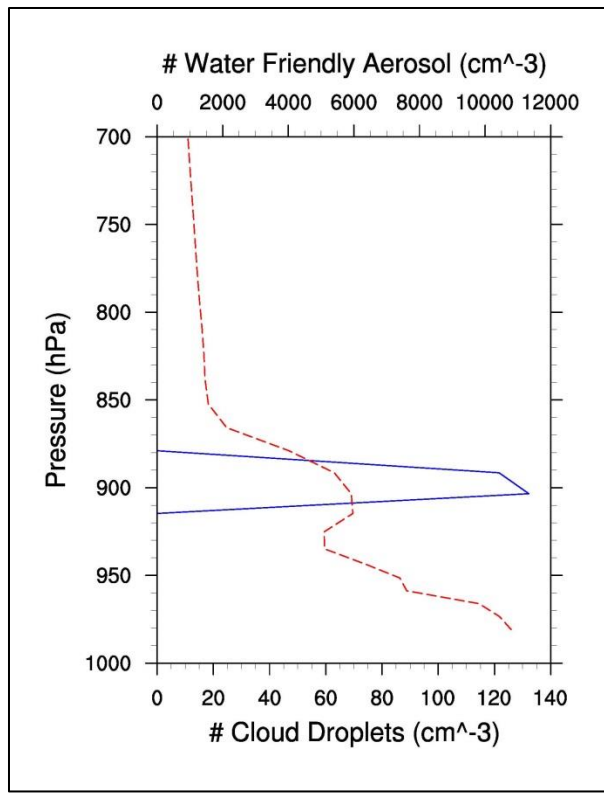


Figure 47 As in Fig. 26, valid at the same time, except as produced by eliminating the grid scaling factor of TE14 which reduced the surface aerosol flux by 80% for a grid length of 4 km from that of Thompson and Eidhammer's 20 km.

CHAPTER 4

4. Conclusions

It is common practice in operational single-moment cloud microphysics schemes to set a constant cloud droplet number concentration. In contrast, observations indicate wide variation in the background values of number concentration. In many situations, this does not lead to large errors, because the amount of condensate is controlled by the synoptic-scale vertical motion. However, in some meteorological settings, this assumption could potentially lead to significant error, particularly where cloud-radiation interactions can be altered by microphysical properties. One such scenario is the burn-off of stratus clouds over the interior of the Pacific Northwest. Here, cloud transmissivity has a direct linkage to cloud lifetime, and an unrealistically low droplet number concentration could lead to premature stratus erosion. In fact, WRF simulations of several summertime stratus cases in western Washington State featured premature burn-off of a forecasted stratus deck. The working hypothesis was that increasing the number concentration to a value more aligned with climatology could reduce solar transmissivity, maintaining a lower LCL and prolonging cloud lifetime.

A new coupled microphysics-radiation option in version 3.6 of WRF allowed for testing of this hypothesis. Implementation of this option yielded mixed results in the cloud forecast study presented here. Despite reduced solar transmissivity, cloud lifetime and coverage didn't exhibit significant changes.

4.1 Science Questions Answered

This study showed that the TE14 microphysics scheme successfully varies CCN concentration over space and time. This work found variations in cloud droplet number concentration produced by the new scheme, verifying that TE14 indeed allows this quantity to change as the dynamics and thermodynamics dictate; a definite step toward reality from prescribed, domain-wide constant concentration. However, evidence showed a rapid departure from the mean concentration, leading to a 50% deficit at hour 24 from initialization, and possibly premature dissipation of model cloud. Sensitivity testing for this factor corrected the aerosol number and increased N_d , but did not significantly prolong the cloud over Seattle due to other factors with more control.

Testing for the effect of increased N_d on cloud radiative properties revealed a statistically significant change in cloud transmissivity to shortwave radiation. The Aero and 1000 runs produced 3% and 16% mean increases in cloud opacity despite mean cloud water decreases of 6% and 21%, respectively.

The Aero and 1000 runs increased cloud coverage forecast skill over the control by 1.5% and 6.3%, respectively, achieving 3% and 11% higher hit rates (11% and 26% lower miss rates) for ceiling occurrence, respectively. However, no model showed increased skill over that of using persistence from the previous day.

Verification against METAR ceiling height data showed that no model showed statistically significant benefit over another. Comparison with TAMDAR observations showed a trend in greater cloud depth forecast for the 1000 and Aero runs over the 100, with the Aero matching both height values and cloud depth observations best.

Onset and dissipation timing forecasts by the 1000 run outperformed the control run by more than 2 hrs (MAE). The Aero run improved onset forecasts 46% over the control, while nearly equaling error of the 100 run in dissipation timing, perhaps the metric of the Aero run's greatest potential.

Sensitivity tests revealed a great deal about controls of variability in model cloud in this experiment. Altering the initial conditions in the control run from NAM grid 218 to the ERA-Interim resulted in 27% and 16% increases in timing error for 18 July and a nearly fourfold increase in dissipation timing error when combined with 22 July 2013 data (Fig. 45). Testing forecast coverage and timing of stratus with the non-local closure of the YSU scheme showed it to create less cloud in the domain and to dissipate it faster, to the tune of 120% worse mean onset and 43% worse mean dissipation forecast error.

4.2 Implications

Evaluation of forecast cloud coverage, height, and timing verification revealed that several factors accounted for greater variability in model cloud formation and dissipation than cloud droplet number concentration. The ERA-Interim initial condition provided the model too warm and too dry an initial condition which likely led to wider variability in cloud forecast timing and coverage measured here than any other factor. Dynamics are perhaps primary among the factors with greater importance. It is likely that a relatively small forecast error in vertical motions and divergence lowered the model inversion over the PSB and led to the premature dissipation of the model cloud in all three configurations, despite a tenfold increase in cloud droplet number concentration in the 1000 run. Although increasing cloud droplet number concentration does change cloud radiative and operational forecast qualities,

these results suggest that improvements in model dynamics, observation, and data assimilation could amplify improvements in cloud droplet number concentration representation.

4.3 Future Work

Implementing TE14 CCN and N_d variation yielded more realistic forecast cloud physical and radiative properties than the default domain-wide constant $100 \text{ N}_d \text{ cm}^{-3}$. This tool should be tested in many different real-world and idealized stratiform cases, such as the subtropical SC fields of the east Pacific, to test the significance of the radiative property changes found here. Additional testing should focus on tracing the aerosol production and advection of the scheme, including sensitivity tests for the scaling factor and comparison with aerosol observations. To the author's knowledge, a test of TE14 in the context of deep moist convection has not been accomplished, but would add knowledge regarding the water- and ice-friendly aerosol influence of the scheme. Additionally, testing the scheme in different geographic settings would potentially mete out skill differences for areas of more pollution, such as Los Angeles, CA, Beijing, China, or more pristine conditions such as the Pacific Intertropical Convergence Zone.

The views expressed in this thesis are those of the author and do not reflect the official policy or position of the United States Air Force, Department of Defense, or the U.S. Government.

REFERENCES

- 14WS, 2014: Climatology Narrative and Operational Climatic Data Summary II Seattle-Tacoma International Airport, 14th Weather Squadron.
- Abel, S. J., D. Walters, and G. Allen, 2010: Evaluation of stratocumulus cloud prediction in the Met Office forecast model during VOCALS-REx. *Atmospheric Chemistry and Physics*, 10, 10541-10559.
- Ackerman, A. S., O. Toon, D. Stevens, and J. A. Coakley, 2003: Enhancement of cloud cover and suppression of nocturnal drizzle in stratocumulus polluted by haze. *Geophys.Res.Lett.*, 30.
- Ackerman, A. S., O. B. Toon, and P. V. Hobbs, 1995: A model for particle microphysics, turbulent mixing, and radiative transfer in the stratocumulus-topped marine boundary layer and comparisons with measurements. *Journal of Geophysical Research*, 1995, 100, 7121-7133.
- Ackerman, A. S., O. B. Toon, J. P. Taylor, D. W. Johnson, P. V. Hobbs, and R. J. Ferek, 2000: Effects of aerosols on cloud albedo: Evaluation of Twomey's parameterization of cloud susceptibility using measurements of ship tracks. *J.Atmos.Sci.*, 57, 2684-2695.
- Ackerman, A. S., O. B. Toon, and P. V. Hobbs, 1993: Dissipation of marine stratiform clouds and collapse of the marine boundary layer due to the depletion of cloud condensation nuclei by clouds. *Science*, 262, 226-229, doi:262/5131/226 [pii].
- AFWA/A3W, 2014: Terrestrial Weather Thesis Topics for Academic Year 2014.
- Ahijevych, D., 2015: Image Archive Meteorological Case Study Selection Kit. [Available online at mmm.ucar.edu/imagearchive].
- AFI 11-202, 2014: Air Force Instruction 11-202: General Flight Rules. [Available online at www.e-publishing.af.mil].
- AFI 13-1AOC, 2012: Air Force Instruction 13-1AOC, Vol 3: Operational Procedures: Air and Space Operations Center: Space, Missile, Command, and Control., 94-95. [Available online at www.e-Publishing.af.mil].
- AFMAN 15-124, 2013: Air Force Manual 15-124: Meteorological Codes. [Available online at www.e-Publishing.af.mil].
- AFMAN 15-111, 2015: Air Force Manual 15-111: Surface Weather Observations. [Available online at www.e-Publishing.af.mil].

Albrecht, B. A., 1989: Aerosols, cloud microphysics, and fractional cloudiness. *Science*, 245, 1227-1230, doi:245/4923/1227 [pii].

Billings, P., J. Nolen, 2013: American Lung Association State of the Air. , www.stateoftheair.org/2013/assets/ala-sota-2013.pdf.

Bone, R., O. Olmos, and A. Mundra, 2000: Paired approach: A closely spaced parallel runway approach concept. *Federal Aviation Administration, Washington, DC*.

Bony, S., J. Dufresne, 2005: Marine boundary layer clouds at the heart of tropical cloud feedback uncertainties in climate models. *Geophys.Res.Lett.*, 32.

Brenguier, J., H. Pawlowska, L. Schüller, R. Preusker, J. Fischer, and Y. Fouquart, 2000: Radiative properties of boundary layer clouds: Droplet effective radius versus number concentration. *J.Atmos.Sci.*, 57, 803-821.

Brenguier, J., P. Chuang, Y. Fouquart, D. Johnson, F. Parol, H. Pawlowska, J. Pelon, L. Schüller, F. Schröder, and J. Snider, 2000: An overview of the ACE-2 CLOUDYCOLUMN closure experiment. *Tellus B*, 52, 815-827.

Colarco, P., A. da Silva, M. Chin, and T. Diehl, 2010: Online simulations of global aerosol distributions in the NASA GEOS-4 model and comparisons to satellite and ground-based aerosol optical depth. *Journal of Geophysical Research: Atmospheres (1984–2012)*, 115.

Coniglio, M. C., J. Correia Jr, P. T. Marsh, and F. Kong, 2013: Verification of convection-allowing WRF model forecasts of the planetary boundary layer using sounding observations. *Weather and Forecasting*, 28, 842-862.

Conover, J. H., 1966: Anomalous Cloud Lines. *J.Atmos.Sci.*, 23, 778.

Cotton, W. R., G. Bryan, and Van den Heever, Susan C, 2010: *Storm and cloud dynamics*. Vol. 99, Academic press, 1-8.

Cubison, M., B. Ervens, G. Feingold, K. Docherty, I. Ulbrich, L. Shields, K. Prather, S. Hering, and J. Jimenez, 2008: The influence of chemical composition and mixing state of Los Angeles urban aerosol on CCN number and cloud properties. *Atmospheric Chemistry and Physics*, 8, 5649-5667.

Dee, D., S. Uppala, A. Simmons, P. Berrisford, P. Poli, S. Kobayashi, U. Andrae, M. Balmaseda, G. Balsamo, and P. Bauer, 2011: The ERA-Interim reanalysis: Configuration and performance of the data assimilation system. *Q.J.R.Meteorol.Soc.*, 137, 553-597.

- Doughton, S., 2009: Puget Sound area ranks high in cancer risk from toxic air pollution, reports say. *The Seattle Times*.
- Feingold, G., A. J. Heymsfield, 1992: Parameterizations of condensational growth of droplets for use in general circulation models. *J.Atmos.Sci.*, 49, 2325-2342.
- Gao, F., X. Zhang, N. A. Jacobs, X. Huang, X. Zhang, and P. P. Childs, 2012: Estimation of TAMDAR observational error and assimilation experiments. *Weather and Forecasting*, 27, 856-877.
- Ginoux, P., M. Chin, I. Tegen, J. M. Prospero, B. Holben, O. Dubovik, and S. Lin, 2001: Sources and distributions of dust aerosols simulated with the GOCART model. *Journal of Geophysical Research: Atmospheres (1984–2012)*, 106, 20255-20273.
- Hallion, R. P., 1997: *Precision Guided Munitions and the New Era of Warfare*. Air Power Studies Centre.
- Harper, K., L. W. Uccellini, L. Morone, E. Kalnay, and K. Carey, 2007: 50th anniversary of operational numerical weather prediction. *Bull.Am.Meteorol.Soc.*, 88, 639-650.
- Hauke, M., 2014: Memorandum for AFWA/A3W Chief Scientist AFIT: Thesis/dissertation Topic Request.
- Iacono, M. J., J. S. Delamere, E. J. Mlawer, M. W. Shephard, S. A. Clough, and W. D. Collins, 2008: Radiative forcing by long-lived greenhouse gases: Calculations with the AER radiative transfer models. *Journal of Geophysical Research: Atmospheres (1984–2012)*, 113.
- ISU, 2015: Iowa State University: Meteorological data archive. [Available online at mtarchive.geol.iastate.edu/].
- JP 2-01.3, 2009: Joint Intelligence Preparation of the Battlefield. [Available online at fas.org/irp/doddir/dod/jp2-01-3.pdf].
- JP 3-09.1, 1999: Joint Tactics, Techniques and Procedures for Laser Designation Operations. [Available online at www.dtic.mil/cgi-bin/GetTRDoc?Location=U2&doc=GetTRDoc.pdf&AD=ADA434233].
- Kain, J. S., 2004: The Kain-Fritsch convective parameterization: an update. *J.Appl.Meteorol.*, 43, 170-181.
- Kiehl, J., K. E. Trenberth, 1997: Earth's annual global mean energy budget. *Bull.Am.Meteorol.Soc.*, 78, 197-208.

Kulesa, G., 2003: Weather and aviation: How does weather affect the safety and operations of airports and aviation, and how does FAA work to manage weather-related effects?, climate.dot.gov/documents/workshop1002/kulesa.pdf.

Lance, S., A. Nenes, and T. A. and Rissman, 2004: Chemical and dynamical effects on cloud droplet number: Implications for estimates of the aerosol indirect effect, *J. Geophys. Res.*, 109, D22208, doi:10.1029/2004JD004596. *Journal of Geophysical Research*, 109, doi:10.1029/2004JD004596.

Lasmanis, R., 1991: The geology of Washington. *Rocks and Minerals*, 66, 262-277.

Mass, C., 1981: Topographically forced convergence in western Washington State. *Mon. Weather Rev.*, 109, 1335-1347.

Moses, L., 2015: The Geology of Washington State. [Available online at www.dnr.wa.gov/Publications/ger_geol_map_washington_pagesize.pdf].

NCDC, 2015: NOMADS Data Access, NAM218 grid. [Available online at nomads.ncdc.noaa.gov/data.php?name=access].

Neemann, E., 2015: 16th Weather Squadron/Environmental Characterization, personal communication (e-mail).

Neiburger, M., 1944: Temperature changes during formation and dissipation of west coast stratus. *J.Meteorol.*, 1, 29-41.

Newton, I., 1934: *Philosophiae Naturalis Principia Mathematica* (1687), translated and reprinted by Cambridge Univ.

NOAA, 2015: Comprehensive Large Array-Data Stewardship System. [Available online at <http://www.class.ncdc.noaa.gov/saa/products/welcome;jsessionid=D4B5A82008B5E864C2CF69D860C8FCEA>].

NODC, 2015: Water Temperature Table of All Coastal Regions. [Available online at https://www.nodc.noaa.gov/dsdt/cwtg/all_meanT.html].

Norquist, D. C., 1999: Cloud predictions diagnosed from mesoscale weather model forecasts. *Mon. Weather Rev.*, 127, 2465-2483.

Pahlow, M., M. B. Parlange, and F. Porté-Agel, 2001: On Monin–Obukhov similarity in the stable atmospheric boundary layer. *Bound.-Layer Meteorol.*, 99, 225-248.

Petters, M., S. Kreidenweis, 2007: A single parameter representation of hygroscopic growth and cloud condensation nucleus activity. *Atmospheric Chemistry and Physics*, 7, 1961-1971.

Pringle, K., H. Tost, A. Pozzer, U. Pöschl, and J. Lelieveld, 2010: Global distribution of the effective aerosol hygroscopicity parameter for CCN activation. *Atmospheric Chemistry and Physics*, 10, 5241-5255.

Ramanathan, V., R. D. Cess, E. F. Harrison, P. Minnis, B. R. Barkstrom, E. Ahmad, and D. Hartmann, 1989: Cloud-radiative forcing and climate: results from the Earth radiation budget experiment. *Science*, 243, 57-63, doi:243/4887/57 [pii].

Randall, D. A., 1984: Stratocumulus cloud deepening through entrainment. *Tellus A*, 36, 446-457.

Rogers, R. R., M. Yau, 1989: A short course in cloud physics, International series in natural philosophy.

Saleeby, S. M., W. R. Cotton, 2004: A large-droplet mode and prognostic number concentration of cloud droplets in the Colorado State University Regional Atmospheric Modeling System (RAMS). Part I: Module descriptions and supercell test simulations. *J.Appl.Meteorol.*, 43, 182-195.

Skamarock, W., J. Klemp, J. Dudhia, D. Gill, and D. Barker, 2008: *A description of the Advanced Research WRF version 3.NCAR Tech.*

Stephens, G. L., T. J. Greenwald, 1991: The Earth's radiation budget and its relation to atmospheric hydrology: 2. Observations of cloud effects. *Journal of Geophysical Research: Atmospheres (1984–2012)*, 96, 15325-15340.

Thompson, G., T. Eidhammer, 2014: A study of aerosol impacts on clouds and precipitation development in a large winter cyclone. *J.Atmos.Sci.*, 71, 3636-3658.

Thompson, G., P. R. Field, R. M. Rasmussen, and W. D. Hall, 2008: Explicit forecasts of winter precipitation using an improved bulk microphysics scheme. Part II: Implementation of a new snow parameterization. *Mon.Weather Rev.*, 136, 5095-5115.

Timeanddate.com, 2015: Seattle, USA Sunrise, Sunset and Day Length. [Available online at <http://www.timeanddate.com/sun/usa/seattle?month=7&year=2013>].

Trenberth, K. E., J. T. Fasullo, and J. Kiehl, 2009: Earth's global energy budget. *Bull.Am.Meteorol.Soc.*, 90, 311-323.

- Twomey, S., 1974: Pollution and the planetary albedo. *Atmospheric Environment* (1967), 8, 1251-1256.
- USGS, Puget Sound Basin NAWQA. [Available online at wa.water.usgs.gov/projects/pugt/].
- Walters, M., 2000: Walters Comments on Grosso. *Bull.Am.Meteorol.Soc.*, 81, 2475.
- White, J., Gaunt, J., Dulfer, P., 2015: Flight routes, maps, ceiling minima and tactics, techniques and procedures in transit from KTCM to KYKM.
- Wielicki, B. A., E. F. Harrison, R. D. Cess, M. D. King, and D. A. Randall, 1995: Mission to planet Earth: Role of clouds and radiation in climate. *Bull.Am.Meteorol.Soc.*, 76, 2125-2153.
- Wood, R., 2012: Stratocumulus clouds. *Mon.Weather Rev.*, 140, 2373-2423.
- WPC, 2013: Surface Analysis. [Available online at http://www.wpc.ncep.noaa.gov/archives/web_pages/sfc/sfc_archive.php].
- Wyant, M. C., R. Wood, C. S. Bretherton, C. R. Mechoso, J. Bacmeister, M. A. Balmaseda, B. Barrett, F. Codron, P. Earnshaw, and J. Fast, 2010: The PreVOCA experiment: modeling the lower troposphere in the Southeast Pacific. *Atmospheric Chemistry and Physics*, 10, 4757-4774.
- Yang, Q., W. Gustafson Jr, J. D. Fast, H. Wang, R. C. Easter, H. Morrison, Y. Lee, E. G. Chapman, S. Spak, and M. Mena-Carrasco, 2011: Assessing regional scale predictions of aerosols, marine stratocumulus, and their interactions during VOCALS-REx using WRF-Chem. *Atmospheric Chemistry and Physics*, 11, 11951-11975.